

A NEAR-INFRARED SELECTED PHOTOMETRIC SURVEY OF DISTANT GALAXIES

Dissertation

der Fakultät für Physik
der
Ludwig-Maximilians-Universität München

vorgelegt von

Niv Drory

aus Haifa

München, den 15. Januar 2002

1. Gutachter: Prof. Dr. Ralf Bender
2. Gutachter: Prof. Dr. Simon D.M. White

Tag der mündlichen Prüfung:

to my father

Zusammenfassung

Die Entwicklung von Galaxien als Funktion der Zeit direkt zu verfolgen ist nicht möglich. Daher muß man sich auf die Untersuchung von statistischen Eigenschaften der Galaxienpopulation als Funktion der Rotverschiebung beschränken, um aus den Ensembleeigenschaften Rückschlüsse auf die Eigenschaften einzelner, typischer Mitglieder zu ziehen. In den letzten Jahren sind viele Durchmusterungen zu diesem Zweck durchgeführt worden, mit Auswahlkriterien in verschiedensten Wellenlängenbereichen, angefangen im Ultravioletten bis hin zum Submillimeterbereich.

Die früheren, optisch selektierten Durchmusterungen, unter anderen [Broadhurst et al. \(1988\)](#), [Colless et al. \(1990\)](#), [Lilly et al. \(1991\)](#), [Glazebrook et al. \(1994\)](#) und [Cowie et al. \(1994\)](#), markierten den Weg für den Canada-France Redshift Survey ([Lilly et al., 1995a](#); CFRS), eine *I*-Band selektierte Durchmusterung, welche Aufschlußreiche Folgerungen über die Entwicklung der Galaxienpopulation im Rotverschiebungsbereich $0.2 < z < 1$ zuließ. Insbesondere die Zunahme der mittleren Sternentstehungsrate und die Entwicklung der Leuchtkraftfunktion im *B*-Band bis zu einer Rotverschiebung von $z \sim 1$ zogen viel Aufmerksamkeit auf sich, da hiermit statistisch signifikante Ergebnisse über die Entwicklung der Galaxienpopulation über einen Zeitraum von ~ 8 Gyr vorlagen.

Selektion in einem bestimmten Wellenlängenbereich führt unweigerlich zu Selektionseffekten, der bevorzugten oder benachteiligten Aufnahme bestimmter Galaxienklassen in die Stichprobe. Dies kann auch zum Vorteil der Stichprobe genutzt werden, z.B. werden durch Selektion im blauen Licht bevorzugt sternbildende Objekte aufgenommen. Im nahinfraroten *K*-Band wird das Licht von Galaxien im Wesentlichen durch die Strahlung kühler, alter Sterne dominiert, was diesen Wellenlängenbereich relativ unempfindlich gegenüber dem Spektraltyp der Galaxie ([Cowie et al., 1994](#)) und ihrer augenblicklichen Sternentstehungsrate macht ([Kauffmann & Charlot, 1998](#)). Damit sind die *k*-Korrekturen in diesem Band klein und unterscheiden sich nur wenig entlang der Hubblesequenz. Das Licht im Nahinfraroten ist daher wesentlich durch die stellare Masse der Galaxie bestimmt [Rix & Rieke \(1993\)](#) und kann als Maß für diese Größe dienen [Brinchmann & Ellis \(2000\)](#).

Diese Arbeit beschäftigt sich mit einer *K*-Band selektierten Stichprobe von Galaxien im Rotverschiebungsbereich $0 < z < 1.5$, dem Munich Near-Infrared Cluster Survey (MUNICS). MUNICS überdeckt ein Quadratgrad in den nahinfraroten *J*- und *K*-Bändern und 0.6 Quadratgrad in den Optischen *V*-, *R*- und *I*-Bändern und stellt somit

die größte zur Zeit verfügbare, nahinfrarot selektierte Stichprobe dar.

Nach einem Überblick über den augenblicklichen Stand der Beobachtungen bezüglich der Entwicklung von Galaxien, und einem kurzen Einblick in die diesbezüglichen aktuellen theoretischen Konzepte in Kapitel 1, wendet sich Kapitel 2 der technischen Beschreibung des MUNICS-Projektes zu. Es werden die gewählten Himmelsfelder, die Empfindlichkeiten in den verschiedenen Filtern und das photometrische System der Durchmusterung vorgestellt. Die Reduktion der infraroten und der optischen Bilddaten wird besprochen, und die photometrische Kalibration der *K*-band Daten anhand des 2-Micron All Sky Surveys (2MASS), sowie die Anpassung der Kalibration der anderen Bänder mithilfe synthetischer stellarer Photometrie durchgeführt.

In Kapitel 3 wird eine neuentwickelte Software zur automatisierten Detektion, Photometrie, und Klassifikation von Quellen in Bilddaten vorgestellt. Diese Software ist insbesondere unter dem Gesichtspunkt der Anwendbarkeit auf wenig homogene Bilddatensätze optimiert. Sowohl der Hintergrund als auch das Rauschen wird in jedem Bild als Funktion des Ortes bestimmt und lokal zur Detektion von Quellen verwendet. Zur Photometrie von detektierten Quellen in anderen Bildern als dem Detektionsbild wird nicht erwartet, daß die Bilder das selbe Koordinatensystem teilen. Stattdessen wird lediglich mit (transformierbaren) Koordinaten- und Aperturlisten gearbeitet. Die Klassifikation der Quellen in Punktquellen (Sterne) und aufgelöste Quellen (Galaxien) wird in jedem Bild anhand eines Vergleichs mit der Punktverbreitungsfunktion eben dieses Bildes durchgeführt. Es wird kein Modell für die Punktverbreitungsfunktion a priori angenommen, diese wird direkt aus den Bildern heller Sterne in jedem Bild vermessen. Die Leistung des Softwarepaketes wird anhand mehrerer Beispieldaten von verschiedensten Instrumenten überprüft und mit anderen Paketen verglichen.

Kapitel 4 widmet sich der Erstellung von Objektkatalogen aus den Bilddaten. Die Parameter zur Objektdetektion und ihr Einfluß auf die Vollständigkeit und die Anzahl falscher Detektionen werden diskutiert. Diese werden so gewählt, daß die Kontamination der Kataloge durch falsche Quellen im Mittel unter 1% bleibt. Einen großen Stellenwert in diesem Kapitel nimmt die Untersuchung der Vollständigkeit des Kataloges bezüglich der Detektierbarkeit von Galaxien als Funktion der Rotverschiebung und als Funktion ihres Helligkeitsprofils ein. Ebenso wird die Verlässlichkeit der Messung der totalen Helligkeit als Funktion der Rotverschiebung und des Helligkeitsprofils (de Vaucouleurs bzw. exponentiell) untersucht. Hierzu wurden Simulationen mit Galaxien, welche den bekannten Skalierungsrelationen zwischen Helligkeit und Effektivradius genügen, durchgeführt, und ihr Ergebniss mit Vorhersagen der Sichtbarkeitstheorie verglichen und in deren Kontext interpretiert. Die wichtigsten Ergebnisse dieser Untersuchung sind eine Benachteiligung von elliptischen Galaxien hoher Gesamthelligkeit bei hohen Rotverschiebungen gegenüber Ellipsen mittlerer Gesamthelligkeit bei gleicher Rotverschiebung, da ihre Flächenhelligkeit geringer ist als die weniger heller Objekte. Die Photometrie heller Ellipsen ist auch wesentlich stärker systematisch zu zu kleinen Gesamthelligkeiten verfälscht, verglichen mit Objekten mittlerer Helligkeit, welche im Mittel richtig vermessen werden. Beide Probleme sind bei exponentiellen Profilen erheblich weniger stark ausgeprägt. Sehr schwache Objekte werden prinzipiell zu hell eingeschätzt, da diese nur durch die Streuung von Bildpunkten zu höheren

Helligkeiten hin detektiert werden. Objekte mit $M^* - 1 < M < M^* + 2$ werden im Allgemeinen richtig vermessen, sofern sie noch detektierbar sind. Ein weiteres interessantes Ergebnis ist, daß moderates Seeing bei der Detektion schwacher, entfernter Quellen hilfreich ist, da es Licht aus dem Zentrum des Profils etwas nach aussen verteilt und somit die Fläche mit hoher Helligkeit vergrößert. Mit wachsendem Seeing kehrt sich der Effekt um, da dann die gesamte Fläche durch den Verbreiterungseffekt unter dem Detektionslimit verschwindet.

Kapitel 5 widmet sich der Bestimmung der *K*-Band Leuchtkraftfunktion und ihrer Entwicklung im Rotverschiebungsbereich $0.4 < z < 1.2$, unter Berücksichtigung der vorangegangenen Erkenntnisse. Zunächst wird ein Verfahren zur Bestimmung photometrischer Rotverschiebungen vorgestellt und an Hand eines Datensatzes von ca. 340 spektroskopisch ermittelten Rotverschiebungen geeicht. Das Verfahren benutzt eine Bibliothek aus spektralen Energieverteilungen (SEDs; spectral energy distributions), welche aus den spektroskopisch ermittelten Rotverschiebungen und den photometrischen Daten dieser Galaxien erstellt und optimiert wurden, anstatt sich rein auf SEDs aus Modellrechnungen zur spektralen Entwicklung von Sternpopulationen zu verlassen. Die Leuchtkraftfunktion wird im Folgenden behandelt. Es zeigt sich, daß die Daten mit der Lokalen *K*-Band Leuchtkraftfunktion bis zum größten untersuchten Rotverschiebungsintervall von $1.0 < z < 1.2$ verträglich sind, d.h. die Leuchtkraftfunktion entwickelt sich kaum. Da man aber mindestens von passiver Evolution der stellaren Populationen der Galaxien ausgehen muß, ergibt sich zwangsläufig, daß auch eine Dichteentwicklung stattgefunden haben muß, um die gesamte Leuchtkraftfunktion konstant zu halten. Desweiteren wird die Leuchtkraftfunktion als Funktion des Spektraltyps der Galaxien untersucht. Die Stichprobe wird hierbei in frühe, mittlere und späte Typen unterteilt. Die frühen Typen scheinen bei hohem z und hohen Helligkeiten etwas weniger zahlreich zu sein als lokal. Da aber diese Typen vorwiegend elliptische Galaxien sind, könnte dies durch die in Kapitel 4 besprochenen Auswahl effekte erklärbar sein. Die mittleren Typen zeigen keine signifikante Entwicklung, während die späten Typen einen interessanten Trend zeigen: Bei höheren Rotverschiebungen tauchen immer mehr, immer hellere blaue Galaxien auf. Interpretiert man nun die *K*-Band Helligkeit als Maß für die stellare Masse, so ergibt sich hieraus, daß massereichere Galaxien bei höherem z blau werden als masseärmere Galaxien, oder, anders ausgedrückt, massereiche Galaxien haben ihre Sterne tendenziell früher gebildet als masseärmere Objekte.

In Kapitel 6 wird die Entwicklung der Massenfunktion der Galaxien besprochen. Um die stellare Masse einer Galaxie aus ihrer *K*-Band Helligkeit abzuleiten, wird zunächst ein Modell maximaler passiver Evolution verwendet. Hierbei wird angenommen, dass alle Sterne so alt sind, wie das Universum bei der Rotverschiebung der Galaxie. Da das Masse-Leuchtkraft Verhältniss im *K*-Band eine monotone Funktion der Zeit ist (für Populationen, welche älter als ~ 2 Gyr sind), folgt aus dem maximalen Alter auch eine maximale Masse bei gegebenem *K*-Band Licht. Es wird die integrierte Massenfunktion betrachtet, d.h. die Anzahldichte von Galaxien mit einer Masse über einem bestimmten Limit, in unserem Fall $2 \times 10^{10} M_{\odot}$, $5 \times 10^{10} M_{\odot}$ und $1 \times 10^{11} M_{\odot}$. Während die Massenfunktionen für das kleinste untere Limit (entspricht ca. L^* -Objekten) sich

kaum ändert, nimmt die Anzahl-dichte für höhere Limits mit der Rotverschiebung um einen Faktor $\sim 2 \dots 4$ ab. Dieses Ergebnis wird mittels eines weiteren Verfahrens zur Bestimmung der Masse aus der *K*-Band Helligkeit überprüft. Es werden Modelle zur Entwicklung stellarer Populationen mit exponentiell abnehmenden Sternentstehungsraten herangezogen, um durch Ausgleichsrechnung ein am besten passendes Modell für jede einzelne Galaxie zu finden. Dessen Masse-Leuchtkraft Verhältnis wird der Galaxie zugewiesen. Daß das Masse-Leuchtkraft Verhältnis im *K*-Band nur wenig von der Sternentstehungsrate abhängt, sind die Ergebnisse für die Massenfunktion von den vorhergehenden ununterscheidbar. Es wird das selbe Verhalten als Funktion der Massengrenze und der Rotverschiebung festgestellt. Insbesondere die Tendenz zu einer stärkeren Entwicklung bei Galaxien mit höherer Masse ist im Zusammenhang mit hierarchischen Modellen zur Galaxienentstehung hervorzuheben, wobei die Modelle aber nachwievorn zu junge stellare Populationen in massereichen Galaxien vorhersagen.

Contents

1	Introduction	1
1.1	Observational evidence for galaxy evolution	1
1.1.1	Redshift surveys	2
1.1.2	High-redshift early-type galaxies	2
1.1.3	Early-type galaxies in clusters and their scaling relations	3
1.1.4	Scaling relations in the field	5
1.1.5	The global star formation rate of field galaxies	6
1.1.6	Morphological evolution	7
1.1.7	Evolution of clustering and merging	8
1.1.8	Lyman-break galaxies	10
1.2	The theoretical side	11
1.2.1	Gas and star formation	11
1.2.2	Evolution of galaxies	11
1.2.3	Linking with observations	12
1.3	Outline	13
2	The Survey	15
2.1	Motivation	15
2.2	Survey concept and layout	17
2.2.1	Scientific aims	17
2.2.2	Limiting sensitivity	20
2.2.3	Field selection	20
2.2.4	Photometric system	22
2.3	Observations and data reduction	25
2.3.1	Infrared observations and data reduction	25
2.3.2	Optical observations and data reduction	29
2.3.3	Astrometry	30
2.3.4	Final photometric calibration	30
2.3.5	Spectroscopy	31
3	Yet another object detection algorithm: YODA	33
3.1	Introduction	33
3.2	Overview of YODA	34
3.3	Object detection	35
3.3.1	Background determination, thresholding, and object assembly	35

3.3.2	Splitting of multiple components	36
3.3.3	Evaluation of shape parameters	36
3.4	Photometry	37
3.5	Star-galaxy separation	38
4	Image analysis	45
4.1	Object detection	45
4.2	Photometry	46
4.3	Star-galaxy separation	48
4.4	Galactic extinction	49
4.5	Completeness	49
4.5.1	Implementation of the simulations	50
4.5.2	Elliptical galaxies	51
4.5.3	Results of the simulations	53
4.5.4	Discussion	54
4.5.5	Visibility theory	56
4.5.6	Lost-light fraction	61
4.5.7	The effect of seeing	62
4.5.8	Detection probabilities for the MUNICS Fields	65
4.6	Galaxy number counts	69
4.7	Colour distributions and objects at $z \geq 1$	71
5	The rest-frame K-band luminosity function	73
5.1	Introduction	73
5.2	The galaxy sample	74
5.3	Photometric redshifts	75
5.3.1	Construction of SED templates	75
5.3.2	The redshift probability function	76
5.3.3	Application of the technique	78
5.4	The cumulative redshift distribution	81
5.5	Computing the luminosity function	83
5.5.1	The V_{\max} method	83
5.5.2	Monte-Carlo simulations	84
5.6	Results	88
5.6.1	Influence of the completeness corrections	88
5.6.2	The final rest-frame K -band luminosity function	88
5.6.3	The rest-frame K -band luminosity function by spectral type	90
6	The mass function of field galaxies	93
6.1	Introduction	93
6.2	The maximum PLE model	94
6.3	The fitted mass-to-light-ratio model	96
6.4	Discussion	98
A	Photometric calibration using the stellar sequence	111

B Detection probabilities for pointlike and extended sources

123

List of Figures

2.1	<i>k</i> -Corrections in the <i>I</i> and <i>K</i> bands	16
2.2	Apparent <i>K</i> -band magnitude of galaxies of mass $10^{11}M_{\odot}$ with different star formation histories	17
2.3	Stellar population synthesis models in the <i>J</i> – <i>K'</i> vs. <i>K'</i> plane for different star-formation histories	18
2.4	Layout and nomenclature of one of the MUNICS ‘mosaic fields’	21
2.5	Relative transmission of the MUNICS <i>V</i> , <i>R</i> , <i>I</i> , <i>J</i> , and <i>K'</i> filters	22
2.6	Comparison of stellar colours from synthetic photometry with MUNICS data	24
2.7	Histogram of spectroscopic redshifts	31
3.1	Comparison of photometry in 5 arcsec circular apertures between SExtractor and YODA	38
3.2	Cuts through the likelihood surface at $\beta = 0$	40
3.3	Results of applying the resolution classifier to artificial stellar images and to an <i>R</i> -band image of the globular cluster M92	41
3.4	Results of applying the resolution classifier to an <i>R</i> -band image of the (resolved) dwarf galaxy IC10 and to an image of the globular cluster NGC288	41
3.5	Comparison of the scale parameter α in different wavebands	42
4.1	The 50 per cent completeness limit as a function of object-detection parameters	46
4.2	Signal-to-noise ratio in <i>K'</i> and <i>R</i> as a function of magnitude	47
4.3	Magnitude errors as a function of magnitude	48
4.4	Absolute <i>K'</i> -band Magnitudes and effective radii of simulated disk galaxies	53
4.5	Detection probability for point-like sources, de Vaucouleurs profiles, and exponential profiles	54
4.6	Comparison of true magnitude and output magnitude	55
4.7	Comparison of surface-brightness profiles	56
4.8	Comparison of measured and predicted areas above the detection threshold for point-like sources	57
4.9	Comparison of measured and predicted areas above the detection threshold for extended sources	58

4.10	Comparison of true magnitude and output magnitude for exponential profiles	60
4.11	Comparison of true magnitude and output magnitude for de Vaucouleurs profiles	62
4.12	Visibility and completeness functions for de Vaucouleurs profiles at 0.8 arcsec and 1.6 arcsec seeing	63
4.13	Visibility and completeness functions for exponential profiles at 0.8 arcsec and 1.6 arcsec seeing	64
4.14	Number counts for galaxies in K' , J , I , R , and V	69
4.15	Colour–magnitude and colour–colour diagrammes for MUNICS objects	72
5.1	A low-resolution spectrum constructed from objects with known spectroscopic redshifts	76
5.2	Final SED library for determining photometric redshifts	77
5.3	Comparison of photometric and spectroscopic redshifts	78
5.4	Examples of photometric redshift determinations	79
5.5	The $M_K - z$ relationship	80
5.6	The redshift distribution of the total sample	81
5.7	The redshift distribution of $16 < K < 18$ galaxies	83
5.8	Monte-Carlo realisations of the luminosity function	85
5.9	Completeness corrections in the luminosity function	87
5.10	The rest-frame K -band luminosity function at $0.4 < z < 1.2$	89
5.11	The rest-frame K -band luminosity density at $0.4 < z < 1.2$	90
5.12	The K -band luminosity function by spectral type	91
6.1	The integrated mass function using maximum PLE	95
6.2	Grid of CSP models with exponentially declining star formation rates	96
6.3	Evolution of \mathcal{M}/L_K with age for different star formation histories	97
6.4	The average \mathcal{M}/L_K of the MUNICS sample as a function of redshift	98
6.5	Integrated mass function using PLE and fitted mass-to-light ratios	99
A.1	Photometric calibration with artificial stellar photometry field S2F1	112
A.2	Photometric calibration with artificial stellar photometry field S2F5	113
A.3	Photometric calibration with artificial stellar photometry field S3F1	114
A.4	Photometric calibration with artificial stellar photometry field S3F5	115
A.5	Photometric calibration with artificial stellar photometry field S4F1	116
A.6	Photometric calibration with artificial stellar photometry field S5F1	117
A.7	Photometric calibration with artificial stellar photometry field S5F5	118
A.8	Photometric calibration with artificial stellar photometry field S6F1	119
A.9	Photometric calibration with artificial stellar photometry field S6F5	120
A.10	Photometric calibration with artificial stellar photometry field S7F5	121
B.1	Detection probabilities in field S2F1	124
B.2	Detection probabilities in field S2F5	125
B.3	Detection probabilities in field S3F1	126
B.4	Detection probabilities in field S3F5	127

B.5	Detection probabilities in field S4F1	128
B.6	Detection probabilities in field S5F1	129
B.7	Detection probabilities in field S5F5	130
B.8	Detection probabilities in field S6F1	131
B.9	Detection probabilities in field S6F5	132
B.10	Detection probabilities in field S7F5	133

List of Tables

2.1	The MUNICS Mosaic Fields	26
2.2	The MUNICS Quasar Fields	27
2.3	MUNICS observing runs	28
4.1	Parametric description of the completeness function for point-like sources	66
4.2	Parametric description of the completeness function for de Vaucouleurs profiles	67
4.3	Parametric description of the completeness function for exponential profiles	68
4.4	K' , J , I , R , and V -band galaxy number counts for the MUNICS mosaic fields	70
5.1	Mosaic Fields used for constructing the luminosity function and the mass function	74

Chapter 1

Introduction

The last decade has seen unprecedented progress in the observational study of galaxy formation and evolution, made possible by the advance in space-based and ground-based instrumentation.

The high spatial resolution imaging capabilities (roughly 1 kpc at $z = 1$) of the Hubble Space Telescope (HST) extended our possibility to study the morphology and scaling relations of galaxies to redshifts around unity, allowed the detailed study of the dynamics in galaxy cores, and enabled us to resolve the stellar populations of local galaxies into single stars.

New wide-field CCD imagers at ground-based 4-m and 8-m-class telescopes made deep multi-colour imaging surveys feasible, probing normal (L^*) galaxies to $z \sim 1.5$, and allowed a first glimpse at the galaxy population at $z \sim 3$ by dropout selection techniques. Additionally, wide-field detector arrays sensitive to near-infrared light became available. Simultaneously, multi-object spectrographs facilitated the undertaking of statistically significant and complete redshift surveys to $z \sim 1$ as well as follow-up spectroscopy of Ly-break galaxies.

Finally, new bolometers in the sub-mm and satellites in the infrared and the X-ray regime have extended our wavelength coverage into these domains.

1.1 Observational evidence for galaxy evolution

A tempting strategy for the observational study of the evolution of galaxies is to simply observe samples of galaxies at increasingly larger look-back times and compare their ensemble properties to those of galaxies in the local universe. A remarkable and most extreme undertaking of such a kind are the Hubble Deep Field (HDF) observations (Williams et al., 1996, 2000; Casertano et al., 2000), the deepest images obtained so far, spanning 80% of the universe's age (see Ferguson et al., 2000, for a review).

A picture has emerged in recent years in which there is only mild evolution in the population of normal luminous ($\sim L^*$) galaxies to $z \simeq 1$, while less luminous blue galaxies do evolve significantly over the same redshift range.

1.1.1 Redshift surveys

Optically selected imaging and spectroscopic surveys of samples of typically 500 to 2000 field galaxies in the redshift range $0.2 \lesssim z \lesssim 1$, most notably the Autofib survey (Ellis et al., 1996), the Canada France Redshift Survey (CFRS; Lilly et al., 1995a) and the Canadian Network for Observational Cosmology surveys (CNOC I; Yee et al., 1996; CNOC II; Yee et al., 1996) have probed basic properties of galaxies to look-back times of ~ 10 Gyr.

The pioneering CFRS found that the Luminosity Function (LF) in the B -band of the blue field population brightens by roughly 1 mag to $z \simeq 1$ and also becomes steeper at the faint end at $z \gtrsim 0.5$ (see also Heyl et al., 1997). In contrast, the red population was found to show very little change in either number density or luminosity (Lilly et al., 1995b). Lin et al. (1999) attempted to discriminate explicitly between number-density and luminosity evolution in the CNOC2 sample consisting of roughly 2000 galaxies. They found that the early-type population shows positive luminosity evolution (1.6 mag) which is nearly compensated by negative density evolution (factor of 0.5), so that there is little net change in their overall LF. The intermediate-type population shows positive luminosity evolution (0.9 mag) plus weak positive density evolution (factor of 1.7), resulting in mild positive evolution in its luminosity density. The amount of luminosity evolution in the early- and intermediate-type populations is consistent with expectations from models of passive evolution of their stellar populations. The late-type population is best fit by a strong increase in number density at high redshift (factor of 4.1), accompanied by only little positive luminosity evolution (0.2 mag). The overall B -band luminosity density of late-type objects was found to increase rapidly in both the CFRS and CNOC II samples, while the luminosity density of early-type objects was found to be nearly constant. However, these studies are not sensitive enough to probe the sub- L^* regime beyond the knee of the LF, such that the disentanglement of luminosity and density evolution cannot be very robust.

1.1.2 High-redshift early-type galaxies

Dedicated studies of the most massive early-type systems, whose density evolution is expected to be strongest, have led to contradictory results regarding the amount of number density evolution present to $z \approx 1$. Early-type galaxies selected from the CFRS were analysed by Kauffmann et al. (1996) and were found to be strongly evolving in number density using V/V_{\max} statistics. Totani & Yoshii (1998) have argued that this result strongly depends on the exact selection criteria applied to extract these objects from the catalogue, as colour criteria were applied since no suitable morphological data were available (see also Totani & Yoshii, 2000 for the role of selection effects).

As an alternative to selection by optical colours alone, many attempts were made to select early-type galaxies at $z \gtrsim 1$ by their very red optical-infrared colour, usually chosen as $R-K > 5$ or $R-K > 6$ (Martini, 2001; Daddi et al., 2000; Cimatti et al., 2000; Chapman et al., 2000; Yan et al., 2000; Liu et al., 2000; Thompson et al., 1999). Studies of the surface densities of these Extremely Red Objects (EROs; Hu & Ridgway, 1994), have revealed that they are truly mostly $z \gtrsim 1$ early-type systems with a contribution of $\sim 15\%$ of dusty starbursts, according to HST-based morphological

studies by [Moriondo et al. \(2000\)](#), and according to their strong clustering amplitude ([Daddi et al., 2000](#)). These studies generally found the surface densities of EROs to be compatible with the expectations from passive evolution of today's population of early-type systems and thus requiring no density evolution. Yet these studies were restricted to very small fields of view until very recently, and it is yet unclear what fraction of the galaxies selected this way are actually ellipticals, as luminous Sa and Sb type spirals at higher redshifts may also fulfil the selection criteria. The actual redshift distribution of the systems selected this way is also unknown, since spectroscopic redshift measurements are very difficult for these objects, due to their faintness in the optical bands and the difficulty of near-IR spectroscopy ([Cimatti et al., 1999](#)).

Taken together, it is unclear how reliable this selection technique is, and therefore the interpretation of the measured surface densities in terms of volume number densities is by no means straightforward.

Using HST imaging, several studies investigated the abundance of morphologically selected galaxies to $z \sim 1$. [Im et al. \(1996\)](#) constructed the luminosity function of field elliptical galaxies in redshift bins to $z = 1.2$ using data from the HST Medium Deep Survey (MDS; [Griffiths et al., 1994](#)) and the Groth Survey Strip ([Groth et al., 1994](#)). They concluded that the LF brightens by 0.5 to 1 mag to $z = 1.2$, and that there was no significant evolution in the number density.

By combining morphology and colour criteria, [Menanteau et al. \(1999\)](#) and [Treu & Stiavelli \(1999\)](#) concluded that the number density of early-type galaxies at high z is smaller than what is expected from models of passive evolution of the local population. However, [Schade et al. \(1999\)](#) pointed out that the number density of early-type objects is consistent with being constant from $z \sim 1$ to $z \sim 0.2$ if selected purely by morphology using no colour criterion. This suggests that some low star formation activity in these objects might be making them appear bluer than expected from pure passive evolution.

1.1.3 Early-type galaxies in clusters and their scaling relations

A convenient way to study early-type galaxies is to target clusters of galaxies with their large fraction of early-type members. In recent years these studies have pushed as far as $z = 1.27$ ([Stanford et al., 1997](#); [van Dokkum et al., 2001](#)). In a study of 19 clusters out to $z = 0.9$, [Stanford et al. \(1998\)](#) found that the slope of the colour-magnitude relationship shows no significant change, which provides evidence that it arises from a correlation between galaxy mass and metallicity, not age ([Stanford et al., 1998](#)). Furthermore, the intrinsic scatter in the optical-IR colours of the galaxies is small and nearly constant with redshift, which indicates that the majority of giant, early-type galaxies in clusters share a common star formation history, with little perturbation due to uncorrelated episodes of later star formation.

[de Propris et al. \(1999\)](#) studied the K -band luminosity function in 38 clusters spanning $0.1 < z < 1$, finding that $K^*(z)$ departs from no-evolution predictions at $z \gtrsim 0.4$ and is consistent with the behaviour of a simple passive luminosity evolution model in which galaxies form all their stars in a single burst at $z_f = 3$ in an $H_0 = 65 \text{ km s}^{-1} \text{ Mpc}^{-1}$, $\Omega_M = 0.3$, $\Omega_\Lambda = 0.7$ universe.

The $\text{Mg}-\sigma$ relation of cluster early-type galaxies as a function of redshift is a reli-

able diagnostic of old stellar populations for its near independence of the Initial Mass Function (IMF). This relation also reveals passive evolution at least to $z \approx 0.4$ (Bender et al., 1996; Ziegler & Bender, 1997), with the bulk of the stars forming at $z > 2$ and at redshifts as high as 4 in the most massive systems.

By comparing the correlation of Balmer line-strengths with the velocity dispersions for E/S0 galaxies in four clusters spanning $0.06 < z < 0.83$ Kelson et al. (2001) found moderate evolution in the zero point of the $(H\gamma+H\delta)$ - σ relation with redshift, consistent with the passive evolution of old stellar populations. Under the assumption that the samples can be compared directly (which is not trivial, since it is by no means self-evident that the antecedents of today’s early-types are the early-types we see at high redshift), single-burst stellar population synthesis models constrain the last major occurrences of star formation in the observed E/S0 galaxies to be $z_f > 2.5$.

Yet stronger constraints on the time scale and physics of galaxy formation are obtained from the study of galaxy scaling relations as a function of redshift, coupling the dynamics (and total masses) of galaxies to their stellar populations. They allow the comparison of galaxies of *similar masses* at different redshifts.

Studies of the Fundamental Plane (FP; e.g., Djorgovski & Davis, 1987; Bender et al., 1992) of early-type galaxies in clusters and its evolution with redshift can be used to derive the evolution of the mass-to-light ratio \mathcal{M}/L in the galaxies. This provides a combined constraint on the formation redshift of the stars and the initial mass function (IMF), given a cosmological model.

Up to $z \lesssim 0.5$ (e.g., van Dokkum & Franx, 1996; Kelson et al., 1997; Ziegler et al., 1999; Kelson et al., 2000) such investigations generally agree that the evolution in the B -band mass-to-light ratios \mathcal{M}/L_B is compatible with passive evolution and consistently derive formation redshifts of $z_f \gtrsim 2$. Additionally, the scatter of the FP relation shows no evolution with redshift, staying constant at approximately 15%. This is taken as evidence for the uniformity of the formation time scale and processes of the early-type population in clusters. Recent extension of these studies to a cluster at $z = 0.83$ (van Dokkum et al., 1998) yielded similar results, pointing to $z_f > 1.7$ with a Salpeter IMF, $\Omega_M=0.3$, and $\Omega_\Lambda=0.7$.

At present, a limiting factor in constraining z_f from the observed luminosity evolution of early-type galaxies is the poor understanding of the IMF (van Dokkum et al., 1998). In strong starbursts, the formation of low-mass stars might be suppressed. Low-mass stars are formed predominantly in cold molecular clouds where the Jeans mass is small. Such clouds are less common when the ambient star formation rate is high because of the energy released by supernovae (see, e.g., Charlot et al., 1993; Rieke et al., 1993 and references therein).

Another severe problem such studies may suffer from is a selection effect termed “progenitor bias” (van Dokkum & Franx, 1996): those early-type galaxies which have spirals as progenitors at the redshift in question, are not included in the samples. This leads to a strong bias towards the oldest galaxies in the clusters. In fact, van Dokkum & Franx (2001) show that 50% of today’s early-type galaxies in clusters may have been morphologically transformed from spirals at $z < 1$ and their progenitor galaxies may have had roughly constant star formation rates prior to morphological transformation. The mean luminosity weighted formation redshift of the stars in this case becomes as

low as $\langle z_* \rangle = 2.0^{+0.3}_{-0.2}$ (see also Sect. 1.1.6 below).

1.1.4 Scaling relations in the field

In the field, it is more difficult to gather data for significant samples of early-type galaxies, because of the relative paucity of these objects relative to the denser environments in clusters. Therefore, larger areas have to be imaged (using HST) and spectroscopy is less efficient since not many objects can be observed at once using multi object spectroscopy.

From a sample of 25 objects selected from the HST-based medium deep survey, [Treu et al. \(2001\)](#) conclude that the scatter of the FP at $z \approx 0.4$ is as small as that in the Coma Cluster and that the intermediate z FP is offset towards the local one by an amount compatible with passive evolution and $z_f \gtrsim 2$. The sample does not span a range large enough to infer the slope of the relation.

The situation is not very different with regard to spiral galaxies. Although more numerous in the field, the need for spatially resolved spectroscopy to deduce rotation curves for the Tully-Fisher (TF) relation makes such observations rather difficult at ground-based sites, even with large telescopes.

A number of studies have nevertheless assessed the evolution of the TF relation in the field to $z \sim 1$. [Vogt et al. \(1996\)](#) looked at nine faint field galaxies in the redshift range $0.1 \lesssim z \lesssim 1$ and found that the rotation curves appear similar to those of local galaxies in both form and amplitude, implying that some massive disks were in place at $z \sim 1$. The key result was that the kinematics of these distant galaxies show evidence for only a modest increase in luminosity ($\Delta M_B \lesssim 0.6$ mag) compared to the TF relation for local galaxies.

[Vogt et al. \(1997\)](#) added 8 Galaxies in the HDF to the previous sample to provide a high-redshift TF relation spanning 3 magnitudes. This sample was selected primarily by morphology and magnitude, rather than colour or spectral features. They concluded that there was no change in the shape or slope of the relation with respect to the local one and that the offset in the disk luminosity is presumably caused by luminosity evolution in the field galaxy population and does not correlate with galaxy mass.

From a sample defined by 12 intermediate-redshift kinematically normal galaxies, ([Simard & Pritchett, 1998](#)) construct a TF relation at $z = 0.35$, finding that these galaxies have a systematically lower rotation velocity (i.e., mass) for their luminosity than expected from the local TF relation, in agreement with other studies. Yet the offset from the local relation is higher than that of [Vogt et al.](#), namely ~ 1.5 mag. These authors also find a hint that massive galaxies are not as displaced from the local TF relation as low-mass ones, which might provide an explanation of the discrepancy, if the galaxies of [Vogt et al.](#) were systematically more massive.

Selection effects are expected to be important in these analyses, as the scatter in the local TF relation is large, especially for late-type galaxies. Sample selection effects, particularly in [O II] emission strength, could be responsible for part of the observed TF evolutionary shift if star formation rates were responsible for the local TF relation scatter.

Therefore it is likely that a mass-dependent luminosity evolution scenario can ex-

plain the available kinematics and surface brightness data, although it is obvious that the constraints set by the data are indicative at most. The strongest conclusion one can draw is that disks with masses comparable to present day galaxies are in place at $z \sim 1$, although they might be systematically brighter and have less regular morphology (see Sect. 1.1.6 below).

1.1.5 The global star formation rate of field galaxies

Star formation rate measurements spanning a wide range of observational techniques and different star formation indicators have been published in recent years, suffering from different selection effects and different sensitivities to dust extinction and to the stellar Initial Mass Function (IMF). A number of studies addressed the evolution of the mean comoving star formation density in the interval $0 < z \lesssim 1$ self-consistently, i.e. by using the same star formation indicator for at least two distinct redshift bins.

For example, Lilly et al. (1996) and Hammer et al. (1997) measured the star formation rate using the rest-frame 2800Å luminosity density and the [O II] emission line strength of CFRS galaxies, respectively. Hogg et al. (1998) observed 375 galaxies in the HDF region and measured [O II] equivalent widths, while (Cowie et al., 1999) inferred the star formation rate from rest-frame UV fluxes in multicolour data of the same region. Rowan-Robinson et al. (1997) obtained far-IR fluxes of 8 sources in the HDF and Flores et al. (1999) obtained 15 μm ISO observations of a CFRS survey field to investigate the contribution of strong starbursts to the overall star formation rate. Mobasher et al. (1999) carried out a 1.4 GHz survey of distant galaxies and (Haarsma et al., 2000) measured the 1.4 GHz fluxes of galaxies with known redshifts in the HDF and other public data sets.

Remarkably, all these studies agree that the average field star formation rate has declined by a factor of ~ 10 (on average) from $z \sim 1$ to the present epoch. Hogg (2001) argues that this is the most secure positive detection of galaxy evolution so far. The main source of systematic discrepancies between the different star formation indicators used in the above studies is absorption by dust. Flores et al. (1999), using ISOCAM data, conclude that 4% of field galaxies at $z \lesssim 1$ are strong and heavily extinguished starbursts with star formation rates of 50 to 200 $M_{\odot}\text{yr}^{-1}$. Yet this sparse population is responsible for roughly 25% of the star formation density at $z \sim 1$.

This picture was augmented by studies of the global star formation rate as a function of redshift in the HDF, spanning a much wider range in redshift of $0 < z \lesssim 4$. It was found to increase from the present epoch up to redshifts of $z \sim 1$ and appeared to steadily fall off beyond redshifts of $z \sim 2$ (Madau et al., 1996), thus exhibiting a peak in the same redshift range where the assembly of the Hubble Sequence seemed to have taken place (see Sect. 1.1.6 below).

However, other considerations have led to a global picture that may not be as clear: Sub-millimetre observations (Hughes et al., 1998) and near-IR emission line measurements (Pettini et al., 1998; Moorwood et al., 2000; Teplitz et al., 2000) showed that significant dust extinction is present in the $z \gtrsim 2.5$ galaxies, substantially increasing the star formation rates in Lyman-Break Galaxies compared to the values initially inferred from their rest-frame UV emission, all in all questioning the peak at $z \sim 1.5 - 2$

in the star formation history of the universe. Also, newer UV selected surveys for star-forming galaxies found higher values than before (Treyer et al., 1998; Sullivan et al., 2000), increasing somewhat the star formation rate in the local universe, lowering the increase of the star formation rate to $z \sim 1$ to a factor of ~ 4 .

Nevertheless, the increase in luminosity density seen in all optical bands and at $1\mu\text{m}$ (Madau et al., 1998) and the increased star formation activity to $z \sim 1$ are to be considered firm observational evidence of galaxy evolution.

1.1.6 Morphological evolution

Only HST with its spatial resolution of ~ 1 kpc at $z \sim 1$ made it possible to study the morphology of significantly redshifted galaxies. When the HDF images became available, it became clear that the young galaxies seen at $z \gtrsim 2$ in these ultra-deep images were very different from their local counterparts, with no galaxies of regular appearance visible at larger redshifts.

The excess numbers of blue galaxies at faint magnitudes have been first noticed in early deep ($B \gtrsim 22$) imaging surveys (see Ellis, 1997, for a review on these faint blue galaxies). Their morphologies were first revealed using the MDS imaging program. Glazebrook et al. (1995) and Driver et al. (1995) used galaxy number counts as a function of galactic morphology to find that the elliptical and spiral galaxy counts both follow the predictions of no-evolution models to their magnitude limits, indicating that regular Hubble Sequence evolves only slowly to $z \sim 0.5$, whereas the irregular/peculiar/merger galaxies have a very steep number - magnitude relation and greatly exceed predictions based on proportions in local surveys, making up half the total counts at $I = 22$.

HST follow-up imaging of major ground-based redshift surveys (Brinchmann et al., 1998) established that the increase in numbers of galaxies having irregular/peculiar/merger morphologies as a function of redshift is still found after taking the bias towards later types due to bandpass shifting into account. Note that Ferguson et al. (2000) compared optical and near-IR morphologies of distant galaxies finding that they are mostly similar, in the sense that compactness or coarse disk-structure is preserved. Brinchmann et al. (1998) found a substantial increase in the fraction of irregular galaxies from 9% at $z \approx 0.4$ to 32% at $z \approx 0.8$ and attributed the increase in blue luminosity density to these galaxies.

Using the same sample, Lilly et al. (1998) found that the sizes of large galaxy disks do not change significantly out to $z \sim 1$. The size function of disk scale lengths in disk-dominated galaxies (i.e., with bulge-to-total ratios, $B/T \leq 0.5$) was found to stay roughly constant to $z \sim 1$, at least for those larger disks with exponential scale lengths $r > 3.2h_{50}^{-1}$ kpc, where the sample was most complete. This result suggests that massive galactic disks cannot have grown substantially since $z \sim 1$, unless a corresponding number of large disks have been destroyed through merging.

In addition to a roughly constant number density, the galaxies with large disks, $r > 4h_{50}^{-1}$ kpc, were found to have properties consistent with the idea that they are similar galaxies observed at different times. However, on average, they show higher B -band disk surface brightnesses, bluer overall ($U-V$) colours, higher [O II] equivalent

widths, and less regular morphologies at high redshift than at low redshift.

In the course of a redshift survey of the HDF-North and its Flanking Fields, [van den Bergh et al. \(2000\)](#) investigated galaxy morphology in this sample of 241 galaxies with spectroscopic redshifts in the range $0.25 < z < 1.2$, concentrating on classification according to the classical Hubble Sequence. They find that grand-design spirals are rare or absent beyond $z \sim 0.3$, that Sa and Sb galaxies do not exhibit well-defined spiral arms anymore beyond $z \approx 0.6$ and that the arms of Sc galaxies are more chaotic than those of their local counterparts. Furthermore, the fraction of late type disks (Sc and Sd) drops from 23% locally to 5% for $z \gtrsim 0.4$ and that bars are extremely rare beyond $z \sim 0.5$ (although it is difficult to distinguish between true bars and triaxial bulges). They note that most intermediate and late-type objects at $z \gtrsim 0.5$ cannot be coerced into the Hubble Sequence and that interacting galaxies become more common with increasing redshift.

Summarising, one may conclude that the Hubble Sequence applies in full detail at $z \lesssim 0.3$, bars disappear and spiral structure becomes underdeveloped at $z \sim 0.5$ and by $z \sim 1$ irregular/peculiar/merger morphologies become dominant among luminous galaxies, while spheroidal galaxies still exist with roughly unchanged number densities to at least $z \sim 1$. Taken together with the evidence from the Tully-Fisher relation and the structural data presented above one may again conclude that massive disks are in place at redshift unity, although their appearance might be very different.

1.1.7 Evolution of clustering and merging

The clustering properties of the spatial distribution of galaxies on scales larger than ~ 0.1 Mpc are usually expressed in terms of the two-point correlation function, $\xi(r)$, or its two-dimensional on-sky projection, $\omega(\theta)$. The evolution of these quantities depends on the background cosmology, the spectrum of primordial density fluctuations out of which structure evolves, and the relation of galaxies to dark matter halos (biasing).

Locally, $\xi(r)$ follows a power-law, $\xi(r) \propto (r/r_0)^\gamma$ with $\gamma \approx 1.7$ and the correlation length r_0 changing with luminosity from $r_0 \sim 4.5$ Mpc at $M_B \sim -18.5$ to $r_0 \sim 8.0$ Mpc at $M_B \sim -22$.

Interpretation of apparent changes seen in $\xi(r)$ with redshift are to be taken with caution, though. Since clustering varies with galaxy type, apparent changes of clustering with time may well reflect a combination of the true evolution of large-scale structure and evolution of the galaxies being observed (including the complication by selection biases).

The most reliable measurements are possible using redshift surveys, since they provide $\xi(r)$ directly without the need to de-project $\omega(\theta)$. The usual parametrisation used is $\xi(r, z) = \xi(r, 0)(1+z)^{-(3+\varepsilon)}$ and $r_0(z) = r_0(0)(1+z)^{-(3+\varepsilon)/\gamma}$, with ε being the evolution parameter ($\varepsilon = \gamma - 3 = -1.3$ clustering fixed in comoving coordinates, $\varepsilon = 0$ clustering fixed in proper coordinates, and $\varepsilon = 0.8$ linear growth).

[Le Fèvre et al. \(1996\)](#) and [Carlberg et al. \(1997\)](#) consistently found a fairly rapid decline in clustering with redshift in the CFRS and the Hawaii K-Sample ([Cowie et al., 1996](#)), respectively. At $z \sim 0.5$, the clustering length was found to be as low

as $r_0(z = 0.5) = 1.5 \pm 0.1$ Mpc, implying $0 < \varepsilon < 2$. Neither analysis took into account the evolution of the luminosity function or was able to quantify the effects of cosmic variance in the small samples. Recently, [Small et al. \(1999\)](#) reported much stronger correlations $r_0(z = 0.3) = 3.7 \pm 0.13$ Mpc for a larger sample.

From the deeper and even larger CNOC2 sample, [Carlberg et al. \(2000\)](#) draw a volume-limited subsample and use the measured evolution of the Luminosity Function ([Lin et al., 1999](#)) to construct an “evolution compensated” sample of 2300 (luminous, $M_R \lesssim -20.3$) galaxies. They, too, find higher clustering at $z = 0.65$, obtaining $r_0 = 5.3 \pm 0.1$ Mpc, $\varepsilon = 0.8 \pm 0.2$ for $\Omega_M = 1$ and $r_0 = 4.85 \pm 0.1$ Mpc, $\varepsilon = -0.81 \pm 0.19$ for a flat $\Omega_M = 0.2$ cosmology. Their selection of intrinsically luminous galaxies at all redshifts makes their result more difficult to interpret in comparison to the CFRS, which contains intrinsically fainter galaxies, though.

On scales smaller than ~ 50 kpc, galaxies will merge on time scales of ~ 1 Gyr so that the evolution of clustering on these scales is highly non-linear. Therefore, the counts of galaxies in close pairs as a function of redshift can be used to quantify the evolution of the merging rate.

Earlier studies used ground-based (e.g., [Zepf & Koo, 1989](#); [Carlberg et al., 1994](#)) or HST-based (e.g., [Burkey et al., 1994](#)) imaging data alone, correcting statistically for counts by projected pairs. Later redshift surveys were used to select dynamical pairs directly ([Yee & Ellingson, 1995](#); [Patton et al., 1997](#)). These studies yielded a wide variety of results. If the merger rate is parametrised as $f_M \propto (1+z)^s$, s was found to be in the range $0 < s < 5$ for $z \lesssim 1$. These discrepancies are most probably due to differences in defining pairs, contamination by projected pairs and spectroscopic incompleteness at close separations.

[Patton et al. \(1997\)](#), analysing pair counts in the CNOC1 redshift survey, showed that the past results were roughly consistent with their value of $s = 2.8 \pm 0.9$ when accounting for these effects.

Recently, [Le Fèvre et al. \(2000a\)](#) used HST imaging data of CFRS galaxies to select spatially and dynamically close pairs to $z \sim 1$ and found that up to 20% of galaxies at $0.75 < z < 1$ are in physical pairs and $s = 2.7 \pm 0.6$, implying that on average an L^* galaxy underwent 0.8 – 1.8 merger events since $z = 1$, with 0.5 to 1.2 merger events happening during a ~ 2 -Gyr time-span around $z \sim 0.9$.

Indeed, [Patton et al. \(2000\)](#) demonstrated that some discrepancies can be attributed to the fact that pair statistics depend on the survey depth, even for volume-limited redshift surveys. For the same reason, flux-limited surveys will exhibit a redshift dependent selection bias. Moreover, any selection effect which changes the mean density of galaxies in the sample, also affects pair statistics.

From the CNOC2 Redshift Survey data, [Patton et al. \(2001\)](#) derive the number of companions per galaxy within a specified range in absolute magnitude, N_c , and the total luminosity in companions, per galaxy, L_c , for pairs with separations $5h^{-1}$ kpc $< r_p < 50h^{-1}$ kpc and $\Delta v < 500$ km s $^{-1}$. N_c is directly related to the galaxy merger rate and L_c can be used to investigate the mass accretion rate, while the influence of selection effects, k -corrections, and luminosity evolution can be modelled for both quantities in a straight-forward manner. They find $N_c = 0.032 \pm 0.008$ and $L_c = 0.029 \pm 0.008 \times 10^{10} h^2 L_\odot$ at $z = 0.3$, for galaxies with $-21 < M_B < -18$. By

comparison with the SSRS2 low-redshift sample they derive $s = 2.3 \pm 0.7$ and that the mass accretion rate is proportional to $(1+z)^{2.3 \pm 0.9}$, with 15% of present epoch $\sim L^*$ galaxies having undergone a major merger since $z = 1$.

1.1.8 Lyman-break galaxies

Simultaneously to the extensive study of galaxies at $z \lesssim 1$, the study of Lyman-Break Galaxies (LBGs) selected by drop-out techniques (Steidel & Hamilton, 1992, 1993; Steidel et al., 1995) and subsequent spectroscopic confirmation (Steidel et al., 1996) provided us a first picture of the galaxy population at redshifts $2.5 \lesssim z \lesssim 4.5$. In this early epoch galaxies seem to have mostly irregular and patchy morphologies (Giavalisco et al., 1996) and small physical sizes (Lowenthal et al., 1997), suggesting that the Hubble Sequence present to redshifts of slightly above unity must have appeared in the redshift range $1.5 \lesssim z \lesssim 2.5$. LBGs exhibit strong angular clustering comparable to that of present day luminous spirals (Giavalisco et al., 1998).

Pettini et al. (2001) present near-infrared spectra of LBGs aimed at detecting the emission lines of [O II], [O III], and $H\beta$. From a sample of ~ 20 objects they reach the following main conclusions. The rest-frame optical properties of LBGs at the bright end of the luminosity function are remarkably uniform, their spectra are dominated by emission lines, [O III] is always stronger than $H\beta$ and [O II], and projected velocity dispersions are between 50 and 115 km s^{-1} . It seems well established that LBGs are the most metal-enriched structures at $z \sim 3$, apart from quasi-stellar objects, with abundances greater than about 1/10 solar and generally higher than those of damped Ly- α systems at the same epoch. The velocity dispersions imply virial masses of about $10^{10} M_{\odot}$ within half-light radii of 2.5 kpc. The corresponding mass-to-light ratios, $\mathcal{M}/L \sim 0.15$, are indicative of stellar populations with ages between 10^8 and 10^9 yr, consistent with the UV-optical spectral energy distributions. However, Pettini et al. (2001) are unable to establish conclusively whether or not the widths of the emission lines reflect the motions of the H II regions within the gravitational potential of the galaxies, since rotation curves could not be observed.

Papovich et al. (2001) investigate the stellar populations of 33 LBGs selected from the HDF by comparison with stellar population synthesis models. They find equivalent ages of 30 Myr to 1 Gyr, a wide range of star formation rates $10^{-2} < SFR < 10^3$, and extinctions of $A(1700\text{\AA}) \sim 1.5$ mag with only a few galaxies being younger and strongly reddened. No galaxies are found to be young and dust free. They find estimates for the minimum stellar masses of LBGs to be $\sim 10^{10} M_{\odot}$, roughly 0.1 of a present day L^* galaxy and an upper bound for the stellar mass of a factor 3–8 that value. This indicates that dynamical mass estimates using line widths may be underestimating the total mass considerably.

It is yet unclear what the fate of these LBGs is. Their clustering suggests they end up in today's massive galaxies while the wide range in star formation rates and other properties rather suggests they represent a much more heterogeneous population. Some might be the building blocks of today's massive galaxies, while others might fade into low-luminosity dwarf systems.

Unfortunately, linking the observations at $z \lesssim 1$ to those at $z \gtrsim 2.5$ is not yet possi-

ble mainly due to the spectroscopic “gap” around redshifts of ~ 2 . Even more so, most evidence presented above suggest that crucial steps in the formation of today’s galaxy population has taken place just in this dark window.

1.2 The theoretical side

The current theoretical standard paradigm of galaxy formation and evolution is that galaxies form within gravitationally collapsed dark matter halos and that merging is the dominant process governing their subsequent evolution (e.g., Cole et al., 2000; Pearce et al., 2001; Kauffmann et al., 1993 and references therein). This paradigm is called hierarchical galaxy formation.

Galaxies are assumed to initially form as disks from gas which cools within the potential well of a dark matter halo. The merging of this halo with other halos governs the subsequent evolution of the galaxy. The merging histories of the halos (“merger trees”) are either taken from N-body simulations directly or generated by Monte-Carlo techniques.

Fully simulating the physics of gas and star formation is not yet possible due to computational limits, but also due to a lack of understanding of processes involved in star formation and energy feedback from supernovae. Therefore, many authors use heuristic descriptions of these processes in so called semi-analytic models to describe the behaviour of baryonic matter within the halos.

1.2.1 Gas and star formation

Gas is usually split into a hot phase and a cold phase. Hot gas cools from the virial temperature of the halo on a time scale determined by the thermal energy density and the cooling rate per unit volume. The latter depends on the specific cooling function of the gas, including effects of temperature and metallicity.

Cold gas can turn into stars if its surface density in the disk is above a certain limit. The star formation rate depends on the total mass of cold gas, the dynamical time scale of the galaxy, and a star formation efficiency being treated as a free parameter. Energy ejected by supernovae is partly re-heating the gas of the interstellar medium to the virial temperature of the surrounding dark matter halo. The efficiency of this process, being ill-constrained, is also treated as a free parameter.

1.2.2 Evolution of galaxies

Following the merger trees, halos merge to form halos of larger mass. It is important to emphasize that the galaxies belonging to each halo do not necessarily also merge. The central galaxy of the largest predecessor halo becomes the central galaxy of the newly formed halo, while the other galaxies become its satellites.

All available hot gas is assumed to be shock-heated to the virial temperature of the new halo, and subsequently to cool and to be accreted only by the central galaxy. Accretion of cold gas by the satellites is cut off, and star formation within them continues only until their reservoir of cold gas is exhausted.

The satellite galaxies experience dynamical friction while orbiting the central object. This sets the time scale for the accretion of the satellites by the central galaxy. If the mass ratio between the central object and an infalling satellite exceeds a critical fraction, typically around 0.3, the merger is termed a major merger, otherwise it is a minor merger.

Major mergers produce spheroidal remnants. The disks are destroyed and all cold gas available is turned into stars in a starburst during the merger. The remnant in such a merger is an elliptical galaxy. Minor mergers do not trigger such morphological transformations. During a minor merger, the stars of the satellite are simply added to the central galaxy and the cold gas is accreted by the central disk.

During further mergers between halos the reservoir of hot gas grows and cools onto the central galaxy being added to its disk, or forming a new disk if the central object just underwent a major merger. This way, elliptical galaxies can accrete new disks and thus become the bulges of spiral galaxies.

1.2.3 Linking with observations

The hierarchical models predict galaxy number densities, circular velocities, mass distributions as a function of redshift, star formation rates, and by means of the incorporated stellar population synthesis models also luminosities and colours.

The models can therefore be compared to a number of observational constraints like B and K luminosity functions, galaxy colour distributions, the scaling relations, galaxy number counts, redshift distributions etc.

Some observables like luminosity functions and redshift distributions are rather well matched for $z = 0$ (e.g. Cole et al., 2000), while the scaling relations of spiral galaxies still remain problematic in the sense that the galaxies are predicted to have too large a surface brightness (and thus being too compact) at a given circular velocity. It is still unclear how the predictions of the models match observations at $z \neq 0$ as data is still sparse.

Also, the properties of elliptical galaxies still remain a major challenge to hierarchical models. Observations as those mentioned in Sect. 1.1.2 and in Sect. 1.1.3 point to large formation redshifts of the stellar populations of these objects. Hierarchical models might be able to reproduce the number density of spheroids, but always tend to yield bluer colours.

The bottom line may be that current modelling of galaxy formation and evolution within the framework of a cold dark matter dominated cosmology makes strong predictions concerning the masses of collapsed objects and their evolution because gravitational evolution of the dark matter dominates this process and can be assessed analytically as well as numerically using N-body simulations. At the same time, the model predictions concerning the evolution of the visible baryonic part of the galaxies are much weaker as these are based on the poorly-understood problems of gas cooling, fragmentation and star formation which can be treated only heuristically in the models. Since mass is hardly directly observable in this context (as weak gravitational lensing surveys are not sensitive enough), yet light is, we are in the situation of being able to model and predict well what we can hardly observe and vice versa.

1.3 Outline

This work is organized as follows.

In Chapter 2 we introduce the Munich Near-Infrared Cluster Survey (MUNICS), a K -band selected photometric survey for distant galaxies. The survey utilises multi-colour imaging in the near-infrared K and J bands, as well as complementary photometry in the optical I , R , and V bands. A spectroscopic follow-up programme is also presented. We motivate the undertaking of such a survey, discuss the survey's technical design, its sensitivity limits, the survey fields, and finally the reduction of the imaging data.

In Chapter 3 we discuss a newly developed software package for automated object detection, photometry, and classification. This package is customised to fit the needs of the MUNICS survey, especially to deal with non-uniform data sets. The algorithms used are presented in detail and the performance of the package is compared to other available products.

The construction of photometric catalogues from the reduced images is the topic Chapter 4. The individual steps in this process are described in detail. First, the choice of optimal parameters for object detection is discussed, taking into account their effect on the number of false detections. Then the multi-colour photometry process and the star-galaxy separation are described.

Secondly, a thorough analysis of the survey's completeness (Sect. 4.5) with respect to point-like sources, disk galaxies and de Vaucouleurs profiles is given. Here we use realistically simulated galaxies following the known scaling relations between surface brightness and effective radius to discuss the detection efficiency and the reliability of the measured total magnitude as a function of radial light profile and redshift. These results are discussed in the context of visibility theory and various selection biases found are explained in this context.

Finally, this chapter is concluded by a comparison of number counts for galaxies with previous studies (Sect. 4.6) as a further consistency check on our data set, and a first look at colour-colour and colour-magnitude diagrammes (Sect. 4.7).

Chapter 5 aims at a measurement of the evolution of the rest-frame K -band luminosity function of field galaxies at $0.4 < z < 1.2$.

After introducing the sub-sample of field galaxies selected from the MUNICS catalogues, a photometric redshift estimation technique is introduced in Sect. 5.3. We calibrate the technique using spectroscopically determined redshifts and describe the construction of an optimal library of template spectra.

As a first application we discuss the cumulative redshift distribution of galaxies and compare the data to predictions from hierarchical galaxy formation models (Sect. 5.4).

Sect. 5.5 and Sect. 5.6 present the method used for estimating the luminosity function and discuss the results obtained for the total luminosity function as well as the type-dependent luminosity function and their consequences for the understanding of galaxy formation.

In Chapter 6 we conclude with a measurement of the stellar mass functions of galaxies at $0.4 < z < 1.2$. We use two approaches to model the mass-to-light ratio of galaxies, a pure luminosity evolution model maximising the stellar mass at all redshifts

presented in Sect. 6.2, and a model based on individual fits of composite stellar populations to the multicolour photometry presented in Sect. 6.3. Finally, we compare and discuss the results obtained from these approaches in Sect. 6.4.

Chapter 2

The Survey

Directly observing the evolution of individual galaxies with time is, unfortunately, not possible. Therefore we must rely on investigating the statistical properties of the whole galaxy population as a function of redshift, trying to draw conclusions from ensemble properties on the evolution of typical members of these ensembles, and thus facing difficulties, like, for example, discriminating between luminosity evolution and number density evolution.

Much work has been invested in this field, resulting in a lot of progress in the last decade which has seen many imaging and redshift surveys being undertaken using different selection techniques in wave-bands from the UV to the sub-mm. These surveys have a wide range of scientific applications, from the detection of high-redshift galaxy clusters to the study of the evolution of ‘normal’ field galaxies.

This chapter begins with a motivation of undertaking K -band selected surveys of distant galaxies (Sect. 2.1). Then, in Sect. 2.2, we describe the scientific aims, the limiting sensitivities, the selection of survey fields, and the photometric system of the Munich Near-IR Cluster Survey (MUNICS). Finally we describe the observations in the near-infrared and optical wavelength regimes, and the reduction of the data and their calibration in Sect. 2.3.

2.1 Motivation

The earlier optically and near-IR selected redshift and imaging surveys, among others [Broadhurst et al. \(1988\)](#), [Colless et al. \(1990\)](#), [Lilly et al. \(1991\)](#), [Glazebrook et al. \(1994\)](#), and [Cowie et al. \(1994\)](#), laid the path to the landmark CFRS ([Lilly et al., 1995a](#)), an I -band selected redshift survey mapping the evolution of the galaxy population out to $z \sim 1$. Also many ‘pencil-beam’ surveys have been carried out, the most prominent being the Hubble Deep Field North and South ([Williams et al., 1996, 2000](#)) and their ground-based imaging and spectroscopic follow-ups, allowing us a first glimpse at the galaxy population at $2.5 \lesssim z \lesssim 4.5$. The inability to determine redshifts spectroscopically for all objects where multi-band imaging data is available (because of limited telescope resources, either in observing time or in collecting area), caused photometric redshift determination techniques to gain attention again ([Baum,](#)

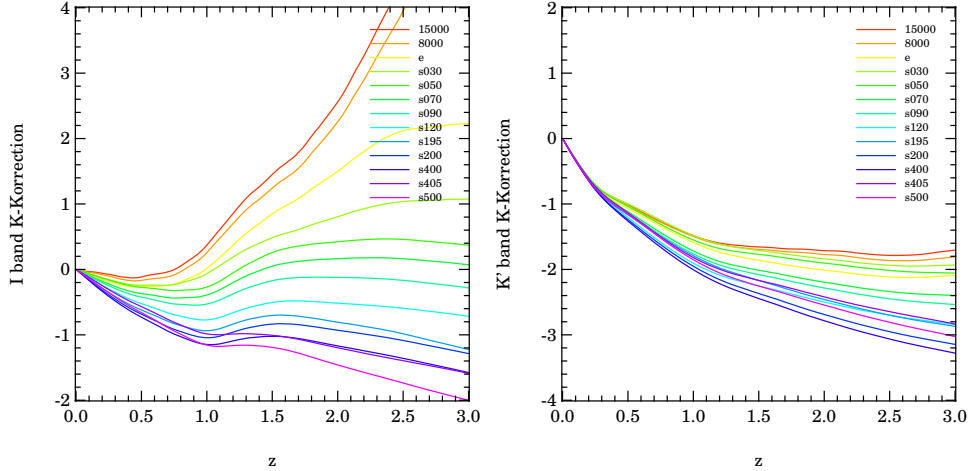


Figure 2.1: Comparison of the k -corrections for the I band (left panel) and K band (right panel) for a range of galaxy SEDs from early to late type.

1962; Koo, 1985; Fernández-Soto et al., 1999; Benítez, 2000). This, and the wide-field imagers becoming available in the optical and also in the near-infrared wavelength regime, made multi-band imaging surveys a very promising option for further studies in galaxy evolution.

Selection in a single pass-band introduces different (and sometimes subtle) selection effects, a well-known fact which need not necessarily be considered at the disadvantage of the resulting object database, as long as the selection function is well-understood and under control. These selection effects can be used deliberately for probing different galaxy populations and different aspects of their evolution. While selection in blue pass-bands is used to study star forming sources, selection in the near-IR is predominantly sensitive to the light of old stellar populations. Near-IR k -corrections are small even at redshifts above unity and insensitive to the spectral type of the observed objects (Cowie et al., 1994) and to short-lived bursts of star formation, as has been pointed out by Kauffmann & Charlot (1998). The former is demonstrated in Fig. 2.1 in which the k -corrections of a range of galaxy SEDs are plotted as a function of redshift both for the K and the I -band. The latter is shown in Fig. 2.2 which compares the B -band and the K -band magnitude of a galaxy of given stellar mass for different star formation histories.

Thus near-IR selected surveys are thought to be much less biased with respect to the mix of spectral types compared to optically selected surveys. Furthermore, the uncertainties resulting from inhomogeneous dust absorption are minimal in the near-IR. It has therefore been concluded that near-IR selection is a feasible attempt at a selection in stellar mass (Rix & Rieke, 1993; Brinchmann & Ellis, 2000).

The Munich Near-Infrared Cluster Survey (MUNICS) is an attempt at closing the gap between previously undertaken infrared-selected deep pencil-beam surveys (Gard-

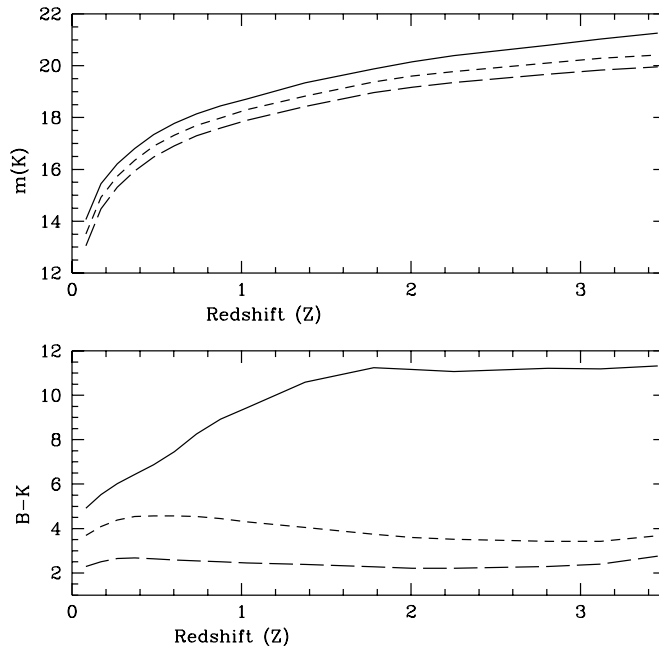


Figure 2.2: Apparent K -band magnitude of galaxy with $10^{11}M_{\odot}$, observed at redshift z as function of star formation history: SSP (solid), $SFR = const$ (short dashed), and ‘starburst’: 80% of stars formed at constant rate, 20% in 10^8 yr before observation (long dashed). Taken from [Kauffmann & Charlot \(1998\)](#).

ner et al., 1993; McLeod et al., 1995; Cowie et al., 1994; Djorgovski et al., 1995; Williams et al., 1996; Saracco et al., 1997) and relatively shallow wide-area surveys (Mobasher et al., 1993; Glazebrook et al., 1994; Gardner et al., 1997), simultaneously profiting from the advantages of near-infrared selection.

MUNICS is a wide-area, medium-deep, photometric survey selected in the K' band. One part of the surveyed fields was centred on known quasars, while the rest was randomly selected at high Galactic latitudes. It covers an area of roughly one square degree in the K' and J bands with optical follow-up imaging in the I , R , and V bands for a large fraction of the total surveyed area.

The resulting object catalogues are strictly selected in K' with a limiting magnitude of $K' \sim 19.5$ mag and $J \sim 21$ mag, sufficiently deep to detect passively evolving systems up to a redshift of $z \lesssim 1.5$ and luminosity of $0.5L^*$ (see Fig. 2.3). The optical data reach a depth of roughly $R \sim 23.5$ mag.

2.2 Survey concept and layout

2.2.1 Scientific aims

The project’s main scientific aims are the following. First, to identify clusters of galaxies at high redshift by detecting their luminous early-type galaxy population. As has

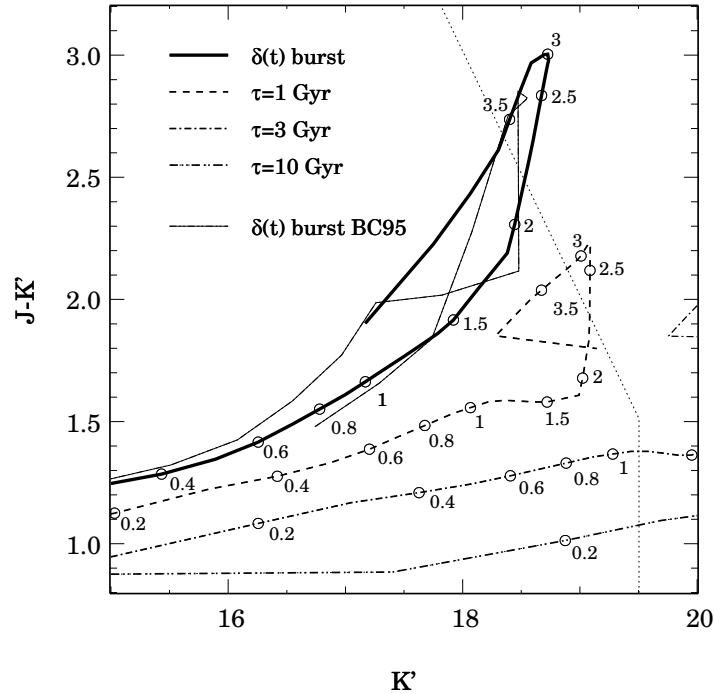


Figure 2.3: Stellar population synthesis models in the $J-K'$ vs. K' plane for different star-formation histories, a $SFR(t) \propto \delta(t)$ burst at $z = 4$, and 3 exponential star formation rates $SFR(t) \propto \exp(t/\tau)$ with $\tau = 1, 3,$ and 10 Gyr, setting in at $z = 4$. The models are normalised to have a luminosity of L_B^* at the present epoch, according to the type-dependent luminosity function of the Virgo cluster (see text) as given by Sandage, Binggeli, & Tammann (1985). The thin dotted line indicates the limiting depth (50 per cent completeness) of the MUNICS data in J and K' . The adopted cosmology is $H_0 = 65, \Omega_0 = 0.3, \Omega_\Lambda = 0.7$. The SSP models used in the synthesis are from Maraston (1998). Additionally, an SSP model by Bruzual & Charlot (1995) is shown for comparison as a thin solid line.

been shown in the last years, the early-type galaxy population in clusters is well in place at redshifts of at least 0.8 (Stanford et al., 1995, 1997, 1998; de Propris et al., 1999). Given the small k -corrections in the K band, this makes selection in the near-IR a promising approach to detect clusters at redshifts around unity, complementing selection in other optical bands. Clusters of galaxies allow to find large numbers of massive galaxies at higher redshift and thus represent unique laboratories to study the evolution of galaxies in high-density regions as a function of redshift, and in contrast to the evolution of similar galaxies in the field. Furthermore, the evolution of the number density of clusters is a promising test of cosmological models, depending sensitively on the density parameter Ω_0 (Eke et al., 1996; Bahcall et al., 1997; Bahcall & Fan, 1998; Eke et al., 1998). While the number of clusters known at redshifts $z > 0.5$ is steadily increasing (mostly due to X-ray selection), samples selected *uniformly* in the optical and near-IR wavelength ranges are still deficient.

Cluster detection at high redshifts is strongly biased towards the most massive systems, mainly because of the lack of detection sensitivity for lower mass systems. Finding also less massive systems is important when reasoning about hierarchical galaxy formation models, since the galaxies in the densest environments formed earlier, so by looking only at the most dense environments one is effectively pushing the epoch of collapse, merging, and star formation out to higher redshifts and further away from the observational window. Therefore we decided to centre a subset of the MUNICS fields on known quasars hoping to increase the chance of detecting clusters in their environment.

Secondly, a statistically well-defined sample of the early-type galaxy population *in the field* can be constructed from our catalogues, which will be used to study the evolutionary history of such objects in the redshift range $0 < z < 1$ by means of the K -band selected luminosity function, the luminosity density at near-infrared wavelengths, and the two-point correlation function. Again, K -band selection offers unique opportunities due to the close connection between near-IR luminosity and stellar mass (Brinchmann & Ellis, 2000), and thus allows direct assessment of the predictions of hierarchical galaxy formation theories.

Early-type galaxies (meaning here massive galaxies: ellipticals, lenticulars and early-type disk galaxies of luminosities around and greater than L^*) are those objects which are most likely to give insights into the processes dominating the formation of the Hubble Sequence. This is because the predictions for their evolution are stronger than for less massive systems in the standard CDM scenario (Baugh et al., 1996; Arag3n-Salamanca et al., 1998; Kauffmann & Charlot, 1998; Cole et al., 2000), and also because they are most easily detectable at $1 \lesssim z \lesssim 2$. It is still unclear if massive bulges and elliptical galaxies formed through hierarchical merging of smaller sub-units over an extended period, with the most massive objects forming later than less massive systems (in the same environment) as predicted by the CDM models, or, if such systems formed the bulk of their stars during a monolithic collapse at high redshift, as is indicated by analysis of their stellar population. Furthermore, it is not known what role star formation actually has during mergers. The study of the evolution of these objects will be the main issue addressed in this work.

Thirdly, the nature of Extremely Red Objects (EROs; Elston et al., 1988; Hu & Ridgway, 1994) will be examined. EROs, usually defined in terms of $R-K$ greater than or approximately equal to 5 at moderately faint K -band magnitudes of $K \geq 18$, are thought to be either high-redshift early-type galaxies or heavily extinguished starburst galaxies (Cimatti et al., 1999; Smail et al., 1999), the relative contribution of the two sub-populations being yet highly uncertain. Due to the small areas of the surveys available so far, even the surface density of these objects is not reliably known (Thompson et al., 1999). Since they mostly are R -band ‘dropouts’, having the possibility to detect such objects in the MUNICS data in the I and J bands, together with the large field covered, will enable us to gain valuable information on their nature.

2.2.2 Limiting sensitivity

Fig. 2.3 shows stellar population synthesis models in the $J-K'$ vs. K' plane for different star-formation histories, a $SFR(t) \propto \delta(t)$ Simple Stellar Population (SSP), and 3 exponential star formation rates $SFR(t) \propto \exp(t/\tau)$ with $\tau = 1, 3,$ and 10 Gyr. The onset of star formation occurs at $z = 4$ in all models. The populations are normalised to have a luminosity of L_B^* at the present epoch, according to the type-dependent luminosity function of the Virgo cluster as given by Sandage et al. (1985). The adopted values for M_B^* are $M_B^* = -21.5$ for the SSP model (elliptical/S0 galaxy), $M_B^* = -20.5$ for $\tau = 1$ (Sa–Sb spiral), $M_B^* = -19.5$ for $\tau = 3$ (Sc), and $M_B^* = -17.5$ for $\tau = 10$ (Sd and later). The cosmology is $H_0 = 65 \text{ km s}^{-1} \text{ Mpc}^{-1}$, $\Omega_0 = 0.3$, $\Omega_\Lambda = 0.7$.

The SSP models are taken from Maraston (1998). The distinguishing feature of that synthesis method is the adaption of the fuel consumption theorem to evaluate the energetics of the post main-sequence evolutionary phases. The models used here have solar metallicity and ages ranging from 30 Myr to 15 Gyr. The IMF is a power law $\Psi(M) \propto M^{-(1+x)}$ with Salpeter exponent $x = 1.35$ down to a lower mass limit of $0.1M_\odot$. The optical and infrared colours predicted by these SSP models are calibrated against Milky Way and Magellanic Cloud globular clusters and are compared to similar models from the literature in Maraston (1998). Fig. 2.3 also shows an SSP model by Bruzual & Charlot (1993) using the 1995 version of their code, with solar metallicity and a Salpeter IMF. The models evolve similarly up to redshifts of $z \sim 1$. The differences in colour are likely due to the different treatment of the post main sequence stages and are discussed in Maraston (1998).

Following the predictions of these models, the limiting magnitudes in the near-IR wave-bands have been chosen to be 19.5 mag in K' and 21.0 mag in J , such that early-type objects having luminosities of $\gtrsim 0.5L^*$ at the present epoch can be detected in K' virtually at any redshift, and in J up to a redshift of $z \lesssim 1.5$, assuming passive evolution.

This is in agreement with the findings of the CFRS, which has shown that, while the luminosity function of the population of blue field galaxies shows significant signs of evolution in the redshift range $0.2 < z < 1$ – explainable by brightening or increase in space density – the redder part of the population (roughly redder than Sbc) shows no signs of evolution of its luminosity function in the same redshift range (Lilly et al., 1995b). The latter is interpreted in terms of brightening of the individual galaxies through passive evolution counterbalanced by negative density evolution, such that the luminosity function of the early-type population effectively does not evolve.

2.2.3 Field selection

The MUNICS survey consists of two sets of near-IR target fields, one set of single camera pointings having an effective field of view of $6' \times 6'$ pointed towards quasars, and a second set of $28' \times 13'$ fields constructed from mosaics of pointings targeted at random high Galactic latitude fields. This second set of fields was selected to contain no bright stars, nearby bright galaxies, and known nearby clusters of galaxies, and furthermore, to have low Galactic reddening (which is all together difficult to accomplish

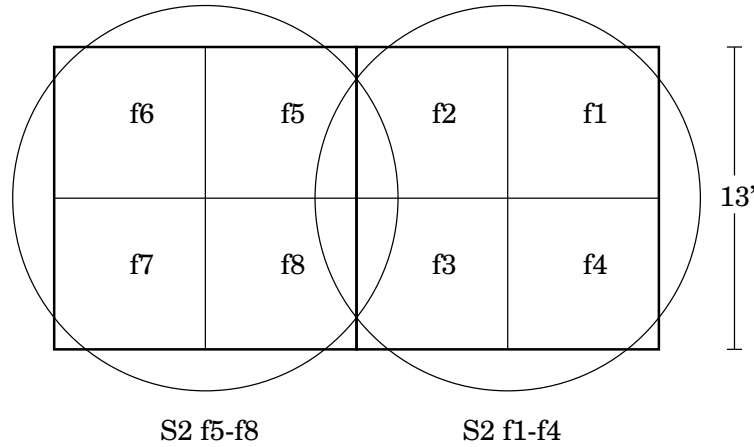


Figure 2.4: Layout and nomenclature of one of the MUNICS ‘mosaic fields’. The size of the stripe is $13' \times 28'$, covered by 2×4 pointings in the near-IR and two pointings in the optical with the circular field of view of CAFOS (see text). The IR image is divided for technical reasons into two 2×2 mosaics. Each optical frame and IR mosaic frame are denoted by the name of the stripe, here S2, followed by the subfields they cover, giving S2 f1...f4 and S2 f5...f8 for this stripe.

together with the prerequisite of having no bright star within the field, given our field size).

A total of 16 fields targeted towards quasars with redshifts $0.5 < z < 2$ were observed. These fields will be referred to as ‘quasar fields’ hereafter, labelled Q1...Q16. The quasars were selected from the seventh edition of the [Veron-Cetty & Veron \(1996\)](#) catalogue. The selection criteria were $B < 19.0$ mag, $0^\circ < \text{Dec} < 65^\circ$, $0^{\text{h}} < \text{RA} < 18^{\text{h}}$, and $0.5 < z < 2$. Six of these quasars are not detected in the radio bands of the catalogue (6 cm and 11 cm) and are therefore considered radio quiet. The remaining 10 are radio loud.

A second set of 7 fields was targeted at high Galactic latitude ‘empty’ fields, i.e. free of bright stars ($V < 17$ mag) and known nearby extragalactic objects. These fields will be called ‘mosaic fields’ hereafter, for they are mosaiced images in the near-IR. They are labelled S1...S7. Each such field is laid out as a stripe of 4×2 IR pointings, yielding an area of $28' \times 13'$. For technical reasons, namely that four near-IR pointings can be completed in K' and J during a single night as well as image size and efficiency of optical follow-up observations (see below), each such stripe is divided into two 2×2 mosaics of single IR frames, denoted f1–f4 and f5–f8. This particular geometry was chosen for efficiency since such a 2×2 mosaic of IR frames suits the circular field of view of the optical imager we used (CAFOS, having a diameter of roughly 16 arcmin; see Sect. 2.3.2). For clarity, Fig. 2.4 shows a sketch of the geometry and nomenclature of the mosaic fields.

Finally, Tables 2.1 and 2.2 lists the coordinates, available pass-bands, seeing, and Galactic foreground extinction of the observed mosaic and quasar fields, respectively.

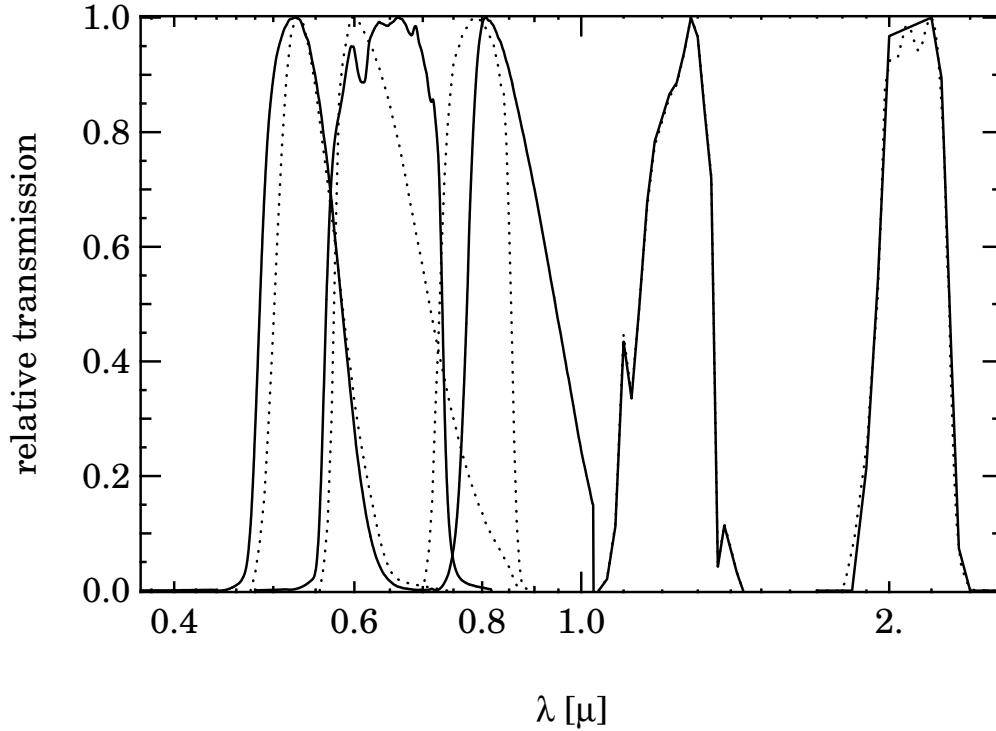


Figure 2.5: Relative transmission of the MUNICS $V, R, I, J,$ and K' filter (solid curves) curves including quantum efficiency of the CCD ($V, R,$ and I) and the Rockwell HAWAII near-IR array (J and K'), as well as the atmospheric transmission in the near-IR. Relative transmission curves of standard Johnson-Kron-Cousins $V, R,$ and I filters, as well as J and K' are shown for comparison (dotted curves).

2.2.4 Photometric system

The MUNICS imaging observations were carried out partly using non-standard filters, or imperfect realisations of standard filters (see Sect. 2.3 below). Since the colours of objects in the MUNICS catalogues extend to much redder colours than any available photometric standard stars, we decided to work in the MUNICS instrumental photometric system and not to transform magnitudes into the standard Johnson-Kron-Cousins system. Linear transformation to the Johnson-Kron-Cousins system would have caused magnitude errors up to 1 mag, because the true transformations are highly non-linear, especially for red objects. The MUNICS photometric zero-points are in the Vega system.

Note that, since comparison of the object's colours with spectral synthesis models is intended (e.g. for deriving photometric redshifts or discussing the nature of EROs), it is important that the observed colours and the synthetic colours are consistent with respect to the filter set.

Accurate measurements of the transmission curves of the glass filters and quantum efficiencies of the detectors were obtained and applied in all subsequent synthetic photometry. The filter curves are shown in Fig. 2.5.

Such accurate knowledge of the filter system allows a reliable calibration of different bands via colour–colour diagrammes of stars which are compared with synthetic stellar sequences obtained from the convolution of SEDs from stellar libraries with the transmission curves. The absolute photometric zero-points can then be derived from a single photometric observation in one band only.

Fig. 2.6 shows a comparison of colours derived by convolving stellar SEDs with the MUNICS filter curves with a sample of stars detected in the MUNICS mosaic fields. The stellar SEDs used for computing the synthetic colours are taken from the Bruzual-Persson-Gunn-Stryker spectral library (Gunn & Stryker, 1983; Strecker et al., 1979), covering spectral types O5 to M8. The agreement between the synthetic photometry and the data along the stellar loci in colour–colour space demonstrates that the constructed filter curves match the actual ones and that the photometric zero-points are mutually consistent in the optical and the near-IR regime (see also Sect. 2.3.2 and Sect. 2.3.1). It is worth noting that we have no cool giants or supergiants in the MUNICS sample (as those would occupy a redder sequence in $J-K$ at $R-I \gtrsim 1.5$) and no stars of earlier type than roughly late F to G. The details of the photometric calibration procedure are described below in Sect. 2.3.4.

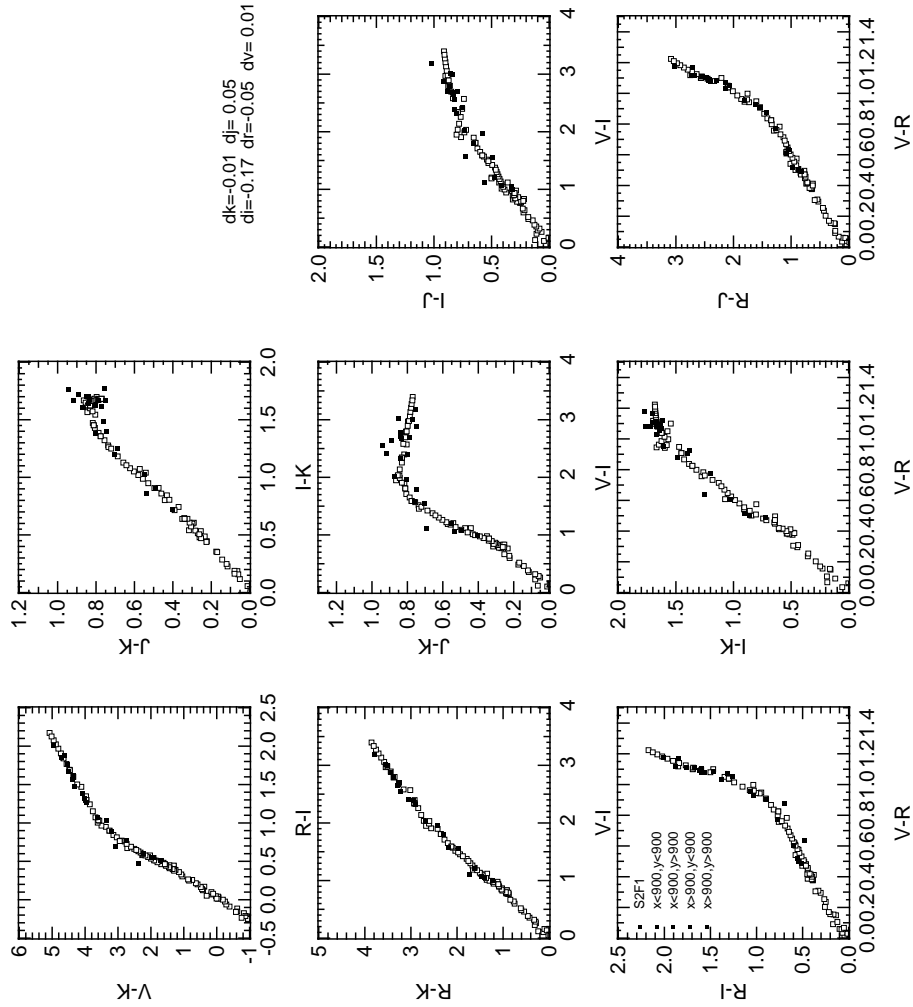


Figure 2.6: Comparison of colours derived by convolving stellar SEDs (see text) with the MUNICS filter curves (open symbols) with a sample of stars identified in the MUNICS field S2 f1–f4 (filled symbols).

2.3 Observations and data reduction

2.3.1 Infrared observations and data reduction

The K' -band and J -band imaging was obtained using the Omega-Prime camera (Bizenberger et al., 1998) at the prime focus of the Calar Alto 3.5-m telescope. Omega-Prime is equipped with a HAWAII 1024² HgCdTe array. The image scale is 0.396 arcsec per pixel, resulting in a $6.75' \times 6.75'$ field of view. The K' filter ($\lambda_0 = 2.12\mu$, $\Delta\lambda = 0.35\mu$; see Wainscoat & Cowie, 1992) was used because it significantly reduces the thermal background seen by the detector relative to the standard K filter, thus gaining sensitivity. Table 2.3 lists all observing runs undertaken to present date.

The K' -band data were observed using a dithering pattern consisting of 16 positions within an area of $30'' \times 30''$ laid out on a 4×4 grid with $10''$ spacing between adjacent grid points. The data were recorded using a randomised sequence of these 16 positions.

On each position 28 seconds of net exposure time were collected, divided into several shorter exposures as necessary depending on the ambient temperature and thus the level of the thermal background. The length of the single exposures was always chosen such that non-linearity of the detector was negligible.

This 16 position cycle was repeated 3 times yielding 48 frames and a total exposure time of 1344 s. The J -band images were observed using the same dithering pattern with longer integration times of 80 s on each position and therefore needed only one cycle, giving a total of 1280 s.

The near-IR mosaic fields consist of four such Omega-Prime pointings arranged in a 2×2 configuration with $6'$ offset in each direction measured from field centre to field centre. Each mosaic then covers a total area of 162 square arc minutes, counting only the central area with the longest total exposure time and removing overlaps and borders due to the dithering pattern (see Fig. 2.4).

On photometric nights, standard stars from the UKIRT Faint IR Standard Stars catalogue (Casali & Hawarden, 1992) were observed several times during the night at different air masses to determine the photometric zero point and the atmospheric extinction coefficient. To increase the number of standard star measurements available for each night, the calibrations of further stars in the UKIRT fields by Hunt et al. (1998) were included. Night-to-night variations in the zero-point were typically less than 0.1 mag. Targets observed during non-photometric nights were re-observed (with shorter exposure time) at least once during photometric conditions to assure accurate photometric calibration. The typical formal uncertainties in the zero-points were 0.05 mag in K' and 0.06 mag in J . The extinction coefficients were found to be stable for all runs with typical values around 0.08 ± 0.025 mag per airmass in K' and 0.12 ± 0.02 mag per airmass in J . By comparison with synthetic photometry as explained in Sect. 2.2.4 we conclude that additional systematic errors in the near-IR calibration as well as systematic offsets between the near-IR and the optical wave-bands cannot be larger than ~ 0.1 mag.

The data were reduced using standard image processing algorithms within IRAF¹.

¹IRAF is distributed by the National Optical Astronomy Observatories, which are operated by the As-

Field	Mosaic	Short name	α (J2000)	δ (J2000)	Filters	K' seeing	$E(B-V)$	Remarks
S1	f1-f2	S1F1	14:49:25	+65:55:31	KJIRV	1.01"	0.017	NIR mosaic incomplete
S2	f1-f4	S2F1	03:06:41	+00:01:12	KJIRV	1.30"	0.080	Good data in all five wave-bands
	f5-f8	S2F5	03:06:41	-00:13:30	KJIRV	1.17"	0.083	Good data in all five wave-bands
S4	f1-f4	S4F1	03:15:00	+00:07:41	KJIRV	0.95"	0.094	NIR data quality poor
	f5-f8	S4F5	03:14:05	+00:07:41	KJIRV	2.52"	0.094	NIR data quality poor
S3	f1-f4	S2F1	09:04:38	+30:02:56	KJIRV	1.10"	0.025	Good data in all five wave-bands
	f5-f8	S2F1	09:03:44	+30:02:56	KJIRV	1.11"	0.027	Good data in all five wave-bands
S5	f1-f4	S2F1	10:24:01	+39:46:37	KJIRV	1.17"	0.012	Good data in all five wave-bands
	f5-f8	S2F1	10:25:14	+39:46:37	KJIRV	1.32"	0.009	Good data in all five wave-bands
S6	f1-f4	S2F1	11:55:58	+65:35:55	KJIRV	1.21"	0.019	Good data in all five wave-bands
	f5-f8	S2F1	11:57:56	+65:35:55	KJIRV	1.41"	0.015	Good data in all five wave-bands
S7	f1-f4	S2F1	13:33:41	+16:51:44	KJ	1.68"	0.023	NIR data quality poor
	f5-f8	S2F1	13:34:44	+16:51:44	KJIRV	1.12"	0.029	Good data in all five wave-bands

Field coordinates are given with respect to the image centres.

Table 2.1: The MUNICS Mosaic Fields

Field	QSO	z_{QSO}	α (J2000)	δ (J2000)	Filters	K' seeing	$E(B-V)$	Remarks
Q1	J000701.3+002242	0.87	00:07:01	+00:22:42	KJIR	1.39"	0.073	PB 5741; Radio quiet
Q2	J000750.9+031733	1.10	00:07:51	+03:17:32	KJIR	1.07"	0.020	PB 5753; Radio quiet
Q3	J005444.0+144646	0.91	00:54:44	+14:46:47	KJIR	1.30"	0.054	PHL 892; Radio quiet
Q4	J005905.6+000651	0.72	00:59:06	+00:06:52	KJIR	1.00"	0.027	PHL 923
Q5	J010026.8+043941	0.53	01:00:27	+04:39:41	KJIR	1.06"	0.024	UM 81; Radio quiet
Q6	J011033.7+015446	0.71	01:10:35	+01:55:37	KJIR	1.29"	0.028	MS 01080+0139; Radio quiet
Q7	J011818.5+025806	0.67	01:18:19	+02:58:06	KJIR	1.23"	0.039	3C 37
Q8	J015838.9+034744	0.66	01:58:39	+03:47:43	KJIR	1.23"	0.031	UM 153; Radio quiet
Q9	J025937.5+003736	0.53	02:59:38	+00:37:37	KJIR	1.33"	0.090	US 3472
Q10	J115517.9+653917	1.20	11:55:28	+65:38:10	KJIRV	1.62"	0.017	4C 65.13
Q11	J122033.9+334312	1.51	12:20:34	+33:43:10	KJ	1.22"	0.012	3C 270.1
Q12	J133335.8+164904	2.08	13:33:40	+16:48:14	KJ	1.86"	0.022	PB 3977
Q13	J133411.6+550125	1.25	13:34:12	+55:01:25	KJ	1.59"	0.007	4C 55.27
Q14	J135704.5+191906	0.71	13:57:05	+19:19:07	KJ	1.72"	0.060	PKS 1354+19
Q15	J135817.6+575205	1.38	13:58:18	+57:52:05	KJ	1.89"	0.010	4C 58.29
Q16	J171938.4+480413	1.08	17:19:38	+48:04:13	KJ	1.79"	0.019	PG 1718+481

Field coordinates are given with respect to the image centres.
 QSO designations according to [Veron-Cetty & Veron \(1996\)](#).

Table 2.2: The MUNICS Quasar Fields

Date	Telescope	Instrument	Remarks
1996 24.10–27.10	CA35	Ω'	Quasar Fields
1997 15.5–19.5	CA35	Ω'	Quasar Fields
1998 8.4–14.4	CA35	Ω'	
1998 12.5–17.5	CA35	Ω'	
1998 28.5–1.6	CA22	CAFOS	
1998 16.11–18.11	McD27	IGI	Quasar Fields
1998 16.12–20.12	CA22	CAFOS	
1998 23.12–30.12	CA35	Ω'	
1999 18.3	Wdst	MONICA	Calibrations
1999 27.5–3.6	CA35	Ω'	
1999 9.6–18.6	CA22	CAFOS	
2000 26.5–31.5	CA35	MOSCA	Spectroscopy
2000 27.5–28.5	HET	LRS	Spectroscopy
2000 16.7	CA35	Ω'	(1)
2000 20.11–22.11	VLT	FORS1/2	Spectroscopy
2000 24.11–28.11	CA35	MOSCA	Spectroscopy
2000 5.12	CA22	CAFOS	(1)
2000 17.12–18.12	CA22	CAFOS	(1)
2000 19.12	CA35	Ω'	(1)
2001 17.1–21.1	CA35	MOSCA	Spectroscopy
2001 11.2–13.2	CA35	Ω'	(1)
2001 26.3–1.4	CA35	MOSCA	Spectroscopy
2001 18.5–21.5	CA35	MOSCA	Spectroscopy
2001 15.12–20.12	CA35	MOSCA	Spectroscopy

(1) Re-imaging of fields with poor data quality.

Table 2.3: MUNICS observing runs. CA22 and CA35 are the 2.2-m telescope and the 3.5-m telescope of Calar Alto Observatory, respectively. McD27 is the 2.7-m telescope and HET is the Hobby-Eberly Telescope, both of McDonald Observatory, Austin, Texas. Wdst is the 0.8-m telescope of Wendelstein Observatory operated by the Universitäts-Sternwarte München.

For each frame a sky frame was constructed from typically 6 to 12 (temporally) adjacent frames where bright objects and detector defects have been masked out, and which were scaled to have the same median counts. These frames were then median-combined using clipping to suppress fainter sources and otherwise deviant pixels to produce a sky frame. The sky frame was scaled to the median counts of each image before subtraction to account for variations of sky brightness on short time-scales. The sky-subtracted images were flat-fielded using dome flats to remove pixel-to-pixel fluctuations in quantum efficiency. The frames were then registered to high accuracy using the brightest ~ 10 objects and finally co-added, again using clipping to suppress

highly deviant pixels due to cosmic ray events and defective pixels on the array, after being scaled to airmass zero and to a common photometric zero-point.

The 2×2 mosaic images were produced by registering the images using objects in the overlap regions, simultaneously cross checking the photometric calibration. Before combining, the images were adjusted to have the same background counts computed from the mode of the pixel values in ‘empty’ sky regions of the images to correct for residual differences in sky brightness. The absolute astrometric calibration of the images is discussed in Sect. 2.3.3 below.

2.3.2 Optical observations and data reduction

The optical imaging of the mosaic fields was performed at the Calar Alto 2.2-m telescope in the V , R , and I bands using the Calar Alto Faint Object Spectrograph (CAFOS) focal reducer in direct imaging mode. CAFOS was equipped with a SITE 2048² CCD detector, yielding a resolution of 0.53 arcsec per pixel and a circular field of view (due to vignetting by optics) of 16' in diameter. The V -band filter used was a standard Johnson filter, the R -band filter was an R_2 filter ($\lambda_0 = 0.648\mu$, $\Delta\lambda = 0.168\mu$), slightly narrower and bluer than Kron-Cousins R . The I -band filter was an RG780 filter with the red cutoff set by the CCD (see Fig. 2.5.) Total exposure times were 2700 s in V and I , and 1800 s in R , divided into several shorter exposures taken with offsets of $\sim 15''$, depending on the presence of bright stars and on seeing conditions to avoid too many saturated objects.

The quasar fields were imaged using the Imaging Grism Instrument (IGI) at the 2.7-m telescope of McDonald Observatory, using a 1024² TK4 CCD (7' field of view) and Mould R and I interference filters. Exposure times 1800 s in R and 2700 s in I , again divided into several shorter exposures.

The optical CCD data were reduced in a fairly standard manner using IRAF, except for cosmic ray cleaning. The frames were bias/overscan corrected and then flat-fielded using a combination of dome flats and sky flats. The I -band frames showed considerable fringing. Fringe images were created from the affected series of science exposures and occasionally also from twilight flats by medianing de-registered images after masking bright sources by hand as necessary. In some cases it was necessary to subtract a low order fit to the overall background in the science frames prior to construction of the fringe image to account for changes in the illumination pattern present in the images in the case where a bright star was close to the image border. The fringe images were then appropriately scaled and subtracted from the affected frames.

Cosmic ray events were identified by searching for narrow local maxima in the image and fitting a bivariate rotated Gaussian to each maximum. A locally deviant pixel is then replaced by the mean value of the surrounding pixels if the Gaussian obeys appropriate flux ratio and sharpness criteria (Gössl et al., 2000). Such a procedure is much more expensive in terms of computing time (roughly 10 CPU minutes per frame) compared to standard median filtering techniques, but is much more reliable in finding cosmic ray events in the wings of objects and in cleaning long cosmic ray trails.

The re-imaging system of CAFOS causes substantial radial distortion of the image which had to be dealt with before co-adding the offset images. Therefore the frames

were rectified using the known distortion equation, a polynomial of fourth order in the distance from the optical axis (K. Meisenheimer, private communication).

If necessary, variations in the background intensity across the frames caused by scattered light were fitted and subtracted in each individual frame. The images were then corrected for atmospheric extinction and scaled to a common photometric zero-point before finally being added using the positions of ~ 15 bright objects for the determination of the offsets between the individual frames.

During photometric nights, photometric standard stars were observed (Landolt, 1992; Christian et al., 1985) and programme fields with insecure calibrations were re-observed with short exposures. The run at the Wendelstein 0.8-m telescope was devoted to such a re-calibration to have independent calibrations for the fields. For each field, a photometric zero point and the atmospheric extinction were determined. No colour terms were fitted to the calibration data, as explained in Sect. 2.2.4. The typical formal uncertainties in the photometric calibration were ~ 0.08 mag in I , ~ 0.04 mag in R , and ~ 0.05 mag in V . The extinction coefficients were usually consistent with a Rayleigh atmosphere, with a few nights showing higher extinction, albeit within the variations typical for Calar Alto. As with the near-IR observations, consistency was checked against synthetic colours of stars, again finding no systematic offsets. We conclude that systematic errors in the optical photometric calibration are again smaller than 0.1 mag in all filters.

For further details of the optical data acquisition and reduction see Feulner (2000).

2.3.3 Astrometry

Astrometric solutions were computed for all K' -band images to translate pixel coordinates into celestial coordinates. For this purpose, astrometric standards from the USNO-SA1.0 catalogue (Monet et al., 1996) were selected in each frame. The celestial coordinates of these stars were matched against the pixel position using the IRAF task CCXYMATCH, and the plate solution was computed using CCMAP. The typical scatter is less than 0.4 arcsec rms.

The V , R , I , and J images of each field were registered against the K' -band image by matching the positions of ~ 200 bright homogeneously distributed objects in the frames and determining the coordinate transform from the K' -band system to each image in the other four pass-bands using the tasks XYXYMATCH and GEOMAP within IRAF. The scatter in the determined solutions is less than 0.1 pixels rms in the transformation from K' to J , and less than 0.2 pixels rms from K' to the optical frames. Note that the frames themselves are not transformed. We only determine accurate transformations and apply these later to the apertures in the photometry process.

2.3.4 Final photometric calibration

The final MUNICS source catalogues are calibrated on the 2-Micron All Sky Survey²(2MASS) in the K -band, which showed very good photometric agreement down

²2MASS Second Incremental Data Release,
<http://www.ipac.caltech.edu/2mass/releases/second/index.html>

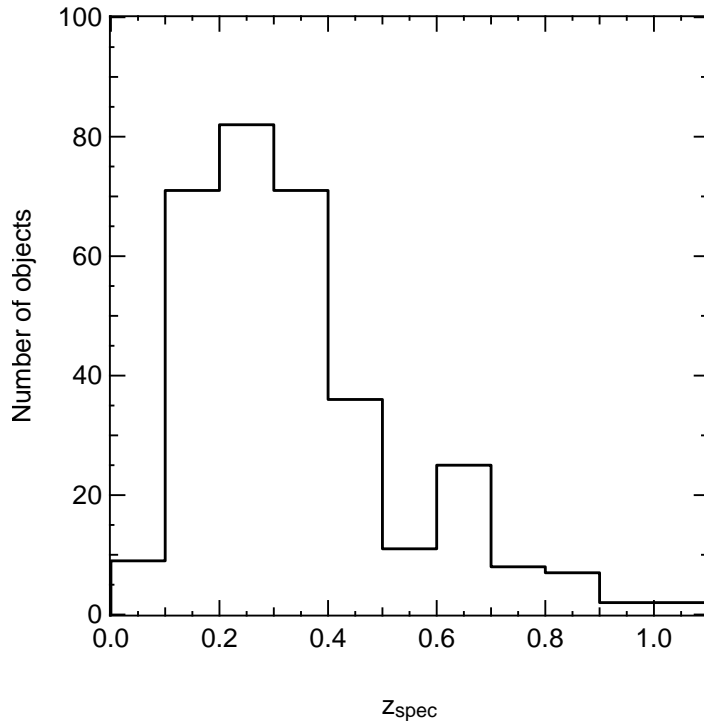


Figure 2.7: Histogram of spectroscopic redshifts. The total number of redshifts amounts to 324.

to $K \sim 17$, and a negligible colour term in $J-K$. To assure internal photometric consistency throughout MUNICS, all other pass bands, after passing their own calibration and subsequent quality control, were adjusted to the joint MUNICS/2MASS system by determining the offsets between stellar sequences from artificial photometry and actual field stars in the catalogues, keeping the calibrated K -magnitude fixed (see Sect. 2.2.4). These calibrations along with the offsets in the photometry we applied to the data in J, I, R , and V to match the stellar photometry are listed in Appendix A.

2.3.5 Spectroscopy

A spectroscopic follow-up programme is currently being conducted at the Calar-Alto 3.5-m telescope, the Hobby-Eberly Telescope, and the VLT, aiming ultimately at a magnitude-limited redshift survey of the K' -band selected catalogue. This spectroscopy programme is described in detail and analysed further in Feulner (2002).

To date redshifts for 324 objects have been obtained. Fig. 2.7 shows the redshift distribution for the current sample. Here we will use these data only to calibrate the photometric redshift code, introduced in Sect. 5.3.

Chapter 3

Yet another object detection algorithm: YODA

This chapter presents YODA (Yet Another Object Detection Algorithm), a software package for automated object extraction, photometry, and star-galaxy classification designed for the special needs of the MUNICS Survey. After introducing common object extraction packages (Sect. 3.1) we give an overview of YODA in Sect. 3.2 and discuss object detection (Sect. 3.3), photometry (Sect. 3.4), and the Bayesian star-galaxy classifier (Sect. 3.5).

3.1 Introduction

Large two-dimensional CCD detectors in the optical regime and also large array detectors in the near-IR have fostered the realisation of deep *wide-area* imaging surveys also covering *multiple bands* in wavelength. Such surveys have become a major tool especially in extragalactic research. Automated object extraction is essential for such projects, and considerable effort has been put into the development of such systems by many authors. Some earlier systems were developed specifically for photographic plate surveys, e.g., Kron (1980), FOCAS (Jarvis & Tyson, 1981), COSMOS (Beard et al., 1990), the APM package Maddox et al. (1990), while more recently developed packages aimed at CCD based surveys, e.g. PPP (Yee, 1991), and SExtractor (Bertin & Arnouts, 1996). Common to all these systems is their focus on single-band datasets, allowing for processing of multi-band datasets only under tough prerequisites, namely that the images share a common coordinate system and plate scale.

Today's large-area multi-band imaging surveys commonly suffer from various inhomogeneities in the dataset. Firstly, the use of different imaging instruments in different pass bands results in variations in the pixel scale and in the field distortion from one pass band to another. Secondly, variability in transparency, sky brightness, and seeing conditions will cause the signal-to-noise ratio to vary across the survey area. Thirdly, constructing mosaics out of smaller images will cause overlapping regions of the resulting frame to be deeper. And finally, illumination gradients will cause the background to vary even across single frames. For most scientific applications of such

surveys it is nevertheless necessary to measure accurate colours, e.g. for studies of the sources' stellar populations or the determination of photometric redshifts. This means photometry in equal (physical) size apertures in all wavebands has to be performed for each source in such an inhomogeneous dataset.

The software package presented here, YODA, is designed to handle inhomogeneous multi-band imaging data which do not share a common pixel coordinate system and have position dependent background noise in an automated way. Also, modularity in the sense of allowing for additional processing to be added easily at each step of the pipeline, most importantly during evaluation of the objects' properties, was considered to be desirable.

3.2 Overview of YODA

Object detection is usually performed using a single image which can be either a frame in one of the available pass bands (for selection reasons) or a weighted sum of frames in several of the available pass bands (for gaining signal to reach fainter detection limits). Subsequent photometry has then to be performed in the *same apertures* applied in all other images.

YODA input, therefore, consists of a "master frame" which is used for object detection as a first step. During this stage, the background value and the rms of the noise in the background are computed as a function of position on the master frame. Pixels lying above a certain threshold relative to the *local* background and noise are then assembled to form objects. The basic properties of these objects, like first and second moments and isophotal fluxes, are written to a catalogue file, the "master catalogue".

The master catalogue can then be processed further through the photometry and classification steps if desired, for the purpose of pre-selecting objects to enter the final catalogues, or it can be used directly for processing the multi-band data. The next step is to transform the positions of the objects in the master catalogue to all frames to be measured and to choose suitable apertures. The subsequent photometry and classification phases use the information in the master catalogue (describing the objects' shapes) and the transformed coordinates and apertures to analyse the objects in all images.

To allow the user to easily extend the package and adapt it to specific needs, for example by adding custom processing steps, all input and output of the various processing stages are handled via simple columnar-format text files. Furthermore, inclusion of user-supplied functions operating on the current object is possible at each step.

YODA is implemented in C++, and is developed under UNIX. It should be portable to essentially any hardware and software architecture where a reasonably ANSI-compliant C++ compiler is available, ideally GCC. It has been so far tested under Linux/x86, Linux/PowerPC, Solaris/SPARC, and Digital-UNIX/Alpha using GCC version 2.95.2 and 3.0.

3.3 Object detection

Two principle approaches to object detection have been proposed in the literature, searching for local maxima (Kron, 1980; Yee, 1991) and collecting consecutive pixels lying above a given threshold relative to the background noise, often called “thresholding”, (Jarvis & Tyson, 1981; Bertin & Arnouts, 1996). While searching for local maxima is better in the presence of crowding since close-by objects are naturally detected as distinct objects, it is less robust at low signal-to-noise and with low surface brightness objects. A promising new possibility might be to use vision models to analyse isophote contour shapes in the image, searching for closed contours. Such an approach has not yet been investigated with respect to its usefulness in astronomy because it is still prohibitively expensive in terms of computing time.

We have therefore implemented thresholding, after convolution of the image with a Gaussian of FWHM equal to the seeing in the frame. The optimum convolution kernel for the detection of faint sources would be the image PSF (Irwin, 1985), but for all practical purposes a Gaussian approximation is good enough, as comparisons have shown.

3.3.1 Background determination, thresholding, and object assembly

Thresholding effectively means collecting pixels above a certain surface brightness and signal-to-noise ratio limit. Usually this limit is expressed in terms of the variance of the background noise present in the image. Of course one would like the statistical significance of such a detection to be independent of position in the image. Therefore an accurate *local* estimate of the background value and noise is needed.

The background and the rms noise in the background are estimated as a function of position in the convolved image by inspecting the histogram of pixel values in rectangular regions of the image, usually 64×64 pixels in size. The pixels within each region are $\kappa - \sigma$ filtered to minimise impact of bright objects and outliers, and the histogram of their values is computed. The background and the rms value in each grid cell is estimated to be the mode and half of the width of the distribution at $1/e$ of the mode, respectively. The final background and rms values for each pixel are produced by bilinear interpolation between the grid cells. If necessary, background estimation can be improved by an iterative process of masking out pixels assigned to objects after thresholding and redetermining the background. This can be useful in the presence of bright stars, large galaxies, or moderate crowding.

Objects are detected by requiring that a minimum number N of consecutive pixels lie at least a certain thresholding factor t of the local rms above the local background. Consecutive here is defined as that at least one of the eight closest neighbours be above the threshold.

The values for N and t reflect a compromise between completeness at a given signal-to-noise – the magnitude limit – and the number of tolerable spurious detections per unit image area (Saha, 1995; Neuschaefer et al., 1995; Harris, 1990), depending on the form and size of the PSF and the pixel scale in addition to the characteristics of the noise present. They have to be chosen carefully for any individual application of

the data.

3.3.2 Splitting of multiple components

Close objects can overlap at the detection isophote, in which case they will be wrongly assembled into a single object by the thresholding phase. Therefore each object is re-examined by thresholding it at a number of linearly spaced, increasingly higher isophotes up to a fixed fraction of its maximum flux.

If an object decomposes into several components at some isophote, the component containing the pixel of maximum flux of the original object retains this identity, the other components being considered as new objects. The new objects are added to the end of the catalogue (their “detection isophote” set to the current splitting isophote) and the original object is continued to be examined. To avoid splitting noise peaks in the wings of objects, the subcomponents are required to consist of a minimum number of consecutive pixels to be regarded as real.

3.3.3 Evaluation of shape parameters

After de-blending, structural parameters within the detection isophote for each object are computed, namely the intensity-weighted radius,

$$R_e = \frac{\sum rI(r)}{\sum I(r)},$$

the intensity-weighted first and second moments,

$$\begin{aligned} C_x &= \frac{\sum xI(x,y)}{\sum I(x,y)}, & C_y &= \frac{\sum yI(x,y)}{\sum I(x,y)}, \\ I_{xx} &= \frac{\sum (x-C_x)^2 I(x,y)}{\sum I(x,y)}, & I_{yy} &= \frac{\sum (y-C_y)^2 I(x,y)}{\sum I(x,y)}, \\ I_{xy} &= \frac{\sum (x-C_x)(y-C_y)I(x,y)}{\sum I(x,y)}, \end{aligned}$$

the elongation,

$$E = \frac{\sqrt{(I_{yy} - I_{xx})^2 + (2I_{xy})^2}}{I_{xx} + I_{yy}},$$

and the full width at half maximum,

$$FWHM = 2\sqrt{\ln 2(I_{xx} + I_{yy})},$$

where $I(x,y)$ denotes the background subtracted intensity at pixel (x,y) , and $r^2 = (x - C_x)^2 + (y - C_y)^2$, the Euclidean distance from the object’s centre. The sums are to be taken over all pixels within the detection isophote.

For computing elliptical aperture shapes in the case where adaptive-size (“Kron-like”) apertures are to be used for photometry, the major and minor axes A and B , as well as the position angle θ , are computed based on the second moments:

$$\begin{aligned}
A^2 &= \frac{I_{xx} + I_{yy}}{2} + \sqrt{\left(\frac{I_{xx} - I_{yy}}{2}\right)^2 + I_{xy}^2}, \\
B^2 &= \frac{I_{xx} + I_{yy}}{2} - \sqrt{\left(\frac{I_{xx} - I_{yy}}{2}\right)^2 + I_{xy}^2}, \quad \text{and,} \\
\tan 2\theta &= 2\frac{I_{xy}}{I_{xx} - I_{yy}}.
\end{aligned}$$

The background flux, the flux at the detection isophote and the total flux within the detection isophote as well as the central and mean surface brightness are also computed. These quantities comprise the final output of the object detection and assembly phase.

3.4 Photometry

The photometry stage within the YODA package is capable of performing photometry in fixed size circular apertures and adaptive size elliptical apertures. Curves of growth in a series of concentric apertures can be computed for each object on demand, too.

The input for the photometry stage basically consists of pixel coordinate lists and aperture descriptions consisting of major axis, minor axis, and position angle. These can be taken from the output of the detection stage, with any geometric transformation applied to the coordinates (and apertures, if needed) to map between the detection frame and the frames to be measured.

The photometry algorithm sums up the sky subtracted flux in each aperture. The sky is determined locally for each object from pixels in an annulus of given distance from the object's aperture and width, having the same form as the aperture. Pixels belonging to neighbouring objects that intersect with the sky annulus are masked out during this process. The sky is measured by examining the histogram of sky pixel values, taking the mode as the final sky value and the width of the histogram as the error per sky pixel.

The error of the resulting object flux is estimated as

$$\Delta f = \sqrt{\frac{f}{G} + N_{pix}\sigma_{sky}^2 + \frac{N_{pix}^2\sigma_{sky}^2}{N_{sky}}}, \quad (3.1)$$

where f denotes the sky subtracted total flux within the aperture, G is the gain value in e^- per ADU, N_{pix} is the number of pixels in the aperture, N_{sky} is the number of pixels in the sky annulus, and σ_{sky} the error per sky pixel as derived from the histogram of sky values.

For the case where aperture photometry is applied to images with different pixel scales, the software offers the possibility to subsample the pixels within the aperture to account more accurately for signal in pixels touching the rim of the aperture.

Finally, Fig. 3.1 shows a comparison of magnitudes and errors measured in $5''$ circular apertures between YODA and SExtractor. The magnitudes agree well and the

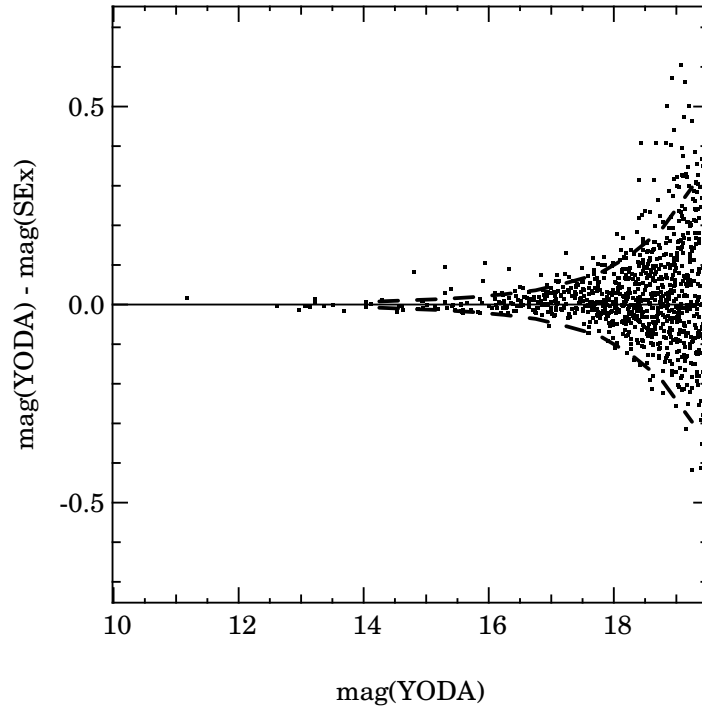


Figure 3.1: Comparison of photometry in 5 arcsec circular apertures between SExtractor and YODA. The dashed lines mark the maximum magnitude error as computed by YODA (see text) in bins of 0.5 magnitudes. This error estimate agrees well with the scatter in the magnitudes as measured by the two different packages. Outliers, mostly at the faint end, are due to differences in the treatment of blended objects. The data are taken from K -band images of high galactic latitude fields from the MUNICS survey obtained at the 3.5-m telescope at Calar Alto Observatory. Tests using simulated data yield similar results.

errors derived by YODA agree with the scatter in the magnitudes as measured by the two different photometry packages. The outliers present mostly at faint magnitudes are due to the different treatment of blended objects.

3.5 Star-galaxy separation

Three different principal approaches have been taken so far on the problem of classifying images of astronomical objects into distinct categories.

The first approach, a Bayesian one, uses the two-dimensional intensity distribution (including its noise characteristics) directly (Sebok, 1979; Valdes, 1982) to calculate the likelihood of a certain model given the observed counts. Here, the models can either be based on light distributions of observed galaxies (as in Sebok’s version), or simply on the observed PSF as a template for an unresolved source (as in Valdes’ implementation). This is particularly interesting if the discrimination between unresolved and resolved sources is a sufficient classification, as is generally the case for

star-galaxy separation.

The second approach, often called the parametric approach, analyses functions of the two-dimensional intensity distribution of the objects' images. Classification is then performed by defining hyper-surfaces in this parameter space bounding the regions occupied by distinct classes of objects, e.g. magnitude vs. peak intensity, the r_{-2} moment of Kron (1980), and the ψ parameter used in the APM survey (Maddox et al., 1990).

The third approach, also the most recently developed one, uses neural networks to classify objects (Odewahn et al., 1992; Bertin, 1994; Bertin & Arnouts, 1996; Bazell & Peng, 1998).

While all methods are successful and consistent at high signal-to-noise, classification gets very difficult as one gets closer to the limiting brightness of one's data. This is not only because of the decrease in signal-to-noise, but also because images of faint objects look more and more similar to images of unresolved sources as their area above the surface brightness limit decreases.

We have chosen to use the Bayesian approach for two reasons: firstly with the likelihood analysis it is possible to derive a meaningful *probability* that a given object's image is produced by a certain class, say unresolved point-like sources. Secondly, by calculating likelihoods for different model templates, one still gains information about the object's appearance, for example in terms of "compact source", "fuzzy star", or "stellar core" etc., even if a strict classification fails.

YODA's classification stage closely follows the *resolution classifier* presented in Valdes (1982) which is also used in the FOCAS package. The main difference lies in that Valdes uses a set of template images discretely sampling the parameter space of his models to find the template of maximum likelihood (for computing time reasons) while we use simplex maximisation to find the parameters of the most likely model, thus scanning parameter space continuously.

We briefly outline the algorithm and present some tests we have performed. For a detailed description of the algorithm's motivation and background we refer the reader to Valdes' thorough treatment in his original paper.

Mathematically stated, a Bayesian classifier picks a class C such that an object of the chosen class would be most likely to produce the observed image counts $I(x, y)$, thus maximising $P(C|I)$. Applying Bayes' theorem, we can state $P(C|I)$ in terms of $P(I|C)$, the probability of observing the counts $I(x, y)$ given an object of class C , which we can compute using the noise characteristics of the measurement and the expected intensity distribution of an object of class C .

The resolution classifier is based on the observation that all resolved sources will give better fits to resolved template than to a totally unresolved template (the PSF) and therefore the PSF and broadened versions of the PSF can be used as model classes C independent of any assumptions on the intrinsic profiles of galaxies present in the data. Models are generated solely from the measured PSF $\Phi(\mathbf{r})$ in the image, where \mathbf{r} denotes the position relative to the source's centre.

Two sets of models are used in our case, one consisting of narrowed and broadened versions of the pure PSF

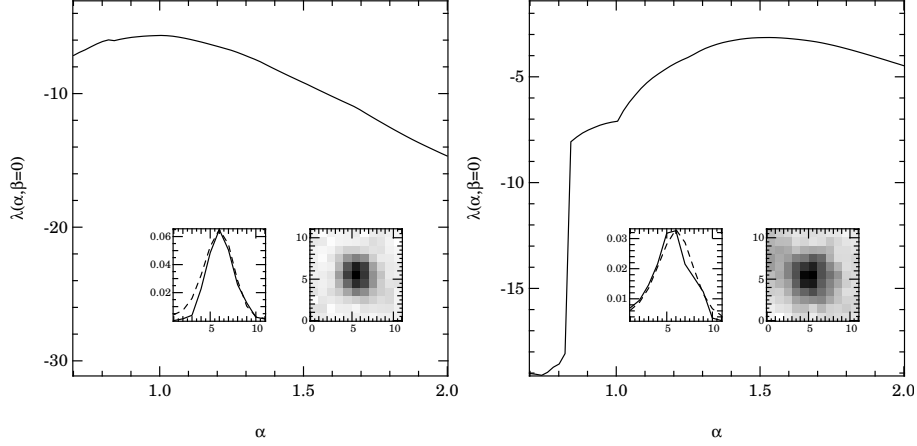


Figure 3.2: Cuts through the likelihood surface at $\beta = 0$ for a faint stellar source (left panel) and a faint clearly resolved source (right panel). The insets show the profile of the object (solid line) and the profile of the model of maximum likelihood (dashed line) in units of ADUs as a function of pixel position, as well as the image of the source.

$$T(\mathbf{r}) = \Phi\left(\frac{\mathbf{r}}{\alpha}\right), \quad (3.2)$$

with the scale parameter α ranging from 0.7 to 10. The second set consists of objects with a stellar core but some additional flux from a slightly broadened component

$$T(\mathbf{r}) = \beta\Phi\left(\frac{\mathbf{r}}{2}\right) + (1 - \beta)\Phi(\mathbf{r}). \quad (3.3)$$

with $0 < \beta < 1$. Thus $C = C(\alpha, \beta)$ for our classifier and we can write $P(I|C)$ as $P(I|\alpha, \beta)$ which is the quantity we have to maximise with respect to α and β . For unresolved, stellar images we expect the maximum to occur at $(\alpha = 1, \beta = 0)$.

Using the Poisson nature of the photon count noise in the image, the likelihood function $\lambda = \ln P(I|\alpha, \beta)$ becomes

$$\lambda = \sum_k \left[\frac{I_k}{LT_k + I_{sky}} \left(1 - \ln \frac{I_k}{LT_k + I_{sky}} \right) - 1 \right], \quad (3.4)$$

where the sum is to be taken over all image pixels, L is the models' luminosity, I_k and $T_k = T_k(\alpha, \beta)$ are the object's and the models' counts in the pixel k , respectively, and I_{sky} is the background intensity at the object's position. This function is maximised using a simplex algorithm with respect to the luminosity L and (α, β) .

Fig. 3.2 shows a cut through the likelihood surface at $\beta = 0$ for two faint objects, an unresolved stellar source and a clearly resolved source.

If a classification into distinct classes, e.g. stars, fuzzy stars, compact galaxies, galaxies, etc. is desirable, this is possible by defining a region in (α, β) -space for each class C_i . Then the probability that a source belongs to a specific class can be directly given as

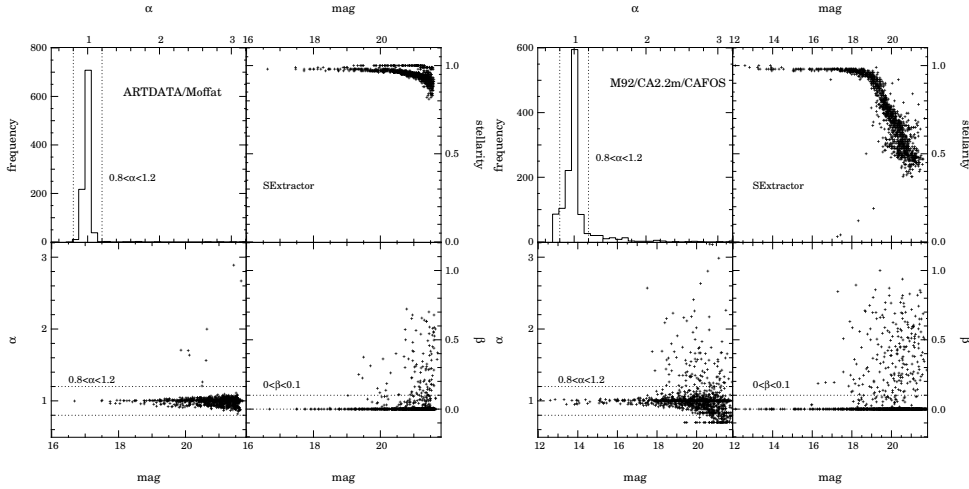


Figure 3.3: Results of applying the resolution classifier to artificial stellar images having Moffat-type profiles created with IRAF/ARTDATA (left panel), and to an R -band image of the globular cluster M92 (right panel) in (α, β) -parameter space in comparison with the *stellarity parameter* of SExtractor. The image of M92 was obtained at the Calar Alto 2.2-m telescope using the focal reducer CAFOS in imaging mode. The dotted lines mark the regions in (α, β) -space populated by unresolved (stellar) images. The top-left panel shows a histogram of the distribution of the scale parameter α , the bottom-left panel shows α vs. magnitude and the bottom-right panel shows β vs. magnitude. Finally, the top-right panel shows the output of SExtractor’s neural net based classifier.

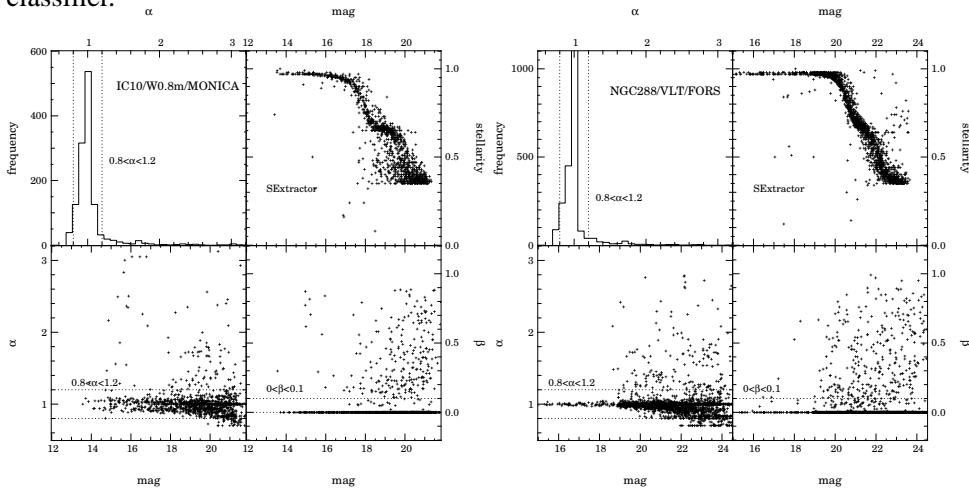


Figure 3.4: Results of applying the resolution classifier to an R -band image of the (resolved) dwarf galaxy IC10 (left panel) obtained at the 0.8-m telescope at Wendelstein Observatory and a V -band image of the globular cluster NGC288 (right panel) obtained with FORS at VLT UT1. Subpanels as in Fig. 3.3.

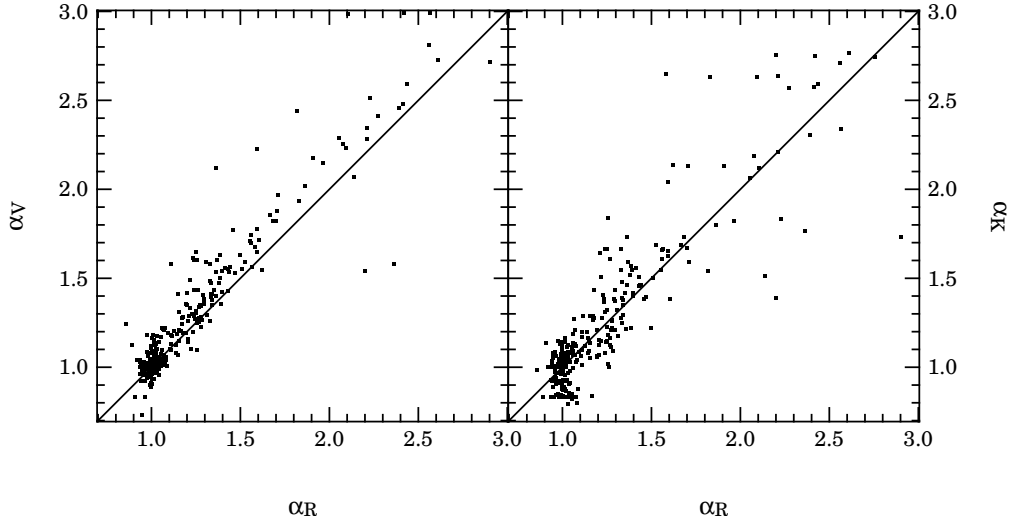


Figure 3.5: Comparison of the scale parameter α derived by the resolution classifier between measurements in different wavebands. The **left panel** shows V vs. R , the **right panel** K' vs. R . Plotted are objects with photometric errors smaller than 0.1 mag taken from the MUNICS survey. The V and R -band data were obtained at the 2.2-m telescope, the K' -band data were obtained at the 3.5-m telescope at Calar Alto Observatory.

$$P(I|C_i) = \int_{\alpha, \beta \in C_i} P(I|\alpha, \beta) d\alpha d\beta. \quad (3.5)$$

Fig. 3.3 and Fig. 3.4 show the application of this classifier to artificial data as well as real images taken at various ground based telescopes. Also shown are results of applying SExtractor’s neural network based classifier to the same datasets. For clarity, we have chosen to use data containing practically only stars, therefore we use images of the outskirts of the globular clusters M92 and NGC288, as well as an image of the surroundings of the Local Group dwarf galaxy IC10. These images have been taken at different telescopes – the Wendelstein 0.8-m, the Calar Alto 2.2-m, and the ESO VLT – to cover a realistic range in imaging characteristics of current instruments. The artificial data were created using the IRAF package ARTDATA with Moffat-type profiles.

These data can be used to define the region in (α, β) -space occupied by stars, and to check the robustness of the classification under different imaging conditions. Clearly, the region in parameter space can be restricted to $0.8 \leq \alpha \leq 1.2, \beta = 0$ for stars, in accordance to Valdes’ finding, over all the range of conditions covered by these datasets. The objects that scatter away from the stellar sequence are due to crowding, especially those objects which have a high value of β . This effect can be seen in the image of the dwarf galaxy IC10 even for very bright sources, as may be expected because of the presence of background flux from the galaxy causing the objects to have extra flux in the wings. Bright objects that scatter away in α usually

are blended with a close-by object.

The comparison with SExtractor's classification shows that the resolution classifier gives more robust results, especially at fainter magnitudes than the application of SExtractor's neural network *without special training*.

Finally, Fig. 3.5 compares the scale parameter α obtained for objects in deep images in the V , R , and K bands, showing that the classifier yields consistent results for the same objects imaged in different wavebands with different instruments.

Chapter 4

Image analysis

The construction of photometric catalogues from the reduced images is the topic of this chapter. The individual steps in this process will be described in some detail. These include the detection of objects in the K' -band images (Sect. 4.1), a thorough analysis of the survey's completeness (Sect. 4.5) with respect to point-like sources, disk galaxies and de Vaucouleurs profiles, the photometry of objects in all filters (Sect. 4.2), and the separation of stars and galaxies in the catalogue (Sect. 4.3). The chapter will be concluded by a comparison of number counts for galaxies with previous studies (Sect. 4.6) as a further consistency check on our data set, and a first look at colour–colour and colour–magnitude diagrammes (Sect. 4.7).

4.1 Object detection

Object detection was performed using the YODA source extraction software described in Chapter 3. This package was specifically designed to be used in multi-band imaging surveys, where the background noise is often inhomogeneous across the images – in mosaiced frames or in dithered images where the exposure time is a function of position – and where the frames do not share a common coordinate system and pixel scale, due to the use of multiple telescopes and imagers. The second point was considered a serious problem since re-sampling the images to a common coordinate system introduces quite considerable noise for faint sources.

Sources are detected by requiring a minimum number N_{pix} of consecutive pixels to lie above a certain threshold t expressed in units of the local rms σ of the background noise. To foster detection of faint sources, the images are convolved with a Gaussian of FWHM equal to the seeing in the image. The choice of the number of consecutive pixels N_{pix} and the threshold t is somewhat a tradeoff between limiting magnitude at some completeness fraction, say 50%, and the number of tolerable spurious detections per unit image area (Saha, 1995). Note that, since we aim at purely K' -band selected catalogues for most of our applications, the presence or absence of a source in other wave-bands cannot be used for confirmation or rejection of sources, so the expected number of spurious detections per unit image area is of great interest to us.

To find reasonable values for N_{pix} and t we performed simulations on the K' -band

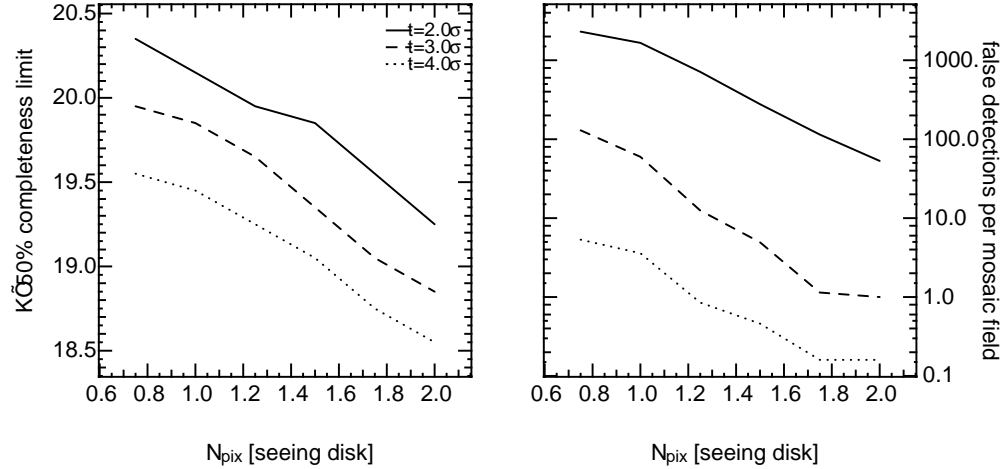


Figure 4.1: The behaviour of the 50 per cent completeness limit for point-like sources and the number of spurious source detections as a function of the detection threshold t in units of the local background rms σ and the required number N_{pix} of consecutive pixels above the threshold in units of the seeing disk area $\pi(FWHM/2)^2$. The left panel shows the change in limiting magnitude at 50 per cent completeness as a function of N_{pix} for detection thresholds of 2.0σ (solid line), 3.0σ (dashed line), and 4.0σ (dotted line). The right panel shows the number of spurious sources integrated over all magnitudes per image (one mosaic field), again as a function of N_{pix} and the detection threshold t . Line styles as in the left panel.

image of one of our mosaic fields (S6 f5–f8). The dependence of the 50 per cent completeness limit on N_{pix} and t was determined by adding point sources to the K' -band image and recording the fraction of the objects recovered by the detection software as a function of N_{pix} and t . The number of false detections was determined by looking for positive detections in an inverted (multiplied by -1) version of the image, after convincing ourselves that the background noise was sufficiently well approximated by a Gaussian. Fig. 4.1 shows the results of these tests.

At the depth of our data we detect roughly 1000 objects per mosaic field. Accepting 1 per cent contamination by false detections, i.e. roughly 10 false objects per mosaic field we fixed the detection threshold at $t = 3\sigma$ and the minimum number of consecutive pixels at 1.4 times the seeing disk area, $N_{pix} = 1.4\pi(FWHM/2)^2$, (10 pixels at 1 arcsec, 16 pixels at 1.5 arcsec seeing for the near-IR frames) and performed object detection using these parameters on all K' -band images.

4.2 Photometry

Photometry was performed in elliptical apertures the shape of which were determined from the first and second moments of the light distribution in the K' -band image, as described in Sect. 3.3.3, and additionally in fixed size circular apertures of 5 and 7

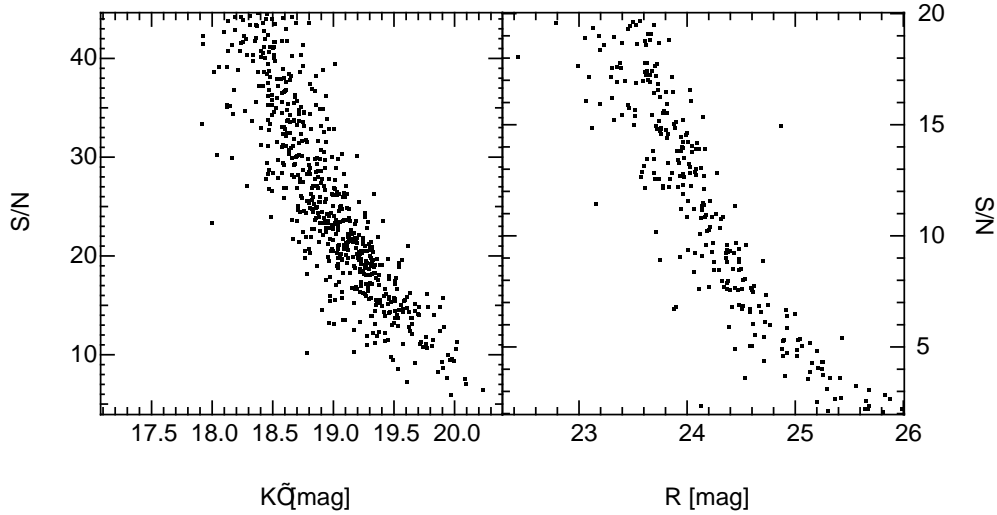


Figure 4.2: Signal-to-noise ratio in K' (left panel) and R (right panel) as a function of magnitude in circular apertures of 5 arcsec diameter for objects taken from the K' -selected catalogue of the field S6 f5–f8. The signal-to-noise ratio is defined here as the signal-to-noise ratio of the aperture photometry, i.e. total (sky-subtracted) flux within the aperture divided by the total noise within the aperture, with contributions to the latter coming from Poisson fluctuations in the object as well as the background, and the error in the determination of the background.

arcsec diameter. To ensure measurement at equal physical scales in every pass-band, the individual frames were convolved to the same seeing FWHM, namely that of the image with the worst seeing in each field. The signal-to-noise ratio as a function of magnitude for the 5 arcsec apertures is shown in Fig. 4.2. At the 50 per cent completeness limit in the K' band (19.59), the signal-to-noise ratio is ~ 10 . For such an object having an $R-K'$ colour of 6, the signal-to-noise ratio in the R band is roughly 3.

Aperture fluxes and magnitudes were computed for each object present in the K' -band catalogue irrespective of a detection in any other band. For this purpose the centroid coordinates of the sources detected in the K' -band images were transformed to the other frames using the full astrometric transformations as determined in Sect. 2.3.3. The shape of the apertures were transformed using only the linear terms of the transformation.

The photometric accuracy for the 5 arcsec aperture magnitudes is roughly 0.1 mag at $K' = 19$ mag. This error estimate includes the effects of photon noise and uncertainty in background determination and subtraction, but does not include (systematic) errors due to the photometric calibration. Fig. 4.3 shows plots of the magnitude error vs. object magnitude for one mosaic field in all five pass-bands.

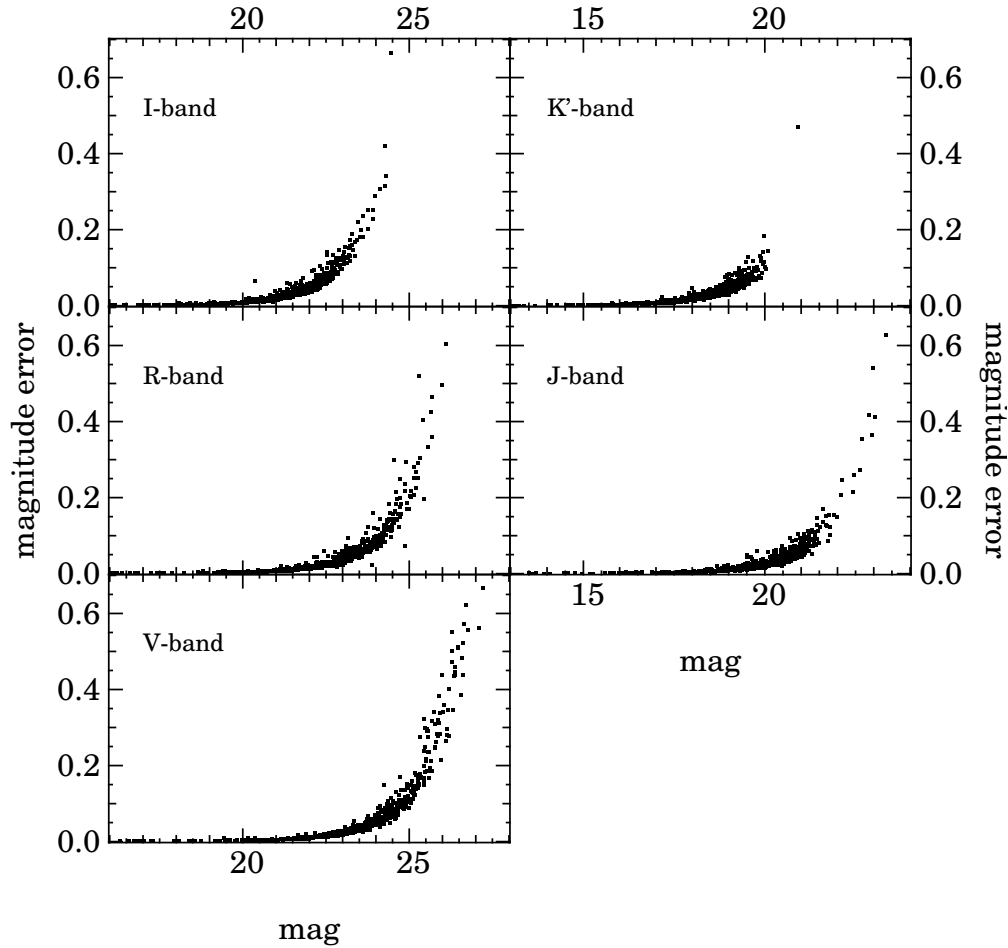


Figure 4.3: Magnitude errors as a function of magnitude in the mosaic field S6 f5–f8 in K' , J , I , R , and V as measured in circular apertures of 5 arcsec diameter for K' -band selected objects. Aperture fluxes are measured in every pass-band for each object present in the K' -band catalogue irrespective of a detection in any other band.

4.3 Star-galaxy separation

Star–galaxy separation relies on YODA’s image classification stage which is based on a Bayesian analysis of the probability that an object’s light distribution is due to an unresolved (point-like) source by comparison with light distributions constructed from the image’s PSF. YODA’s classification parameters are calculated for all objects in the catalogue in all available pass-bands.

As demonstrated in Sect. 3.5, classification is reliable across wave-bands and imaging instruments, and stellar sources almost do not scatter out of the stellar locus in parameter space (except in the presence of crowding). Rather, images of faint galaxies as they become smaller at larger distances, move onto the locus of point-like sources.

Using the multi-pass-band information available in MUNICS allows us to push the limit of reliable classification by using for each object the classification information in

those pass-bands where the signal-to-noise ratio is highest. Therefore, in the mosaic fields where 5 colours are available, we classify as stellar every source that is classified as stellar by YODA in the three pass-bands with highest signal-to-noise. In the quasar fields, where less colour information is available, we rely on the two images with highest signal-to-noise.

As can be seen in Fig. 4.15, objects classified as stars occupy the clearly defined stellar sequence in the $R-J$ vs. $J-K'$ colour-colour plane, with only very few objects classified as stellar having a $J-K'$ colour redder than ~ 1 . These are either misclassified faint and compact galaxies or very late-type stars or brown dwarfs, the latter is a possibility for those objects having also red $R-J$ colour. The objects lying on the stellar sequence at $R-J \gtrsim 2$ and which are classified as galaxies were found to be faint and barely resolved objects failing the classification as a star only due to their appearance in one filter. In many cases an obvious reason – like a second close object – could be identified. We conclude that most of these objects are, in fact, misclassified stars. The total fraction of point-like sources in the catalogues is ~ 10 per cent.

We have also checked the results of the image-based classification against spectral classification for those objects where spectroscopy was already available, namely 45 galaxies and 53 stars having $R < 20.5$. All these objects were correctly classified.

4.4 Galactic extinction

We use the Galactic reddening maps provided by Schlegel et al. (1998) using a value of $R_V = 3.1$ to calculate $A_\lambda = R_\lambda E(B - V)$ to correct the measured magnitudes for Galactic foreground extinction. The values of $E(B - V)$ for our fields are given in Table 2.1 and Table 2.2.

4.5 Completeness

The luminosity function, the mass function, and to a lesser degree the number counts of galaxies, provide an important observational tool set for understanding the evolution of galaxies. All these methods, being statistical in nature, rely on the comprehension of sample selection effects, i.e. the knowledge of what fraction of the true number of galaxies as a function of their intrinsic properties are actually present in the sample. The common method to gain access to such information is to add artificial objects to one's images – usually point-sources and/or galactic profiles with a fixed set of (apparent) radii – and compute the fraction of objects recovered by the detection algorithm used for the survey, as a function of, e.g, apparent magnitude.

The application of such a procedure for point sources is straight-forward and the result is easy to interpret. For deep extra-galactic surveys, the situation is severely more complicated as the galaxies in the survey span a wide range in intrinsic profile shape, intrinsic brightness, and intrinsic size. Additionally, the apparent quantities vary with cosmological distance, such that the fraction of galaxies visible is also a function of redshift. Therefore it is important to simulate objects obeying the known

scaling relationships for galaxies to get physically meaningful results, instead of just using some distribution in apparent quantities.

Dalcanton (1998) analysed the biases of the luminosity function introduced by the cosmological effects of size variation with redshift, and cosmological dimming for galactic profiles in dependence of size and magnitude, taking into account effects of seeing. Starting from the deficiency that magnitudes are usually measured as some sort of isophotal magnitude, that is directly influenced by the above mentioned effects, she finds the possibility of a severe underestimation of the true luminosity function introduced by the fact, that an object and distance depended part of the light is lost outside the limiting isophote.

Using profiles obeying the magnitude-radius relations, Yoshii (1993) predicted the number of objects lost in number count analysis. He finds a strong dependence of the detection rate on the applied detection criterions and magnitude measurement algorithm, leading to a larger number of undetected faint galaxies at high redshifts.

Here we present the results obtained from extensive completeness simulations on images of the MUNICS Survey in the K' band. In these simulations, based on the work presented in Snigula (2000), we analyse the detection probability and the lost-light fraction for point-like sources (Moffat profiles), elliptical galaxies (de Vaucouleurs profiles), and spiral galaxies (exponential profiles). The radii and magnitudes of the simulated galaxies were distributed following the projected fundamental plane relation (Burstein et al., 1997) for ellipticals and the Freeman law (Freeman, 1970) for spirals. The galaxies were simulated at five redshifts between $z = 0.5$ and $z = 1.5$, taking into account size variation with redshift as well as cosmological dimming and K-correction. A flat universe with $\Omega_M = 0.3$, $\Omega_\Lambda = 0.7$ and $H_0 = 65 \text{ km s}^{-1} \text{ Mpc}^{-1}$ was assumed.

In the present discussion, only the results for the MUNICS dataset in the K' band are presented, but as the selection biases described here are caused by the physical nature of the objects they are applicable in a much wider context of deep extragalactic surveys spanning the optical and near-infrared wavelength regimes. The conclusions drawn here are based on the use of a threshold-based detection algorithm. Accordingly they will hold true for other datasets as well, given that this assumption applies as well.

Finally, a reliable and handy analytic formula to estimate the completeness limit of a survey for point-like sources is presented.

4.5.1 Implementation of the simulations

Detection probabilities and photometry results were analysed for three different profile shapes: de Vaucouleurs profiles, exponential disks, and point-like sources.

For each profile type and each image, 200 artificially created objects were added to the image, taking into account the noise properties of the background and the photometric zero-point. The resulting image was processed in the same way as described in Sect. 4.1 regarding detection and photometry, using the software package YODA (Chapter 3). The resulting object catalogue was used to calculate the fraction of recovered objects and to compare the resulting photometry in Kron-like elliptical apertures to the quantities in the input catalogue.

This procedure was repeated 500 times resulting in a total of 100 000 artificial objects per type. In each run, the artificial objects were distributed randomly in (x,y)-position across the image, excluding a 25 pixel wide strip along the image borders, and requiring 20 pixel distance to existing objects, as we intentionally avoid crowding which would introduce effects beyond the scope of this work. Extended sources were convolved with a Gaussian with a FWHM of the measured seeing in the image. Poisson noise was added to all profiles.

In the following we discuss the generation of objects of each of the examined profile types in more detail.

Stars and point-sources

Point-like sources were simulated using a Moffat profile (Moffat, 1969) of the form

$$I(r) = \frac{I_c}{\left(1 + \left(\frac{r}{R}\right)^2\right)^\beta}. \quad (4.1)$$

with the characteristic intensity I_c . The size parameter R defining the radius of the created object was set to the measured value from point-like real sources in the analysed image, and the Moffat parameter β was fixed at the canonical value of 2.5. The apparent magnitudes assigned to the point-sources were chosen randomly from a constant probability density in the range $15 \leq m_{K'} \leq 25$.

4.5.2 Elliptical galaxies

Elliptical galaxies were simulated using a de Vaucouleurs profile (de Vaucouleurs, 1948). For a galaxy with effective radius r_e and effective intensity I_e (defined as the intensity at r_e), this profile can be written as

$$I(r) = I_e \exp\left(-7.67 \left(\frac{r}{r_e}\right)^{\frac{1}{4}}\right). \quad (4.2)$$

To create a realistic population of elliptical galaxies, the radii and absolute magnitudes of the galaxies were distributed to follow the Kormendy relation (Kormendy, 1985), a projection of the local fundamental plane relation (Burstein et al., 1997). We used the K -band Kormendy relation published by Pahre et al. (1995) for the effective radius of the galaxy R_e in kpc and the mean effective surface brightness $\langle\mu_e\rangle$ in mag arcsec⁻²

$$\log R_e = 0.332\langle\mu_e\rangle - 5.090. \quad (4.3)$$

Using the analytical form of the profile, Eq. (4.3) can be transformed into a relation between apparent magnitude m , effective radius r_e in arcsec and $\langle\mu_e\rangle$

$$m = -1.995 - 5 \log r_e + \langle\mu_e\rangle. \quad (4.4)$$

The effective radius R_e in kpc is translated into r_e for a galaxy at the distance D in kpc according to

$$R_e = r_e \cdot \frac{\pi}{648000} \cdot D. \quad (4.5)$$

The absolute and the apparent magnitude are linked by the distance modulus

$$m - M = 5 \log D + 10. \quad (4.6)$$

Using equations (4.5) and (4.6), Eq. (4.4) can be transformed into a relation between absolute magnitude M and effective radius R_e

$$M_{K'} = -1.99 \log R_e - 23.235. \quad (4.7)$$

The absolute magnitudes were chosen randomly and uniformly in the range $-26.5 \leq M_{K'} \leq -20.5$, corresponding to a range of ± 3 magnitudes around M_K^* for the local K-band luminosity function (Loveday, 2000).

To simulate a galaxy at redshift z , the apparent radius was calculated from the given physical radius using the angular distance, the absolute magnitude was transformed into the apparent magnitude using the luminosity distance. During each repetition of the simulation 40 galaxies for each of the five redshifts $z \in \{0.5, 0.75, 1.0, 1.25, 1.5\}$ were created. The axis ratios e were selected randomly in the range $0.7 \leq e \leq 1.0$, the position angles were chosen arbitrarily. For the galaxies at $z = 0.5$ the absolute magnitude range was shifted $-25.5 \leq M_{K'} \leq -19.5$ to better trace the faint-end drop-off of the completeness curve. The resulting apparent magnitudes were adjusted using only K-corrections derived from model SEDs (see Sect. 5.3.1), no evolution corrections were applied.

Spiral galaxies

Spiral galaxies were simulated as pure exponential profiles with no bulge component.

For a galaxy with half-light radius r_h and central intensity I_e the intensity profile can be written as

$$I(r) = I_0 \exp\left(-1.6783 \frac{r}{r_h}\right). \quad (4.8)$$

To create objects with realistic magnitude-size ratios, all galaxies fitted by a pure exponential profile from H-band surface photometry data of spiral galaxies published by Gavazzi et al. (2000) were used. The absolute H -band magnitudes were transformed into the K' -band using $H - K'$ colours derived from model SEDs (see Sect. 5.3.1). The mean correction was $H - K' \simeq 0.128$ mag. The resulting distribution of galaxies in the $\log R_h - M_{K'}$ plane was approximated by assuming

$$M_{K'} = -5 (\log R_h \pm 0.25) - 19.7. \quad (4.9)$$

For a population of local spiral galaxies, this distribution would correspond to a Freeman law with a constant K' -band central surface brightness of $17.52 \text{ mag arcsec}^{-2}$ and a scatter of $1.25 \text{ mag arcsec}^{-2}$.

Fig. 4.4 shows the absolute magnitudes and effective radii of the Gavazzi et al. data and of some artificially created objects. The distribution of the artificial objects reproduces that of the observed population reasonably well, extending to somewhat brighter magnitudes.

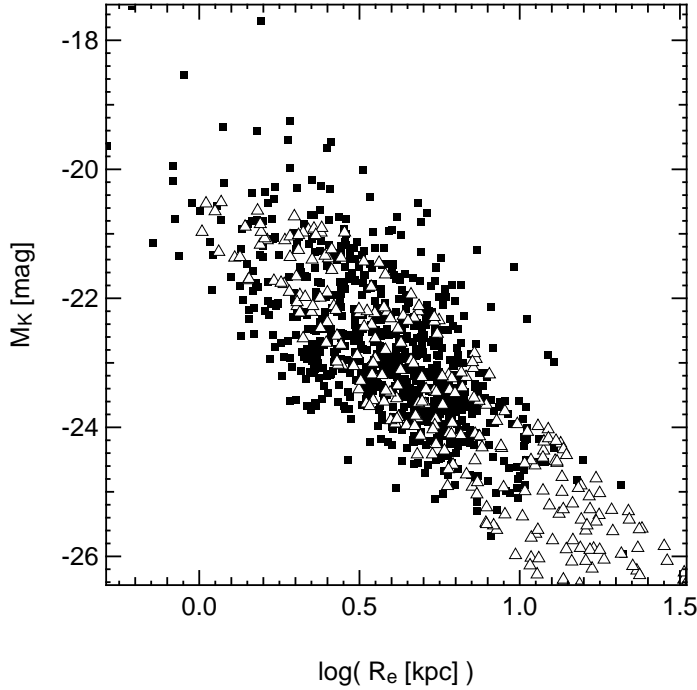


Figure 4.4: Absolute K' -band Magnitudes M'_K and effective radii for the galaxies fitted by a pure exponential profile published by Gavazzi et al. (2000) (filled squares) and some during the simulations created artificial objects (open triangles).

The absolute magnitudes of the objects were randomly chosen in the range $-26.5 \leq M_{K'} \leq -20.5$. Using the same techniques as for the elliptical galaxies the spirals were simulated for the same 5 redshifts, with axis ratios in the range $0 < e \leq 1$ and arbitrary position angles. The resulting apparent magnitudes were adjusted using only K-corrections derived from model SEDs provided by R. Bender (priv. comm.), no evolution corrections were applied. The mean surface brightnesses $\langle \mu \rangle$ were derived from a sample local spiral galaxies.

4.5.3 Results of the simulations

The results for one of the MUNICS fields with a seeing of approximately one arcsec FWHM are shown in Fig. 4.5. The upper panel shows the results for the point-sources, the middle and the lower panel for the de Vaucouleurs and exponential profiles, respectively, for the five redshifts simulated. An interesting effect seen in the figure is that, for higher redshifts $z \gtrsim 1$, the detection probability does not reach one even for the brightest objects, forming a plateau at some lower value. This effect is discussed in detail in Sect. 4.5.4 below. Fig. 4.5 shows that the completeness for point-like sources provides a conservative but reasonable approximation for the completeness of the extended objects up to a redshift of $z = 1.0$.

For each detected object, the difference between the input magnitude and the measured Kron-magnitude was computed. Fig. 4.6 shows the mean magnitude differences

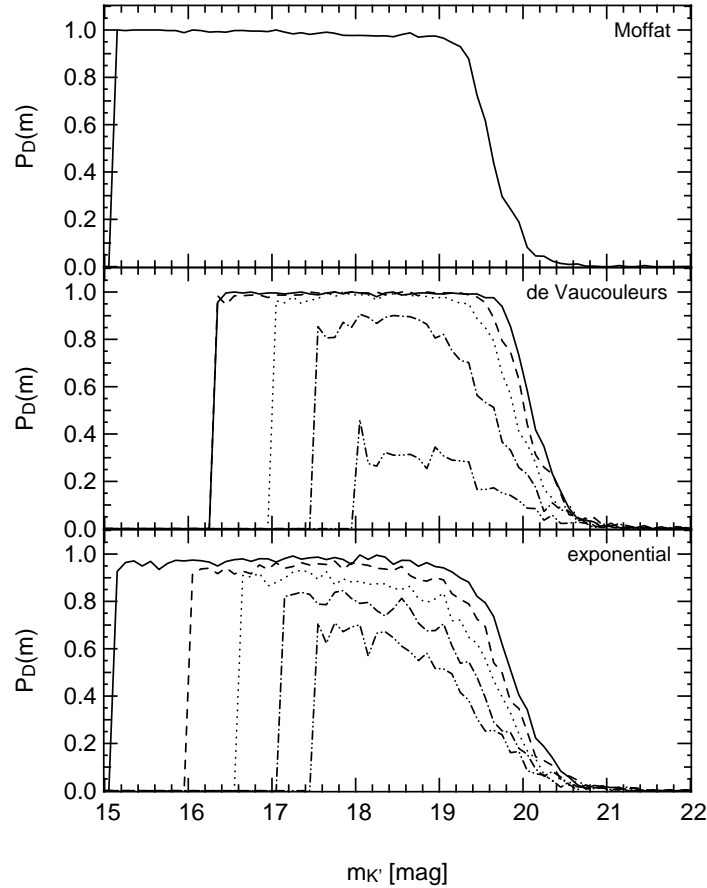


Figure 4.5: Probability $P_D(m)$ to re-detect an artificially created point-source (upper panel), an extended object with a de Vaucouleurs profile (middle panel) and exponential profile (lower panel) as a function of the objects K' -band input magnitude $m_{K'}$. The different line types in the middle and lower panel show the completenesses for the five analysed redshifts, $z = 0.5$ (solid), 0.75 (dash), 1.0 (dot), 1.25 (dashdot) and 1.5 (dashdotdot).

for the analysed profiles, averaged in bins of 0.25 mag and with the standard deviation of the measurements in the bin indicated as error bars.

4.5.4 Discussion

The object recovery probabilities for the high-redshift de Vaucouleurs profiles, and to a lesser degree the exponential profiles as well, as shown in Fig. 4.5 exhibit a significant detection bias compared to lower redshift objects. The fact that the objects at these redshifts never reach a detection probability of one is caused by the distribution of their physical parameters of the objects along the fundamental plane relation in the case of the ellipticals and by the constant central surface brightness in the Freeman law in the case of the disks. In both cases, as the objects' size increases, its radius

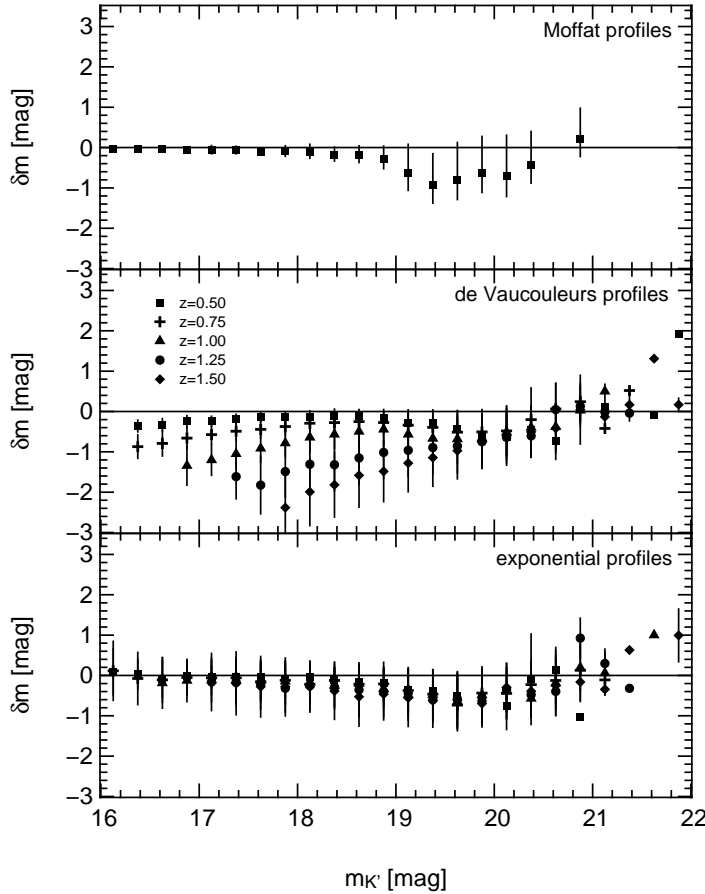


Figure 4.6: Mean magnitude difference $\delta m = m_{K'} - m_{meas}$ between the assigned magnitude $m_{K'}$ of the object and the Kron-magnitude measured by the photometry software m_{meas} in bins of 0.25 mag as a function of the input K' -band magnitude $m_{K'}$. The top panel shows the results for the point-sources, the middle panel for the de Vaucouleurs profiles and the lower panel for the exponential profiles. The error bars show the standard deviation of δm .

grows, and as a result the average surface brightness decreases. As a result, even the brightest objects of the distribution fail to produce an area large enough above the threshold in surface brightness to be detected with probability one in the presence of noise. In Sect. 4.5.5 these results are compared with the theoretical predictions of the visibility theory, which will confirm this view.

The deviations of the measured magnitude from the true magnitude for the de Vaucouleurs profiles as seen in Fig. 4.6, can be explained as resulting from the estimate of the Kron-like aperture radius under the conditions of a surface brightness limited detection procedure and the involved intrinsic brightness profile of the objects. Fig. 4.7 shows the intensity of the de Vaucouleurs and the exponential profile as a function of the radius in units of the effective radius, normalised to the same central surface density. The sharper decline with radius of de Vaucouleurs profile leads to a smaller

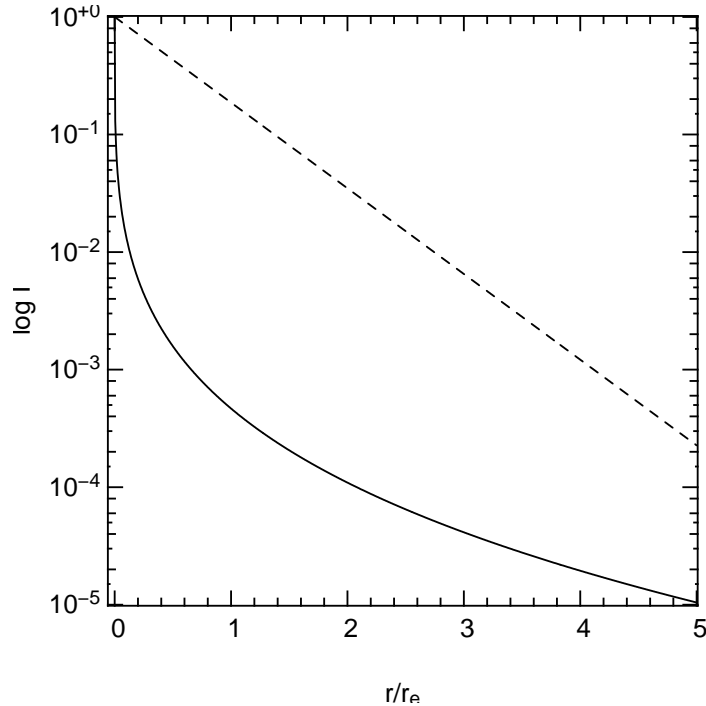


Figure 4.7: Intensity for a de Vaucouleurs profile (solid line) and an exponential profile (dashed line) normalised to the same central intensity. Plotted is the logarithm of the intensity against the radius relative to the effective radius. The de Vaucouleurs profile declines sharper in the centre than the exponential profile.

area above the detection threshold compared to an exponential of the same central surface brightness and effective radius and therefore to underestimating the true Kron-radius. Combined with the previously mentioned surface brightness distribution along the fundamental plane, this leads to an increased amount of lost flux and a larger error in the output magnitude for brighter objects, as these have lower surface brightnesses. In Sect. 4.5.6 we will confirm this explanation with predictions based on computations of the the visibility function and the lost-light fraction.

4.5.5 Visibility theory

Disney & Phillipps (1983) and Phillipps et al. (1990) analysed the dependence of the visibility of a galaxy on its surface brightness and apparent radius in a survey with given detection constraints in surface brightness and object radius. They calculate the maximum distance at which a galaxy with a given magnitude and effective radius can be seen, by calculating the distance at which the surface brightness at the limiting radius drops below the detection threshold. This theoretical approach can be used here as well to predict the behaviour of threshold-based detection algorithms.

To detect an object we require a minimum number of consecutive pixels to lie above a given brightness threshold, usually expressed in units of the standard devia-

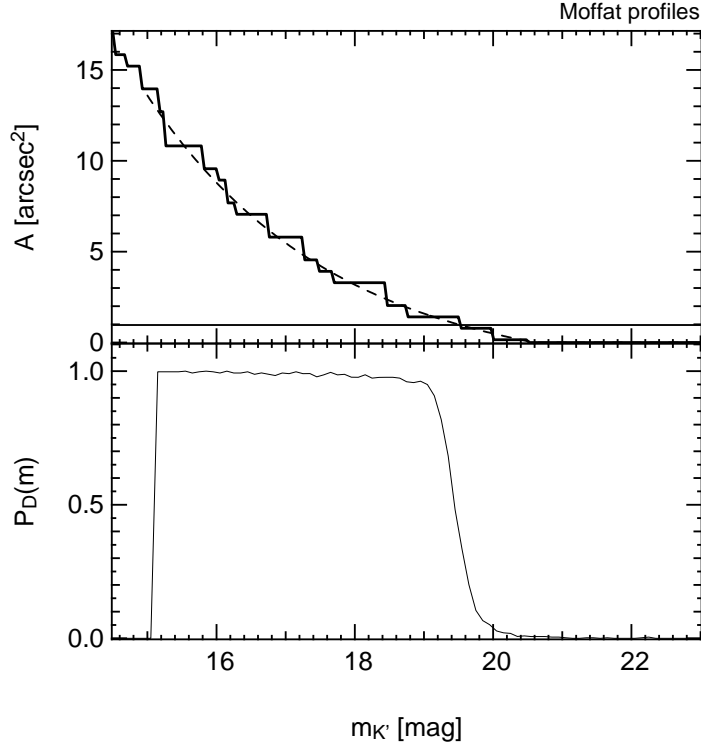


Figure 4.8: Area above detection threshold for point-sources with Moffat profiles. The upper panel shows the predictions derived from the visibility theory (Disney & Phillipps, 1983). The thick solid line shows the area above the detection threshold integrated over the image pixels in the presence of seeing. The smooth dashed line gives the area above the surface brightness limit as predicted by the inversion of the profile. The lower panel shows the object recovery probability as a function of assigned input magnitude.

tion of the background noise. The area required to be above the threshold is usually determined by the seeing disk (resolution element) size. Both values are adjusted such that faint real objects are detected at a tolerable rate of false detections.

In our case the minimum number of consecutive pixels, N , is chosen to be $N = \pi(1.4s/2)^2$, with s being the seeing FWHM in the image. The threshold t is set to 3 times the standard deviation σ of the local background noise.

In the case of circularly symmetric profiles, the calculation of the area above t is trivial, and the limiting surface brightness may be written as

$$\mu_{lim} = m_{zp} - 2.5 \log \frac{t}{p^2} \quad (4.10)$$

for the magnitude zero-point m_{zp} and the pixel scale $p = 0.396$ arcsec/pixel) in the MUNICS K -band images.

To create comparable completeness curves from the simulations as discussed above, a set of simulations for point-sources with Moffat profiles and circular face-

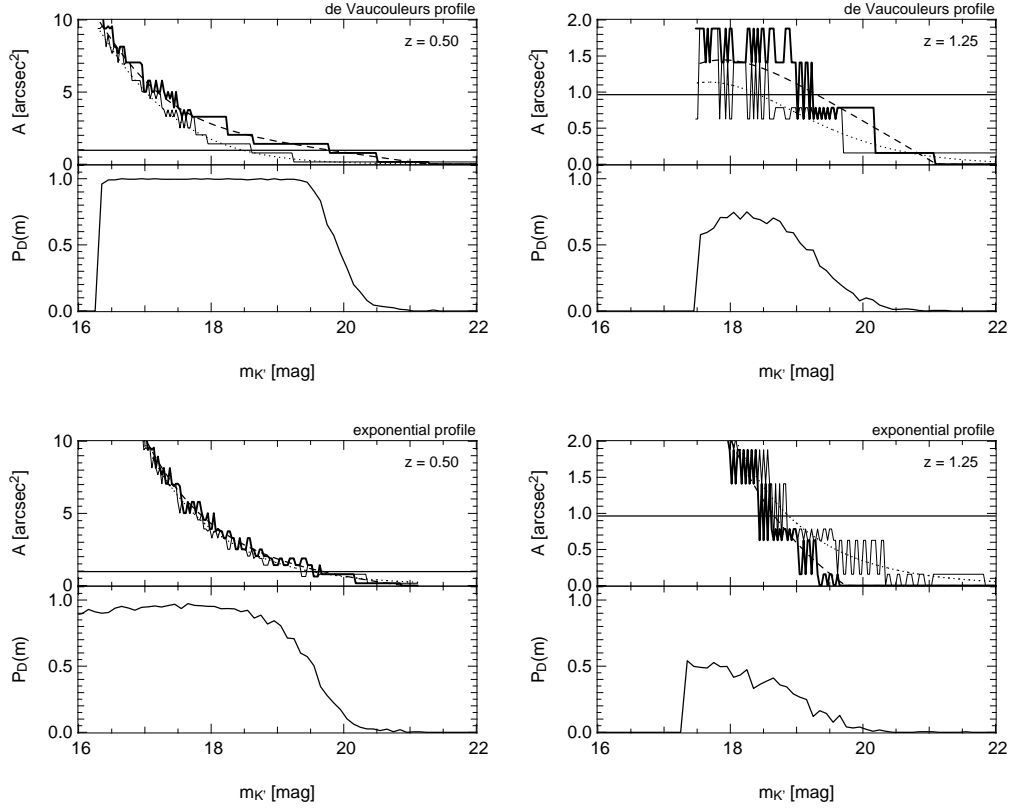


Figure 4.9: Predictions of the visibility function in comparison with the results of completeness simulations for de Vaucouleurs profiles (upper row) and exponential profiles (lower row) at redshift $z = 0.5$ (left column) and $z = 1.25$ (right column). The upper panels depict the area above detection threshold. The thin solid line shows the area above the detection threshold integrated over the image pixels in absence of seeing, the thick solid line the same but in presence of appropriate seeing. The smooth dotted curve gives the area above the surface brightness limit. The lower panels show the object recovery probability as a function of assigned input magnitude measured for a MUNICS image with seeing of ~ 1 arcsec.

on galaxies were calculated. These results are shown in Fig. 4.8 for point-sources, and in Fig. 4.9 for de Vaucouleurs profiles and exponential profiles at redshifts $z = 0.5$ and $z = 1.25$.

For Moffat profiles, the radius R of the circular area A above the limiting isophote can be calculated for Moffat profiles as

$$R = s \sqrt{10 \frac{\mu_{lim} - \mu_c}{2.5\beta} - 1} \quad (4.11)$$

with seeing s and characteristic surface brightness μ_c . In the upper panel in Fig. 4.8 the dashed line shows the area A resulting from the analytic calculation following Eq. (4.11), the solid line gives the area integrated over the image pixels.

Eq. 4.11 can be transformed into

$$m = \mu_{lim} - 2.5 \log \left(\frac{\pi s^2 \left(1 + \left(\frac{R}{s}\right)^2\right)^\beta}{\beta - 1} \right). \quad (4.12)$$

Using Eq. 4.10 this can be written as

$$m = m_{zp} - 2.5 \log \left(\frac{t \pi s^2 \left(1 + \left(\frac{R}{s}\right)^2\right)^\beta}{p^2 (\beta - 1)} \right). \quad (4.13)$$

These formulas provide a simple way to estimate the completeness limit for point-like sources for a given image, using easily measurable parameters. Tests using the MUNICS data have shown that this formula provides a robust estimate of the $\sim 50\%$ completeness level.

For de Vaucouleurs profiles with effective radius r_e and effective surface brightness μ_e within, R can be written as

$$R = r_e \left(\frac{\mu_{lim} - \mu_e}{8.3268} + 1 \right)^4 \quad (4.14)$$

and as

$$R = r_h \left(\frac{\mu_{lim} - \mu_0}{1.822} \right) \quad (4.15)$$

for exponential profiles with half-light radius r_h and the central surface brightness μ_0 .

The dotted line in the upper panels of figure 4.9 show the area within the limiting isophote as a function of apparent magnitude, as calculated using Eq. (4.14) and Eq. (4.15) for de Vaucouleurs profiles and exponential profiles, respectively. For comparison, the same values extracted from objects in the simulations are plotted, too. The area corresponding to the minimum area required for detection is indicated as a horizontal line. The intersection of this line with the curve then provides an estimate of the completeness limit.

The lower panels of these figures shows the detection probability as a function of apparent magnitude. Results are shown both with and without seeing. Seeing was modelled as a convolution with a Gaussian profile. In the case of the de Vaucouleurs profiles, moderate seeing ($\lesssim 1$ arcsec) improves detectability, since it distributes flux outwards, converting the steep core of the de Vaucouleurs profile to a larger and flatter flux distribution. This effect with disk profiles is much weaker since those are flatter, anyway. Note that broader seeing again worsens the detectability of objects, since at some value, it will distribute too much flux outwards and cause the core of the profile to drop beyond the threshold. For a full discussion, see Sect. 4.5.7.

From these plots it becomes apparent, that the theoretical predictions provide a good estimate of the completeness function (as the detectable area drops below the required value at the same apparent magnitude at which the completeness function drops off), but only provided that seeing is taken into account.

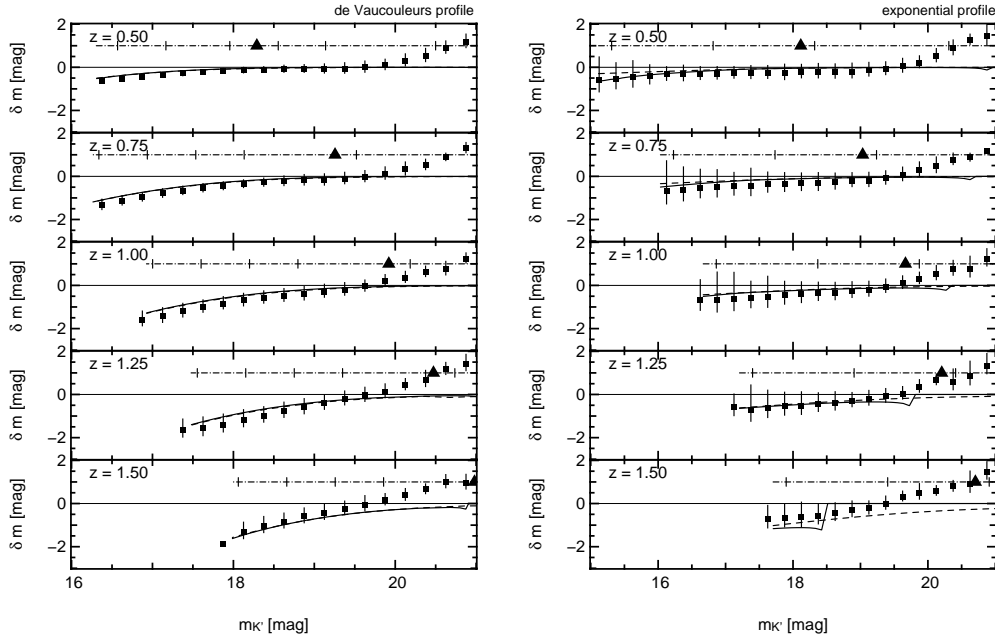


Figure 4.10: Deviation of the measured magnitude from the assigned input magnitude δm for de Vaucouleurs profiles (left figure) and exponential profiles (right figure) with a seeing of 0.8 arcsec, as a function of the assigned K' -band input magnitude. To provide a clue for the width of the distribution, the rms is shown as error bars. The solid line shows the theoretical prediction of the lost-light fraction in absence of seeing, the dashed line for profiles convolved with a Gaussian seeing. The horizontal scale at $\delta m = 1$ in each panel gives the effective radii of the simulated objects in kpc for $r_e \in \{10, 5, 2, 1, 0.5, 0.1\}$ for the de Vaucouleurs profiles at $z = 0.5$, $r_e \in \{40, 20, 10, 5, 1, 0.1\}$ for the other elliptical galaxies and $r_e \in \{20, 10, 5, 2, 1\}$ for the exponential profiles. The large filled triangle denotes the apparent magnitude and radius of an M^* galaxy.

In the case of the high-redshift ($z = 1.25$) galaxies, the detection probability never reaches one. This results from the fact that even for the brightest simulated objects – with an absolute magnitude 3 mag above M^* , but lower mean surface brightness – the objects' core lies barely above the detection threshold for all magnitudes. Therefore, noise easily scatters objects below the threshold and the detection probability is always smaller than unity.

Taking only the predictions of the visibility function for the exponential profiles at high redshifts, the low detection probability surprises. Although the detectable area is much larger than the limiting one, the completeness fraction remains low. The exponential profile is due to its rather flat light-distribution much more susceptible to distortions caused by noise than the steeper de Vaucouleurs profile. These scattered noise pixels, can then either reduce the objects' size below the limiting radius, or form additional false maxima leading to a mis-detection as several objects, not recognised as the artificially created one.

4.5.6 Lost-light fraction

The magnitude differences between the input and the measured magnitudes shown in figure 4.6 exhibit a strong deviation for elliptical galaxies at the bright end of the distribution. The results from the analysis of the visibility function can be used to calculate the lost-light fraction (LLF). Assuming that an object is detected out to the limiting radius r_{lim} where the surface brightness drops below the detection limit, the intensity weighted Kron radius r_k can be calculated for circularly symmetric objects as

$$r_k = \frac{\int_1^{r_{lim}} r' I(r') dr'}{\int_1^{r_{lim}} I(r') dr'}. \quad (4.16)$$

The galactic profile is then integrated out to some factor (in our case 2.5) times the Kron-radius, and the corresponding magnitude is calculated. Fig. 4.10 shows the results of this calculation of the lost-light fraction for circular symmetric de Vaucouleurs and exponential profiles in comparison with the results obtained from the completeness simulations.

The measured magnitudes of the elliptical galaxies deviate strongly from the assigned input magnitudes due to underestimation of the Kron-radius caused by the steep decline of the profile in the central detectable part. In case of the exponential profiles the differences in the photometry are much smaller, since the flatter profile causes the Kron-radius estimate to be closer to the true value, even if only the inner part of the profile is detected.

The analytically calculated lost-light fraction predicts a slightly lower difference than the measurements show (except for the highest-redshift bin). This can be explained by the fact, that the theoretical approach is based on the ideal case where the object is detected exactly out to the maximum visible radius, and that the form of the profile is not distorted. In reality, the area is pixelated and integration over the pixels in calculating the Kron-radius causes this number to be underestimated. Additionally, noise causes mismeasurement of the object size and shape.

In contrast, in the highest-redshift bin ($z = 1.5$), the analytically calculate lost-light fraction predicts higher deviations than actually measured in the simulated images. These objects are only detectable due to additional pixels being scattered above the threshold by noise (as can be seen in Fig. 4.12, which shows that the whole profile is below the threshold). This additional flux causes the photometry to yield too bright magnitudes.

The same effect causes the photometry to yield too bright magnitudes for objects at the faint end of the luminosity function in all redshift bins. These, too, are too faint to be detected without the presence of pixels scattered above the threshold by noise.

As mean surface brightness increases towards fainter objects, and as those are also intrinsically smaller, a larger fraction of the total profile is visible around M^* , and the measurement of the total magnitude improves.

It should be kept in mind, that the largest differences occur for the rather rare objects with absolute magnitudes 3 mag brighter than M^* , while the magnitudes of M^* objects are measured correctly. In the calculation of the luminosity function, this would cause the brightest objects to be redistributed to lower absolute magnitudes. But again,

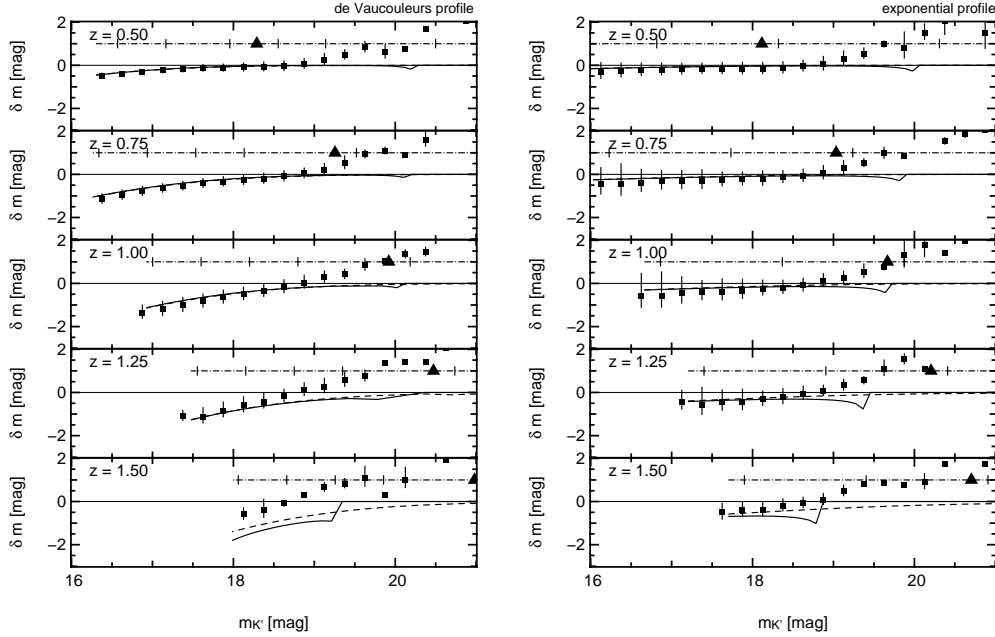


Figure 4.11: Deviation of the measured magnitude from the assigned input magnitude δm for de Vaucouleurs profiles (left figure) and exponential profiles (right figure) with a seeing of 1.6 arcsec. To provide a clue for the width of the distribution, the rms is shown as error bars. The solid line shows the theoretical prediction of the lost-light fraction in absence of seeing, the dashed line for profiles convolved with a Gaussian seeing. The horizontal scale at $\delta m = 1$ in each panel gives the effective radii of the simulated objects in kpc for $r_e \in \{10, 5, 2, 1, 0.5, 0.1\}$ for the de Vaucouleurs profiles at $z = 0.5$, $r_e \in \{40, 20, 10, 5, 1, 0.1\}$ for the other elliptical galaxies and $r_e \in \{20, 10, 5, 2, 1\}$ for the exponential profiles. The large filled triangle denotes the apparent magnitude and radius of an M^* galaxy.

the numbers of such bright galaxies are rather low ($\sim 10^{-4}$ times lower space density than M^* objects), and thus the contamination of the LF by these, rather small. At the faint end, the situation is similar. Although these objects are much more numerous, they are actually below the detection limit, and therefore only detected seldomly by chance (about 200 out of 20000 simulated objects at $z = 0.5$ were detected beyond 20 mag), such that the influence of their wrongly measured magnitude on statistics as the luminosity function is rather negligible.

4.5.7 The effect of seeing

To explore the influence of seeing on the visibility, seeing convolved galactic profiles were used to calculate the visibility function and the lost-light fraction. The seeing was simulated using a two-dimensional Gaussian of the form

$$I(\mathbf{r}) = \frac{1}{2\pi\sigma^2} \exp\left(-\frac{\mathbf{r}^2}{2\sigma^2}\right). \quad (4.17)$$

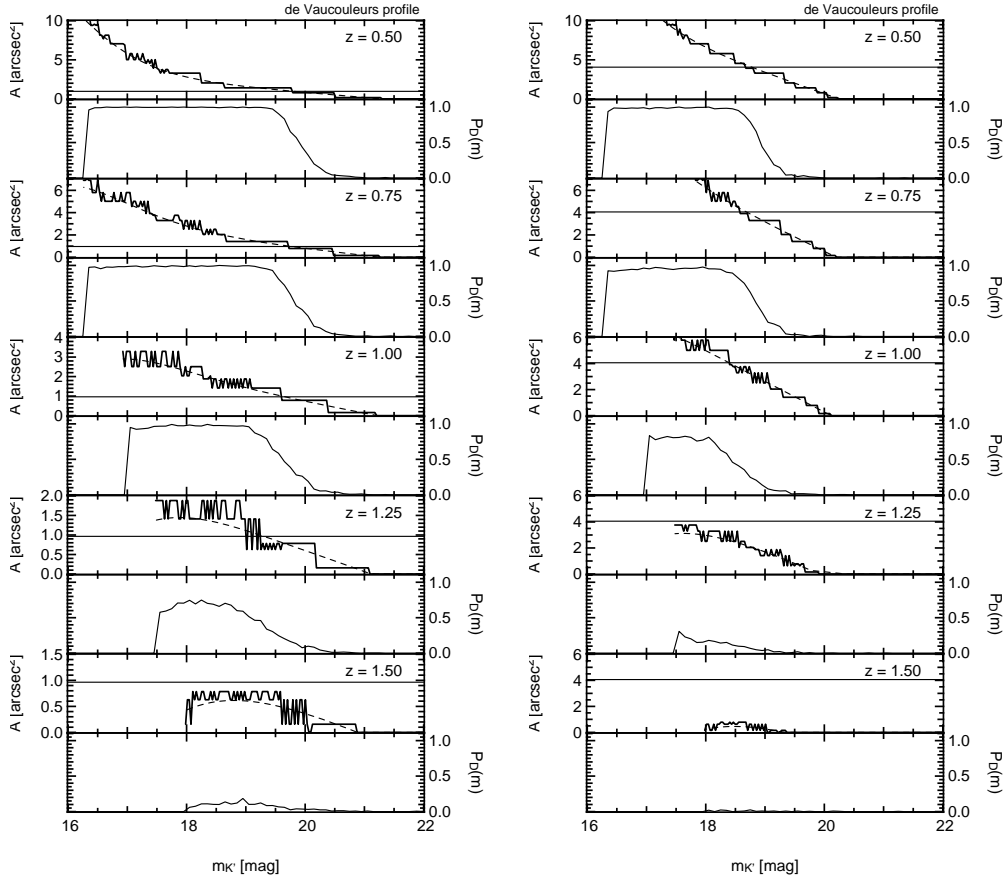


Figure 4.12: Visibility function and completeness function for circular symmetric de Vaucouleurs profiles convolved with a Gaussian seeing of 0.8 arcsec (left figure) and 1.6 arcsec (right figure) at redshifts $z \in \{0.5, 0.75, 1.0, 1.25, 1.5\}$. The upper panels show the theoretical predictions of the visibility function in the continuous case (dashed) and integrated over the image pixels (solid). The lower panels show the object recovery fraction as a function of input magnitude.

The width of the Gaussian kernel σ calculated from the width s of the measured seeing PSF as

$$\sigma = \frac{s}{\sqrt{8 \ln 2}}. \quad (4.18)$$

The galactic profiles I_g were convolved with the Gaussian resulting in the convolved profile I'_g

$$I'_g(r) = \int_0^\infty \int_0^{2\pi} r' I_g(r') e^{-\frac{r^2 + r'^2 - 2rr' \cos \varphi}{2\sigma^2}} d\varphi dr' \quad (4.19)$$

Using convolved profiles, the calculation of the visibility function and the lost-light fraction were repeated on images with two different seeing values of 0.8 and 1.6 arcsec.

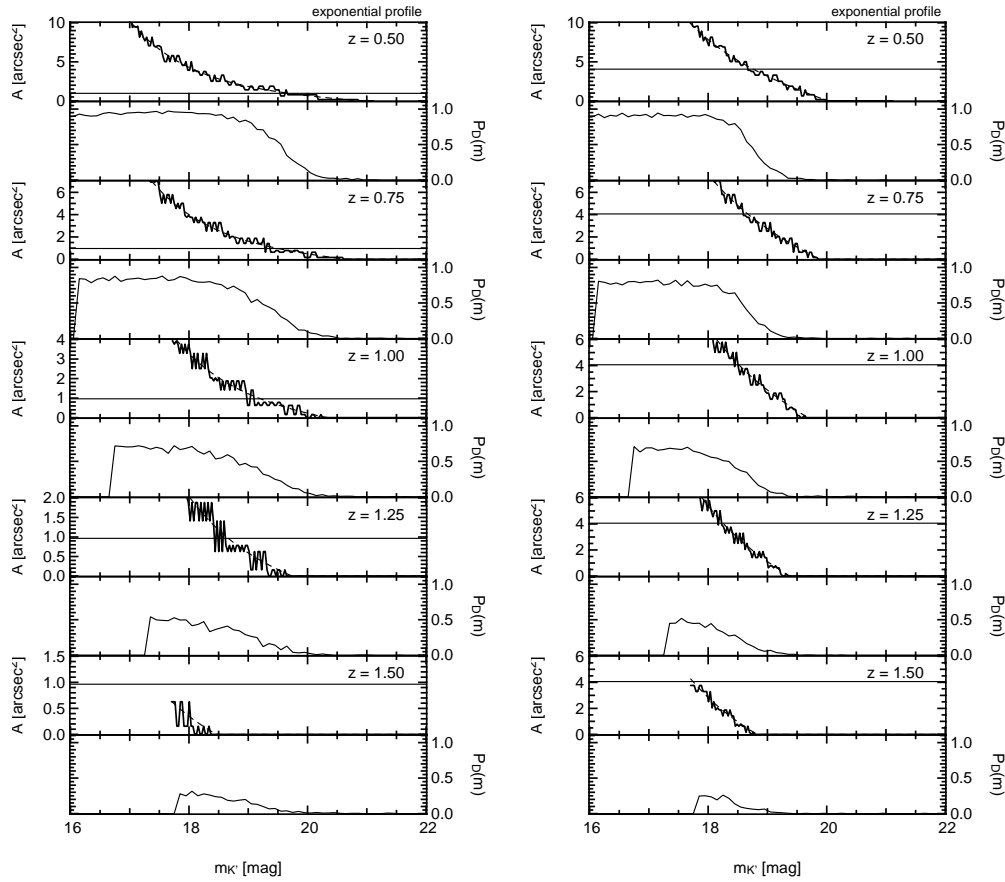


Figure 4.13: Visibility function and completeness function for circular symmetric exponential profiles convolved with a Gaussian seeing of 0.8 arcsec (left figure) and 1.6 arcsec (right figure) at redshifts $z \in \{0.5, 0.75, 1.0, 1.25, 1.5\}$. The upper panels show the theoretical predictions of the visibility function in the continuous case (dashed) and integrated over the image pixels (solid). The lower panels show the object recovery fraction as a function of input magnitude.

Fig. 4.12 shows the results of the completeness simulations and the calculation of the visibility function for de Vaucouleurs profiles with seeing of 0.8 and 1.6 arcsec, figure 4.13 the same for exponential profiles.

An increase of the seeing distributes more light outward from the central parts of the profile within the seeing disk, resulting in a smoothed light distribution in the centre. As discussed above, moderate seeing improves detectability of faint objects by distributing light from the bright centre more evenly across a larger area without reducing the light in the centre below the threshold.

As the seeing gets larger, this effect is counter balanced by the fact that now the amount of light redistributed away from the centre becomes so large that the central parts of the profile fall below the detection threshold.

In the case of the steep de Vaucouleurs profile, this effect is stronger compared to the exponential profile. The detection limit is fainter by roughly 1 magnitude in the

presence of seeing of 0.8 arcsec compared to the seeing-free case. On the other hand, once the seeing is as large as 1.6 arcsec, the detection limit has dropped close to the no seeing case. In the highest-redshift bins, detectability of elliptical galaxies is depressed below the no-seeing case, since now the seeing-convolved profile is completely below the detection threshold.

The lost-light fraction – shown in Figs. 4.10 and 4.11 – for objects with seeing, in contrast, shows no significant change with the increase of the seeing except close to the completeness limit and at high redshift.

The exponential profiles suffer from the same effects, resulting in decrease of the completeness limit with increased seeing. The low overall recovery fraction of exponential profiles compared to de Vaucouleurs profiles at high redshift is caused by the flatter light distribution and the lack of a central peak compared with the de Vaucouleurs profiles. Due to this, the objects' appearance is much more irregular in the images due to the significant fraction of flux in Poisson noise. This results, on the one hand, in pixels dropping below the detection limit, and, on the other hand, false maxima, resulting in the detection of two or more (distinct) structures. These effects have the strongest impact for the circular symmetric (face-on) objects used here. In the more realistic approach using randomly distributed ellipticities – as shown in figure 4.5 – the impact of these effects is much less significant, due to the steeper apparent profiles for inclined disks.

4.5.8 Detection probabilities for the MUNICS Fields

Finally, we present the results of the completeness simulations for the Mosaic fields of the MUNICS survey (see Table 2.1).

Plots of the completeness fraction as a function of apparent magnitude are shown in Appendix B. Additionally, we parameterise the shape of the completeness curves using a combination of two power-laws. A function of the form

$$P_D(m) = \frac{p_0}{\left(\frac{m}{m_0}\right)^\alpha + \left(\frac{m}{m_0}\right)^\beta} \quad (4.20)$$

was fitted to the results. The normalisation p_0 provides a rough estimate of the height of the plateau the completeness function reaches. The break magnitude m_0 can be used as an indication of the 50% completeness limit, if a higher maximum detection rate is reached.

Tables 4.1, 4.2, and 4.3 list the parameters for point-like sources, de Vaucouleurs, and exponential profiles, respectively.

Field	p_0	m_0	α	β
S2F1	0.98	18.82	0.11	127.16
S2F5	0.98	19.12	0.08	143.12
S3F1	0.65	18.78	0.11	127.90
S3F5	0.96	19.25	0.16	140.07
S4F1	0.99	19.08	0.01	101.10
S5F1	0.99	19.09	0.05	144.70
S5F5	0.99	19.11	148.81	0.04
S6F1	0.99	18.75	0.00	149.33
S6F5	0.97	19.25	142.99	0.12
S7F5	0.98	19.06	0.06	92.30

Table 4.1: Parameters of the fit of Eq. 4.20 against the results obtained from the completeness simulations for point-like sources. The normalisation p_0 provides a rough estimate of the height of the plateau the detection probability reaches. The break magnitude m_0 can be used as an approximation of the 50% completeness limit, if a higher maximum detection rate is reached.

Field	$z = 0.5$			$z = 0.75$			$z = 1.0$					
	p_0	m_0	β	p_0	m_0	α	β	p_0	m_0	α	β	
S2F1	1.02	19.22	-0.32	110.50	1.01	19.12	-0.31	102.47	0.99	18.93	76.05	-1.22
S2F5	1.01	19.54	118.58	-0.15	1.01	19.44	114.66	-0.20	1.02	19.29	-0.70	97.96
S3F1	0.83	19.16	111.82	-0.54	0.76	19.09	102.57	0.33	0.72	18.85	74.21	0.30
S3F5	1.01	19.65	139.21	-0.20	1.02	19.60	-0.28	111.96	1.01	19.45	106.26	-0.55
S4F1	1.00	19.53	-0.04	98.09	0.99	19.42	82.18	-0.09	0.86	19.30	0.38	77.23
S5F1	1.01	19.48	129.05	-0.18	1.02	19.40	110.91	-0.38	1.01	19.24	94.38	-0.72
S5F5	1.01	19.52	-0.16	128.85	1.02	19.44	-0.40	107.08	1.02	19.29	-0.83	90.94
S6F1	1.01	19.14	127.56	-0.13	1.00	19.03	126.05	-0.34	0.96	18.77	74.39	-0.99
S6F5	1.01	19.67	-0.11	127.00	1.01	19.61	121.12	-0.21	1.01	19.50	-0.44	107.66
S7F5	1.00	19.48	-0.08	87.53	1.00	19.40	74.91	-0.22	0.91	19.31	0.02	71.80

Field	$z = 1.25$			$z = 1.5$				
	p_0	m_0	β	p_0	m_0	β		
S2F1	0.34	18.93	5.92	85.92	0.06	19.02	-6.91	56.93
S2F5	0.80	18.98	70.49	-2.44	0.14	19.18	64.29	-1.45
S3F1	0.32	18.63	37.62	3.52	0.08	18.07	17.02	-770.30
S3F5	0.95	19.14	70.63	-2.49	0.27	19.12	59.58	-4.79
S4F1	0.59	18.98	-3.16	52.67	0.12	18.91	41.61	-9.17
S5F1	0.80	18.92	-2.44	65.87	0.26	18.21	33.96	-41.32
S5F5	0.86	18.95	-3.57	60.75	0.05	19.59	113.45	13.68
S6F1	0.19	18.83	8.28	65.91	-	-	-	-
S6F5	0.96	19.22	68.88	-1.27	0.36	18.99	50.96	-1.59
S7F5	0.78	19.06	58.76	-3.14	0.13	19.52	78.10	6.32

Table 4.2: Parameters of the fit of Eq. 4.20 against the results obtained from the completeness simulations for de Vaucouleurs profiles at five distinct redshifts $z \in \{0.5, 0.75, 1.0, 1.25, 1.50\}$. The normalisation p_0 provides a rough estimate of the height of the plateau the detection probability reaches. The break magnitude m_0 can be used as an approximation of the 50% completeness limit, if a higher maximum detection rate is reached.

Field	$z = 0.5$						$z = 0.75$						$z = 1.0$					
	p_0	m_0	α	β	p_0	m_0	α	β	p_0	m_0	α	β	p_0	m_0	α	β		
S2F1	0.97	19.12	103.55	-0.07	0.92	19.05	0.07	90.73	0.84	19.00	0.32	89.53	0.98	19.39	-0.05	111.26		
S2F5	0.98	19.39	-0.05	111.26	0.95	19.33	100.28	-0.04	0.86	19.28	89.29	0.41	0.69	19.04	0.08	100.67		
S3F1	0.69	19.04	0.08	100.67	0.67	18.96	90.41	-0.19	0.64	18.87	76.45	-0.59	0.99	19.54	-0.05	105.69		
S3F5	0.99	19.54	-0.05	105.69	0.97	19.44	-0.11	98.81	0.92	19.39	90.77	-0.18	S4F1	0.95	19.34	0.05	81.52	
S4F1	0.95	19.34	0.05	81.52	0.89	19.22	0.10	75.30	0.84	19.14	0.08	61.14	S5F1	0.99	19.35	-0.05	101.58	
S5F1	0.99	19.35	-0.05	101.58	0.96	19.26	90.01	-0.16	0.87	19.20	0.22	95.03	S5F5	0.99	19.38	107.76	-0.11	
S5F5	0.99	19.38	107.76	-0.11	0.94	19.31	95.69	0.00	0.88	19.22	0.10	87.80	S6F1	0.98	18.98	-0.21	104.80	
S6F1	0.98	18.98	-0.21	104.80	0.90	18.93	86.86	-0.07	0.81	18.84	82.68	0.07	S6F5	0.99	19.56	0.00	113.58	
S6F5	0.99	19.56	0.00	113.58	0.96	19.48	99.99	-0.03	0.93	19.42	-0.07	90.57	S7F5	0.98	19.37	-0.05	80.93	
S7F5	0.98	19.37	-0.05	80.93	0.95	19.27	-0.11	67.06	0.86	19.26	73.53	0.19						

Field	$z = 1.25$						$z = 1.5$						
	p_0	m_0	α	β	p_0	m_0	α	β	p_0	m_0	α	β	
S2F1	0.69	18.98	1.38	88.07	0.55	18.92	83.59	3.27	S2F1	0.69	18.98	1.38	88.07
S2F5	0.80	19.14	0.24	73.32	0.67	19.08	75.83	0.48	S2F5	0.80	19.14	0.24	73.32
S3F1	0.55	18.81	-0.24	78.43	0.31	18.86	84.16	6.05	S3F1	0.55	18.81	-0.24	78.43
S3F5	0.82	19.31	81.43	0.29	0.64	19.27	83.07	1.90	S3F5	0.82	19.31	81.43	0.29
S4F1	0.67	19.08	1.28	65.21	0.47	19.12	72.29	3.43	S4F1	0.67	19.08	1.28	65.21
S5F1	0.77	19.14	79.92	0.50	0.57	19.11	2.67	82.73	S5F1	0.77	19.14	79.92	0.50
S5F5	0.77	19.17	0.31	81.99	0.61	19.13	1.30	84.03	S5F5	0.77	19.17	0.31	81.99
S6F1	0.60	18.86	93.53	2.46	0.36	18.90	7.54	120.92	S6F1	0.60	18.86	93.53	2.46
S6F5	0.85	19.37	-0.06	88.12	0.68	19.32	93.77	1.25	S6F5	0.85	19.37	-0.06	88.12
S7F5	0.74	19.22	75.93	0.84	0.52	19.24	72.31	3.60	S7F5	0.74	19.22	75.93	0.84

Table 4.3: Parameters of the fit of Eq. 4.20 against the results obtained from the completeness simulations for exponential profiles at five distinct redshifts $z \in \{0.5, 0.75, 1.0, 1.25, 1.50\}$. The normalisation p_0 provides a rough estimate of the height of the plateau the detection probability reaches. The break magnitude m_0 can be used as an approximation of the 50% completeness limit, if a higher maximum detection rate is reached.

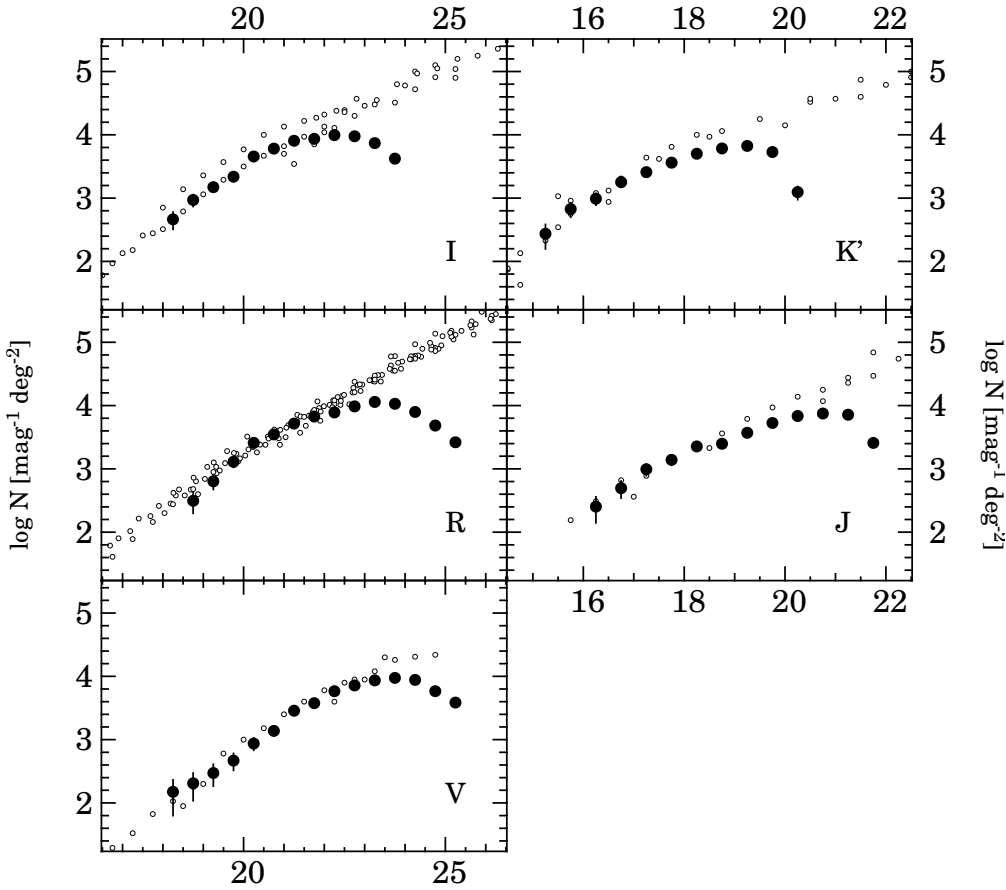


Figure 4.14: Number counts for galaxies in K' , J , I , R , and V from MUNICS data (filled circles) and previous studies (open circles), as described in the text. The counts shown are average number counts from all available MUNICS data and have not been corrected for incompleteness. Error bars indicate Poisson errors.

4.6 Galaxy number counts

In Table 4.4 we present number counts of galaxies in the MUNICS mosaic fields in all five filters K' , J , I , R , and V . These counts are also shown in Fig. 4.14, together with a compilation of number counts from the literature. Object catalogues were generated independently for each pass-band for this purpose, and star–galaxy separation is based on the PSF classification as described above, using only single pass-band information. The data were not transformed into the standard magnitude system for this comparison. Completeness corrections were not applied to these galaxy number counts. Corrected counts are presented in the context of a more detailed analysis in [Feulner \(2000\)](#). The counts are average counts from all the available MUNICS mosaic fields, with field-to-field variations in the number counts being on the level of 0.1 dex. The errors given in Table 4.4 only include Poisson errors.

The number counts are compared to the following literature values. [Gardner et al.](#),

mag	$\log n$	K'		J		I		R		V					
		σ_{low}	σ_{high}	$\log n$	σ_{low}	σ_{high}	$\log n$	σ_{low}	σ_{high}	$\log n$	σ_{low}	σ_{high}			
14.25	1.19	0.47	1.37												
14.75	2.11	1.38	2.32												
15.25	2.44	2.20	2.59												
15.75	2.83	2.70	2.93												
16.25	2.99	2.89	3.07	2.40	2.15	2.56									
16.75	3.25	3.18	3.32	2.69	2.54	2.81	2.14	1.61	2.34						
17.25	3.41	3.35	3.46	2.99	2.89	3.08	2.13	1.40	2.33						
17.75	3.56	3.51	3.61	3.14	3.06	3.21	2.38	2.15	2.53						
18.25	3.70	3.66	3.74	3.35	3.29	3.41	2.66	2.50	2.77	1.92	1.72	2.04	2.17	1.80	2.36
18.75	3.79	3.75	3.82	3.40	3.34	3.45	2.97	2.86	3.05	2.49	2.29	2.63	2.30	2.03	2.47
19.25	3.83	3.79	3.86	3.57	3.52	3.61	3.17	3.09	3.24	2.80	2.67	2.90	2.47	2.26	2.61
19.75	3.73	3.69	3.77	3.73	3.68	3.76	3.33	3.27	3.39	3.11	3.02	3.18	2.66	2.51	2.78
20.25	3.10	2.98	3.18	3.84	3.80	3.87	3.65	3.61	3.69	3.41	3.35	3.46	2.93	2.83	3.02
20.75				3.87	3.84	3.91	3.78	3.74	3.81	3.54	3.49	3.58	3.13	3.05	3.20
21.25				3.86	3.82	3.89	3.90	3.87	3.93	3.71	3.67	3.75	3.45	3.40	3.50
21.75				3.41	3.34	3.47	3.93	3.90	3.96	3.82	3.79	3.85	3.57	3.52	3.61
22.25							3.99	3.96	4.02	3.89	3.85	3.92	3.76	3.72	3.80
22.75							3.97	3.94	4.00	3.98	3.95	4.01	3.85	3.82	3.88
23.25							3.86	3.83	3.90	4.05	4.03	4.08	3.93	3.90	3.96
23.75							3.62	3.57	3.66	4.02	4.00	4.05	3.97	3.94	4.00
24.25							3.36	3.29	3.41	3.89	3.86	3.92	3.94	3.91	3.97
24.75							2.75	2.58	2.86	3.68	3.64	3.72	3.76	3.72	3.80
25.25										3.42	3.36	3.47	3.58	3.53	3.62
25.75										3.03	2.93	3.11	3.16	3.06	3.23

Table 4.4: K' , J , I , R , and V -band galaxy number counts for the MUNICS mosaic fields. The counts as a function magnitude and the error of the counts are given in logarithmic units. The values have not been corrected for incompleteness. The errors are Poisson errors only.

1993; Cowie et al., 1994; Glazebrook et al., 1994; Djorgovski et al., 1995; Gardner et al., 1996 for the K band, Saracco et al., 1999; Teplitz et al., 1999 for the J band, Tyson, 1988; Lilly et al., 1991; Casertano et al., 1995; Gardner et al., 1996; Williams et al., 1996; Huang et al., 1998 for the I band, Couch & Newell, 1984; Hall & Mackay, 1984; Infante et al., 1986; Koo, 1986; Stevenson et al., 1986; Yee & Green, 1987; Tyson, 1988; Jones et al., 1991; Metcalfe et al., 1991; Picard, 1991; Couch et al., 1993; Steidel & Hamilton, 1993; Driver et al., 1994; Metcalfe et al., 1995,?; Smail et al., 1995; Metcalfe et al., 1996; Bertin & Dennefeld, 1997; Hogg et al., 1997; Arnouts et al., 1999; Metcalfe et al., 2000 for the R band, and Driver et al., 1994; Casertano et al., 1995; Gardner et al., 1996 for the V band.

We generally find good agreement with previously published number counts in all pass-bands, again as a consistency check confirming the quality of our photometry.

4.7 Colour distributions and objects at $z \geq 1$

In Fig. 4.15 we show the $J-K'$ vs. K' colour-magnitude diagramme and the $R-J$ vs. $J-K'$, $V-I$ vs. $J-K'$, and $V-I$ vs. $V-R$ colour-colour diagrammes for MUNICS data from three mosaic fields. The total number of objects shown is 2977, of which 286 are classified as point-like. These plots also contain the tracks defined by the stellar population synthesis models described in detail in Sect. 2.2.2. Briefly, the models are an SSP, and three exponential star formation histories with e -folding times of 1, 3, and 10 Gyr forming at $z = 4$. The models have been normalised such that they represent typical L^* objects at $z = 0$, with L^* chosen according to their ‘photometric’ Hubble type. The cosmology adopted is again $H_0 = 65, \Omega_0 = 0.3, \Omega_\Lambda = 0.7$.

These models reasonably envelope the region in the colour-magnitude $J-K'$ vs. K' plane occupied by the data, with the SSP model following the outline of the data points along the bright and red edge as might be expected since any further star formation or a later formation epoch would render the object bluer relative to the SSP.

It is also worth noting that the models constitute a continuous sequence with the duration of the star formation as the parameter in the $R-J$ vs. $J-K'$ plane, closely following the SSP track up to a redshift of ~ 1 , then rapidly turning bluer in $R-J$ while still getting redder in $J-K'$. A significant fraction of objects between the SSP and the 1 Gyr track is compatible with being well evolved objects at a redshift $z \gtrsim 1$.

We finally conclude from these diagrammes that the quality of our data meets the requirements expressed in Sect. 2.2 and that we are in a position to construct a catalogue containing a large number of massive field galaxies in the redshift range $0.5 \lesssim z \lesssim 1.5$ to study their evolution in detail.

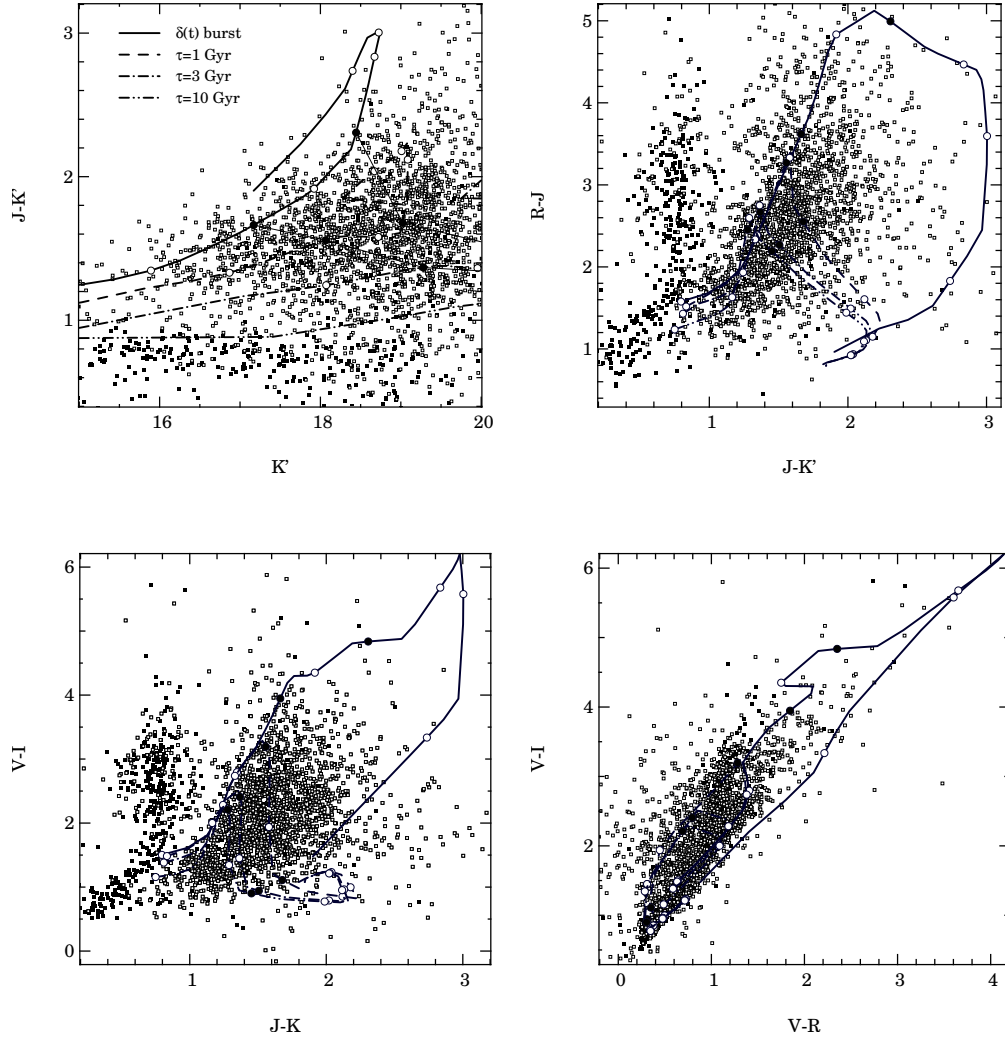


Figure 4.15: Colour–magnitude and colour–colour diagrammes for MUNICS objects taken from 3 mosaic fields (S2 f1–f4, S6 f5–f8, and S7 f5–f8) containing 2977 sources. Objects classified as stellar are marked with filled squares, extended objects are marked with open squares. Also shown are stellar population synthesis models for different star-formation histories. The model parameters are the same as in Fig. 2.3. Redshift along the model tracks is marked by circles at a z spacing of 0.5, with $z = 1$ and $z = 2$ being accentuated by filled circles. The lines of constant redshift at $z = 1$ and $z = 2$ are drawn as thin solid lines.

Chapter 5

The rest-frame K -band luminosity function

The luminosity function (LF) is a basic and fundamentally important statistic used to study galaxy populations and their evolution, since a measurement of the galaxy LF at different redshifts provides a simple means of describing the global changes in the galaxy population with cosmic time.

In this chapter, we aim at measuring the rest-frame K -band luminosity function and its evolution with redshift in the range $0.4 < z < 1.2$ using the MUNICS data set. First, we introduce the sample in Sect. 5.2. Next, we describe the application of the photometric redshift estimation technique to this sample, relying on a complementary spectroscopic sample for calibration (Sect. 5.3). We proceed to discuss the resulting cumulative redshift distribution and its implications for theories of galaxy formation in Sect. 5.4. The luminosity function is presented and discussed in Sect. 5.5 and Sect. 5.6.

5.1 Introduction

Recent observational progress in measuring the optical field galaxy LF has spanned a very wide range of redshifts. Locally, results from the 2dF survey (Folkes et al., 1999) and 2MASS (Kochanek et al., 2001) provide much improved measurements of the type-dependent LF. At redshifts $z \lesssim 1$ a number of results has been published in recent years, e.g. (Lilly et al., 1995b; Heyl et al., 1997; Lin et al., 1997; Liu et al., 1998; Ratcliffe et al., 1998; Lin et al., 1999). Simultaneously, first results at $z \sim 3$ became available through the study of Lyman-break galaxies (Shapley et al., 2001).

In spite of some controversy regarding the normalisation and the very faint end slope of the local LF, it is a well established result that the LF depends on galaxy type in the sense that the faint end is dominated by galaxies of later morphology, later spectral type and bluer colour, and stronger line emission. The bright end is dominated by early-type spirals and the very bright end by (giant) ellipticals (e.g. Marzke et al., 1994; Bromley et al., 1998; Folkes et al., 1999).

The LF situation is somewhat less controversial at intermediate redshifts. At $0.2 \lesssim z \lesssim 1$ the above mentioned R or I -band selected surveys (with samples of typically

Field	Area/arcmin ²	Field	Area/arcmin ²
S2F1	118.7	S5F5	107.6
S2F5	124.1	S6F1	130.8
S3F5	115.3	S6F5	140.2
S5F1	121.9	S7F5	139.1

Table 5.1: List of the Mosaic Fields with best photometric homogeneity, good seeing, and similar depth. The total area amounts to 0.27 square degrees. There are ~ 5000 objects in the corresponding catalogue

hundreds of objects) have consistently found similar trends in the evolution of the rest-frame *B*-band field galaxy LF. The main result was the contrast between the rapid evolution of the blue, star-forming sub-population and the mild change in the redder, early-type population.

Here, we present a measurement of the rest-frame *K*-band LF at $0.4 < z < 1.2$. Since the *K*-band light is much less sensitive to ongoing star-formation and much less dependent on galaxy type compared to the *B*-band (see Sect. 2.1), we hope to be able to move from a picture dominated by the evolution of star formation to one which focuses on the assembly history of mass in these systems.

We assume $\Omega_M = 0.3$, $\Omega_\Lambda = 0.7$ throughout this chapter. We write Hubble’s Constant as $H_0 = 100 h \text{ km s}^{-1} \text{ Mpc}^{-1}$, using $h = 0.65$ unless the quantities in question can be written in a form explicitly depending on h .

5.2 The galaxy sample

The galaxy sample used here is a subsample of the MUNICS survey Mosaic Fields, selected for best photometric homogeneity, good seeing, and similar depth. Furthermore, in each of the remaining survey patches, areas close to the image borders in any passband, areas around bright stars, and regions suffering from blooming are excluded. The subsample covers 0.27 square degrees in *V*, *R*, *I*, *J*, and *K*. Table 5.1 lists the Mosaic Fields used in the subsequent analysis.

The QSO-fields were not used in the present analysis as they lack the spectral coverage and cover a relatively small total area. The galaxy population in those fields, in particular the spatial correlation function in the neighbourhood of the QSO is analysed in Snigula (2000).

Stars were identified following the procedure described in Sect. 4.3, adding a colour criterion in the *J–K* vs. *V–I* plane (see Fig. 4.15). The colour criterion may also exclude $z \lesssim 0.25$ compact blue galaxies. Such galaxies are very unlikely to be present in the *K*-selected sample, given our magnitude limit. Since we will restrict our analysis of the luminosity function to $z > 0.4$ for reasons given below, this is anyway not a problem.

The final catalogue covers an area of 997.7 square arcmin and contains 5132 galaxies.

5.3 Photometric redshifts

Photometric redshifts were derived using the method presented in [Bender et al. \(2001\)](#). This method is a template matching algorithm rooted in Bayesian statistics. It closely resembles the method presented by [Benítez \(2000\)](#). The templates are derived by fitting stellar population models of [Maraston \(1998\)](#) to combined broad-band energy distributions of MUNICS galaxies with spectroscopic redshifts. In this way, representative galaxy templates of mixed stellar populations (variable age, metallicity, and dust extinction) optimised for the MUNICS dataset are obtained.

5.3.1 Construction of SED templates

Using the spectroscopic sample introduced in Sect. 2.3.5, SED templates for the determination of photometric redshifts were constructed by the following iterative method.

A subsample ($\sim 50\%$) of the objects with spectroscopically determined redshifts is chosen. The observed-frame apparent magnitudes of these objects are transformed to rest-frame redshift zero via

$$m^i \left(\frac{\lambda_{eff}^i}{1+z} \right) = m^i(\lambda_{eff}^i) - d(z) - 2.5 \log(1+z), \quad (5.1)$$

where z is the spectroscopic redshift, λ_{eff}^i is the effective wavelength of the observed passband i , for each $i \in \{V, R, I, J, K\}$, and $d(z)$ is the distance modulus.

These rest-frame colours are then normalised to a common luminosity and sorted into distinct “types”. For each type one obtained multiple sampling points of its SED, five samples from each observed object of that particular type at wavelengths corresponding to the de-redshifted observed-frame pass bands. If the number of observed objects is large enough and if those are spread evenly in redshift, one obtains a densely sampled SED, effectively constructing a low-resolution spectrum from the observed magnitudes. This procedure is illustrated in Fig. 5.1.

Then an SED is fitted to each of these types, and this initial set of SEDs is used to determine photometric redshifts of the total sample of objects having spectroscopic redshifts. The photometric redshifts are compared to the spectroscopic ones, and, additionally, the same de-redshifting procedure is applied to the spectroscopic sub-sample not used for the initial construction of the SEDs, only that now we group the objects by the SED that gave the best fit during the determination of the photometric redshift.

Using this comparison, deficiencies in the set of SEDs can be identified as those become apparent through systematic offsets between the de-redshifted magnitudes and the SED templates. This is the case since such deficiencies lead to a wrongly determined photometric redshift and therefore to the assignment of a wrong SED (or, as such, type).

Using this knowledge, the procedure is repeated with a refined set of SEDs, by changing SEDs, abolishing some and adding others, until a satisfactory library of template SEDs is found.

Fig. 5.2 shows the final template SED library. Note that there are no strongly star forming (young) SEDs in the final set, as can be expected in a K -band selected sample.

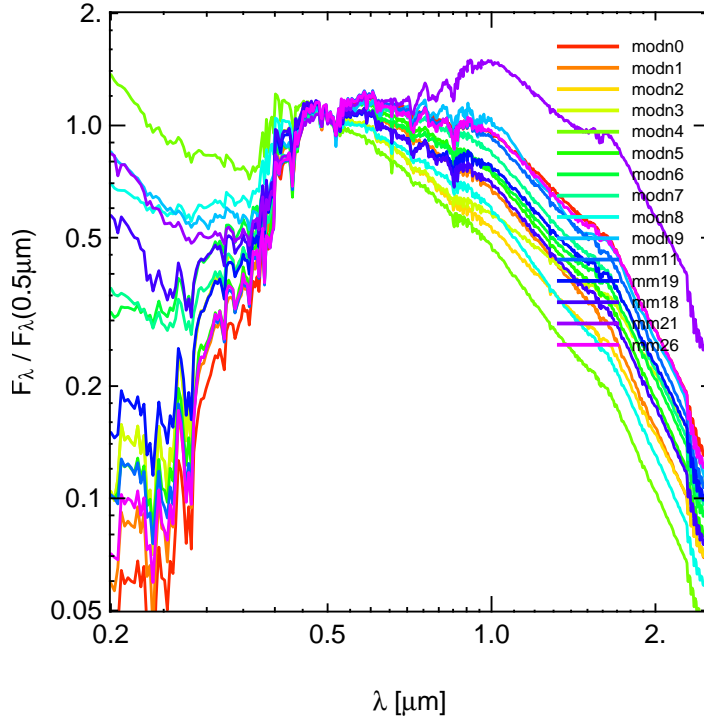


Figure 5.2: Final SED library for determining photometric redshifts. Note that there are no strongly star forming (young) SEDs in the final set, as can be expected in a K -band selected sample. Also noteworthy is the fact that we definitely need dust-reddened SEDs.

is no irregular galaxy having $M_K = -25$ into the system, which allows us to reduce the impact of colour/redshift degeneracies causing catastrophically wrong redshift estimates.

Applying Bayes' theorem, we can write

$$p(z, T|C, m) = \frac{p(z, T|m)p(C|z, T)}{p(C)} \propto p(z, T|m)p(C|z, T). \quad (5.2)$$

Here the expression $p(C|z, T) \equiv \mathcal{L}(z, T)$ is the usual likelihood of observing the colours C if the galaxy is of type T at redshift z . The a priori probability $p(C)$ of observing colours C is a normalisation constant and there is no need to calculate it.

The first factor, the prior probability, $p(z, T|m)$, is the redshift and type distribution of galaxies of magnitude m . In case we have no a priori knowledge, it will be taken to be constant, $p(z, T|m) = 1$. In this case, the results are identical to a maximum likelihood approach.

To calculate $p(z, T|C, m)$ we still need to specify the likelihood of obtaining the measured fluxes if the galaxy is of type T and redshift z . Assuming that the errors in measuring fluxes are Gaussian, we can write

$$-\log \mathcal{L}(z, T) \propto \chi^2(z, T, b) = \sum_i \frac{(f^i - bF_T^i(z))^2}{(\sigma_f^i)^2}, \quad (5.3)$$

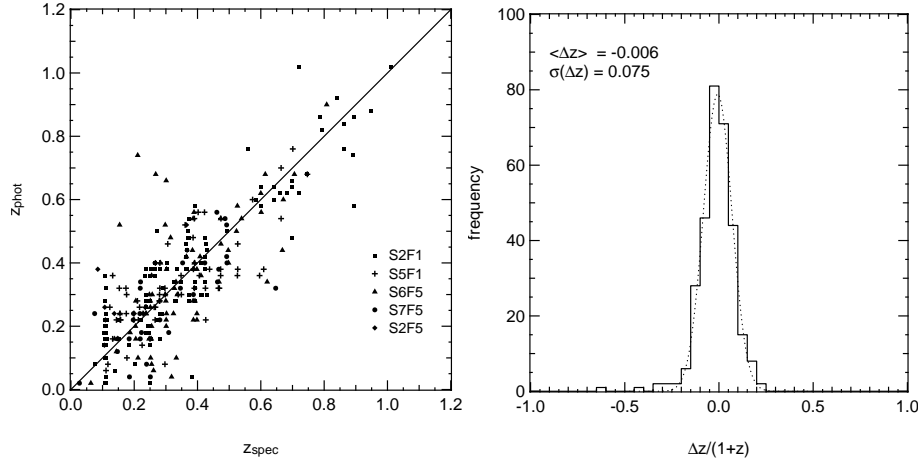


Figure 5.3: Left panel: Comparison of photometric and spectroscopic redshifts for 310 objects in five survey patches (different symbols). Middle panel: The histogram of the redshift errors. The rms scatter is consistent with a Gaussian (dotted line: best-fit Gaussian) of a width $\sigma = 0.075$ and an insignificant mean deviation from the unity relation of $\langle \Delta z \rangle = -0.006$. Right panel: The distribution of photometric redshifts (solid histogram) and a best-fit analytic description (dotted line) as well as the distribution of spectroscopic redshifts (dashed line).

where, again, $i \in \{V, R, I, J, K\}$ denotes the pass-band, f^i and σ_f^i are the measured fluxes and their errors. The $F_T^i(z)$ are the predicted fluxes of the template T at redshift z in the observed pass-bands, and b the flux normalisation factor.

Combining Eqs. 5.2 and 5.3, one finds the most likely redshift by searching for maxima in $p(z, T|C, m)$, calculated over some grid in z . If one is only interested in the redshift, one should marginalise over the type T to obtain

$$p(z|C, m) = \sum_T p(z, T|C, m) \propto \sum_T p(z, T|m) p(C|z, T). \quad (5.4)$$

In our case, though, we want to preserve the type information, and so we assign to each object the redshift z and type T at which $p(z, T|C, m)$ reaches its global maximum.

5.3.3 Application of the technique

In Fig. 5.4 we show three instructive examples of photometric redshifts determinations. These examples and their implications are discussed below.

Firstly, an object at low redshift ($z \lesssim 0.3$), where the 4000\AA break is not yet sampled by our filter set. These objects tend to have rather flat and broad redshift probability functions, with multiple SEDs reaching almost equally high probabilities. Therefore, their redshifts are insecure, and any value $z \lesssim 0.3$ is equally well acceptable. Since the relative redshift error is large in those cases, the relative error in the distance and absolute magnitude will be large, too, and we will therefore restrict ourselves to objects with $z > 0.4$ in what follows. Note that the absolute error in redshift does not seem to increase notably at small redshifts, as can be seen in Fig. 5.3.

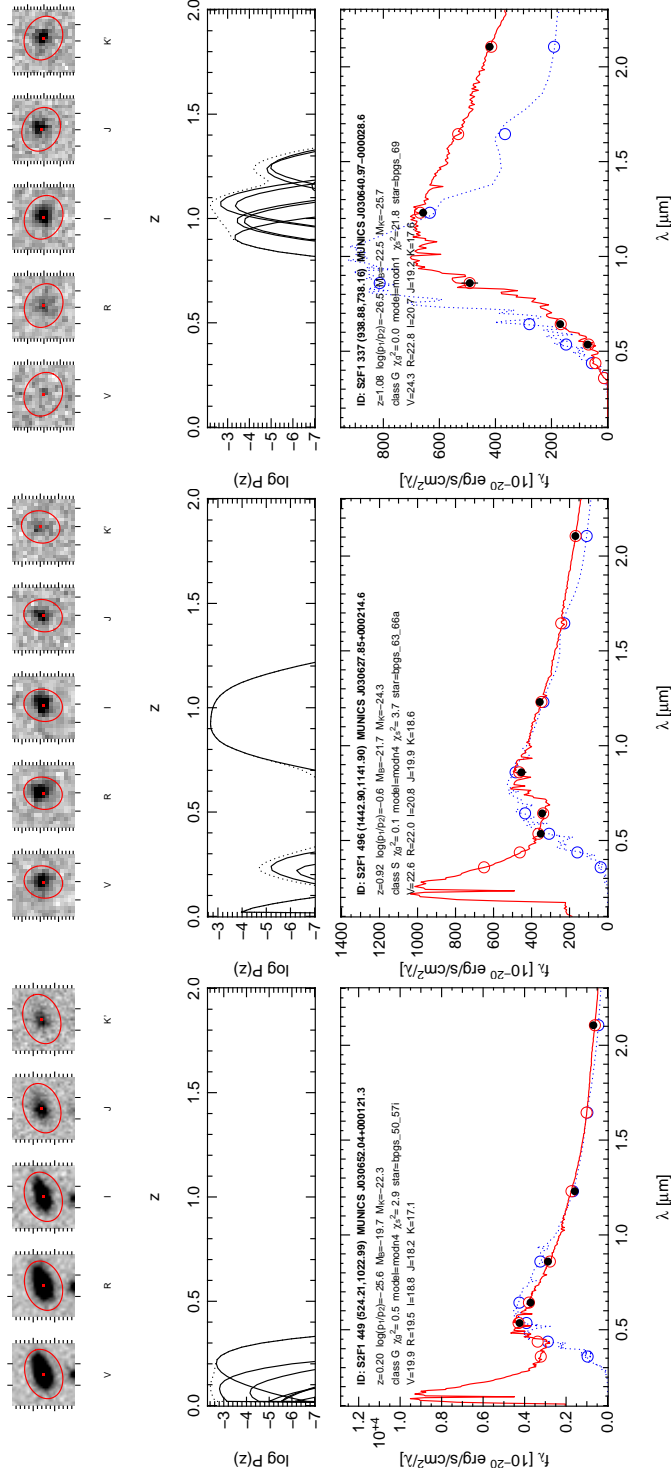


Figure 5.4: Examples of the determination of photometric redshifts. The implications of these examples are discussed in the text. The lower panels show the best-fitting galaxy SED (solid line), the best-fitting stellar SED (dotted line), the expected fluxes in observed-frame V, R, I, J , and K (open circles) and the measured fluxes (filled circles). The middle panel shows the redshift probability function (Eq. 5.2) for the different template SEDs and the total redshift probability function (Eq. 5.4). The upper panels show thumbnail images of the objects in our five pass bands.

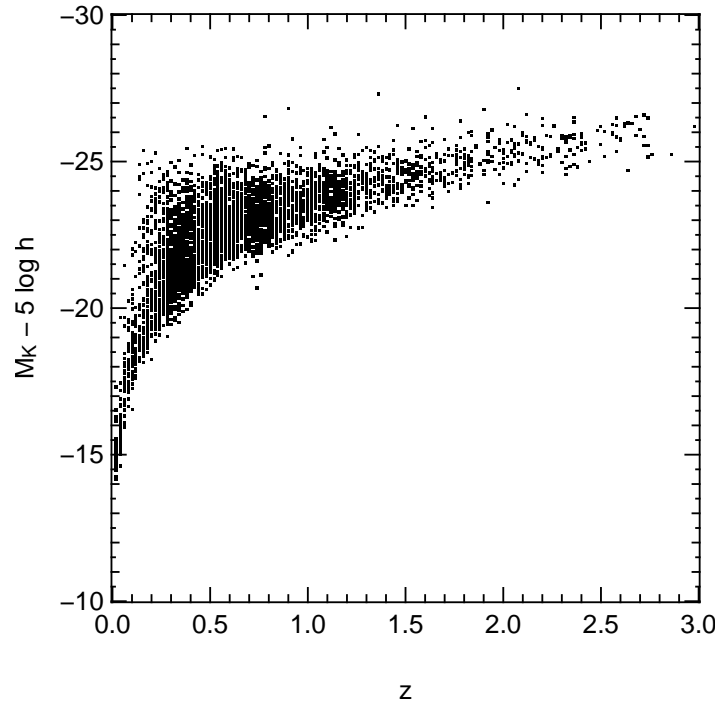


Figure 5.5: The $M_K - z$ relationship for the total MUNICS sample of 5132 galaxies using photometric redshifts.

Secondly, a spiral-like system at redshift around unity. This object is being fit by the bluest SED in our template library. Here the 4000\AA break is redshifted beyond the R -band filter, and the redshift is determined pretty well with only one SED forming the global peak in the redshift probability distribution. Note that although the assignment of this bluest SED seems unambiguous, we nevertheless do not have a good handle of how blue the SED of this object actually is (what the star formation rate may be), since we still do not sample the UV rise in the spectrum.

From this and the above example we may learn that the lack of photometry in bluer pass bands than V is of more harm to the meaningfulness of the SED classification than to the actual determination of the redshift (except for the reduction of scatter, maybe).

Thirdly, an early-type object at redshift $z \approx 1$. The redshift determination, although there are competing SEDs around the global peak, can be regarded as quite secure. The 4000\AA break is in the I band, the object is barely detected in R and essentially undetected in V . The error in the photometry is accordingly large in these two pass bands and hence the insecurity in the SED assignment: as the rest-frame blue slope of the spectrum is not firmly determined, slightly differing effective ages of the underlying stellar population are giving reasonable fits.

Common to all above examples is that the position in redshift of the global maximum of the total redshift probability distribution, $p(z|C, m)$, is always compatible with the redshift one would derive by looking at the probability distribution $p(z, T|C, m)$ of the most likely SED.

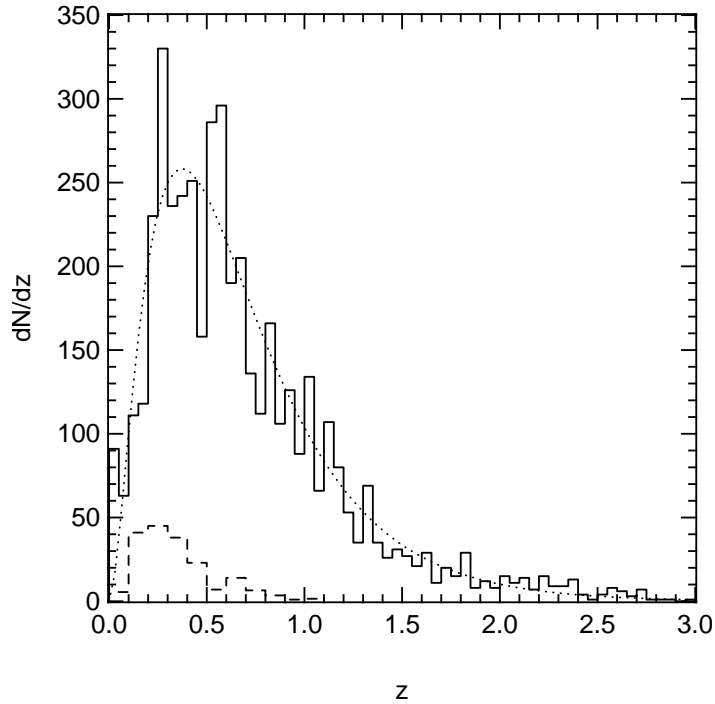


Figure 5.6: The redshift distribution of the total sample of 5132 galaxies as obtained using photometric redshifts (solid histogram) and a best-fit analytic description (dotted line; see text) as well as the distribution of spectroscopic redshifts (dashed line).

Finally, we plot absolute K -band magnitude vs. redshift as obtained from the photometric redshifts in Fig. 5.5, and the redshift distribution of the total sample discussed here, containing 5132 galaxies, in Fig. 5.6. The distribution peaks around $z \approx 0.5$ and has a tail extending to $z \approx 3$. An analytical fit of the form

$$\frac{dN}{dz} = \frac{\beta z^2}{\Gamma(3/\beta) z_0^3} e^{-(z/z_0)^\beta} \quad (5.5)$$

is also shown. The best-fitting values are $z_0 = 0.101$, $\beta = 0.746$.

5.4 The cumulative redshift distribution

The star formation histories of galaxies pose one of the major challenges to current models of galaxy formation within the framework of CDM and its implied paradigm of hierarchical assembly of galaxies.

Within these models, massive galaxies (luminous ellipticals S0s and massive early-type spirals) are assembled relatively late through merging of smaller subunits (Kauffmann et al., 1993; Baugh et al., 1996; Cole et al., 2000), which seems to be in contradiction by the observational evidence for apparently old ages of elliptical galaxies and S0s (Bender et al., 1996; Bernardi et al., 1998; Schade et al., 1999; Thomas, 2001).

Kauffmann & Charlot (1998) proposed to use the rest-frame *K*-band luminosity function and its evolution with redshift as a means to discriminate between the two scenarios for the formation of massive galaxies: the hierarchical paradigm on the one hand and the “traditional” view that massive galaxies form early (or even first) and evolve “passively”, i.e. with strongly declining star formation rates since at least a redshift of $z \lesssim 2$.

Since the predictions for the number density of such systems differ most for the most massive systems, the redshift distribution of *K*-band bright galaxies offers a first opportunity to test the models. If we believe that *K*-band light roughly traces stellar mass (see Sect. 2.1), the redshift distribution of bright *K*-selected galaxies will trace the stellar mass assembled in massive galaxies at each redshift. In particular, the presence of *K*-band bright objects at high redshift ($z \gtrsim 1$) is indicative of a higher formation redshift for an early formation time.

Kauffmann & Charlot (1998) compared the prediction of hierarchical models and of Pure Luminosity Evolution (PLE) models to data, using the very small *K*-selected spectroscopic samples available at that time (Songaila et al., 1994; Cowie et al., 1996), containing 118 galaxies with $16 < K < 18$ and 52 galaxies with $18 < K < 19$, respectively.

They found that much fewer galaxies are observed at high redshift than predicted by a pure luminosity evolution (PLE) model and that the data strongly favour the hierarchical scenario.

Fontana et al. (1999) repeated the test using deeper data from the HDFs and the NTT Deep Field (319 *K*-selected galaxies) reaching $K = 21$ AB mag, reaching essentially the same conclusion.

In Fig. 5.7 we show the hierarchical and the PLE model from Kauffmann & Charlot (1998) along with data from 8 MUNICS Mosaic Fields containing 1550 galaxies with $16 < K < 18$. In this magnitude range, the MUNICS data may be regarded as complete (see Sect. 4.5.8 and Appendix B).

With our much larger sample (and purely *K*-selected as we do not depend on the success of optical spectroscopic redshift identification, which may introduce a bias against red and therefore old objects), the situation is not as clear. In our case the observed redshift distribution lies above the hierarchical prediction and below the PLE prediction.

This result can be understood in terms of a compromise between the competing scenarios: the assembly of massive galaxies seems to take place somewhat earlier than predicted by the hierarchical models and probably the merging systems needed to build up early-type objects themselves contain fairly old stellar populations. On the other hand it is clear, the PLE picture must break down at some point.

The intriguing thing here is that the data lie below the PLE predictions even at small redshifts. The reason for this is not immediately explainable. It may be noteworthy, though, that there is no unique PLE prediction for composite stellar population and that PLE models of different authors therefore strongly depend on the assumed star formation timescales for spirals (usually modelled as exponential decays) and on the local normalisation in terms of the adopted luminosity functions for different Hubble types. At least at the (rather shallow) depth reached by the MUNICS data, this test

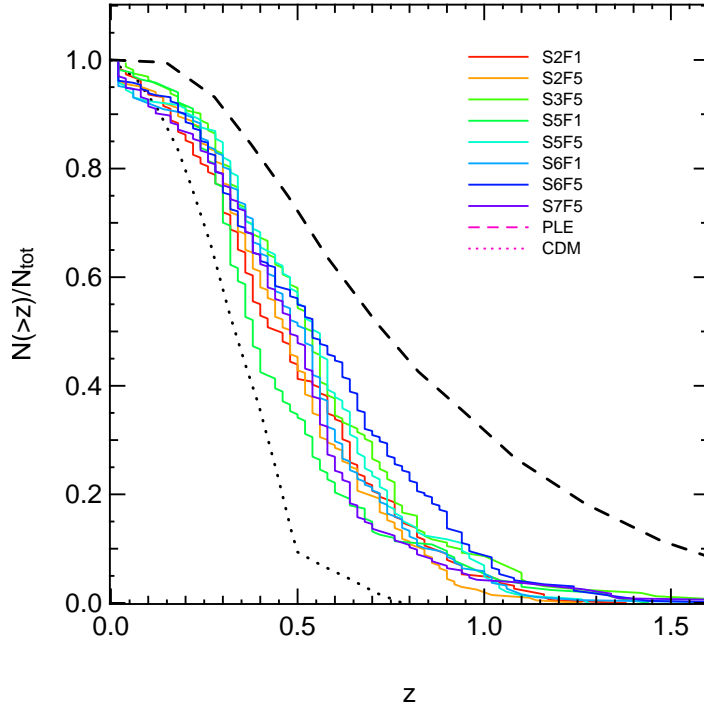


Figure 5.7: The redshift distribution of $16 < K < 18$ galaxies using MUNICS photometric redshifts in 8 Mosaic Fields (solid lines). The dashed line is the hierarchical model, the dotted line the PLE model from [Kauffmann & Charlot \(1998\)](#).

may not be as powerful a discriminant than initially thought.

5.5 Computing the luminosity function

5.5.1 The V_{\max} method

The luminosity function (LF) $\Phi(M)dM$, the comoving number density of objects with absolute magnitude in the range $[M, M + dM)$, is computed using the V_{\max} formalism ([Schmidt, 1968](#)) to account for the fact that some fainter galaxies are not visible in the whole survey volume.

Each galaxy in a given redshift bin $[z_l, z_h)$ contributes to the number density an amount inversely proportional to the volume in which the galaxy is detectable in the survey given all relevant observational constraints:

$$V_i = d\Omega \int_{z_l}^{\min(z_h, z_{max})} \frac{dV}{dz} dz, \quad (5.6)$$

where dV/dz is the comoving volume element, $d\Omega$ is the survey area, z_{max} is the maximum redshift at which galaxy i having absolute magnitude $M_{K,i}$ is still detectable given the limiting apparent magnitude of the survey and the galaxy's SED (the best-fit SED from the photometric redshift determination).

Additionally, the contribution of each galaxy i is weighted by the inverse of the detection probability, $P(m_{K,i})$, where we assume that the detection probability is independent of the galaxy type and can be approximated by that of point-like sources. We only include objects with $P(m_{K,i}) > 0.75$, such that this correction is always small. We have checked that this correction does not bias our results by comparing to what we get for higher completeness limits. Also, the results discussed in Sect. 4.5 demonstrate that although there exist profile-dependent surface-brightness selection biases, these are under control for redshifts up to $z \gtrsim 1$, and that the onset of incompleteness is roughly independent of profile type.

The comoving number density of objects in a given absolute magnitude interval and redshift bin is finally calculated as

$$\Phi(M)dM = \sum_i \frac{1}{V_{\max}^i} \frac{1}{P(m_{K,i})} dM, \quad (5.7)$$

where the sum is to be taken over all objects i in the bin.

The advantage of the V_{\max} method is that it is non-parametric, i.e. no assumption on the form of the LF is made and the estimate of the LF in each bin is independent. There is no need to compute the normalisation of the LF separately. It is quick and easy to compute. The major disadvantage is that this method is sensitive to clustering in the sample. In our case we might hope that this is not a major concern since we average over a large volume and probe multiple independent lines of sight.

Takeuchi et al. (2000) performed a systematic comparison of different estimators for the luminosity function, finding that the V_{\max} estimator yields a completely unbiased result if there is no inhomogeneity. Earlier claims that the V_{\max} estimator is biased even without clustering were not confirmed. The V_{\max} estimator was also found to give consistent results with other statistical estimators analysed, despite of its sensitivity on large scale structure.

The last missing ingredient is the absolute *K*-band magnitude. It is computed by extrapolation from the observed-frame colours, using the best-fit SED from the photometric redshift code. The near-IR slopes of the SEDs are fairly uniform (the *K*-band k -corrections are small and almost type-independent) and so the uncertainty introduced by this extrapolation is rather small, of the order of $\Delta M_K \sim 0.1$ mag in the mean, and thus small compared with the uncertainty of the total rest-frame *K*-band magnitude coming from the uncertainty in the distance.

5.5.2 Monte-Carlo simulations

The use of photometric redshifts, in general, can introduce systematic errors in the derived galaxy distances, and therefore in the luminosity function and mass function that we want to derive in what follows. To investigate these errors, we performed the following tests:

- Templates were derived for a subsample of objects with spectroscopic redshifts and their suitability for the whole galaxy sample was verified using the remaining objects with spectroscopy as described above.

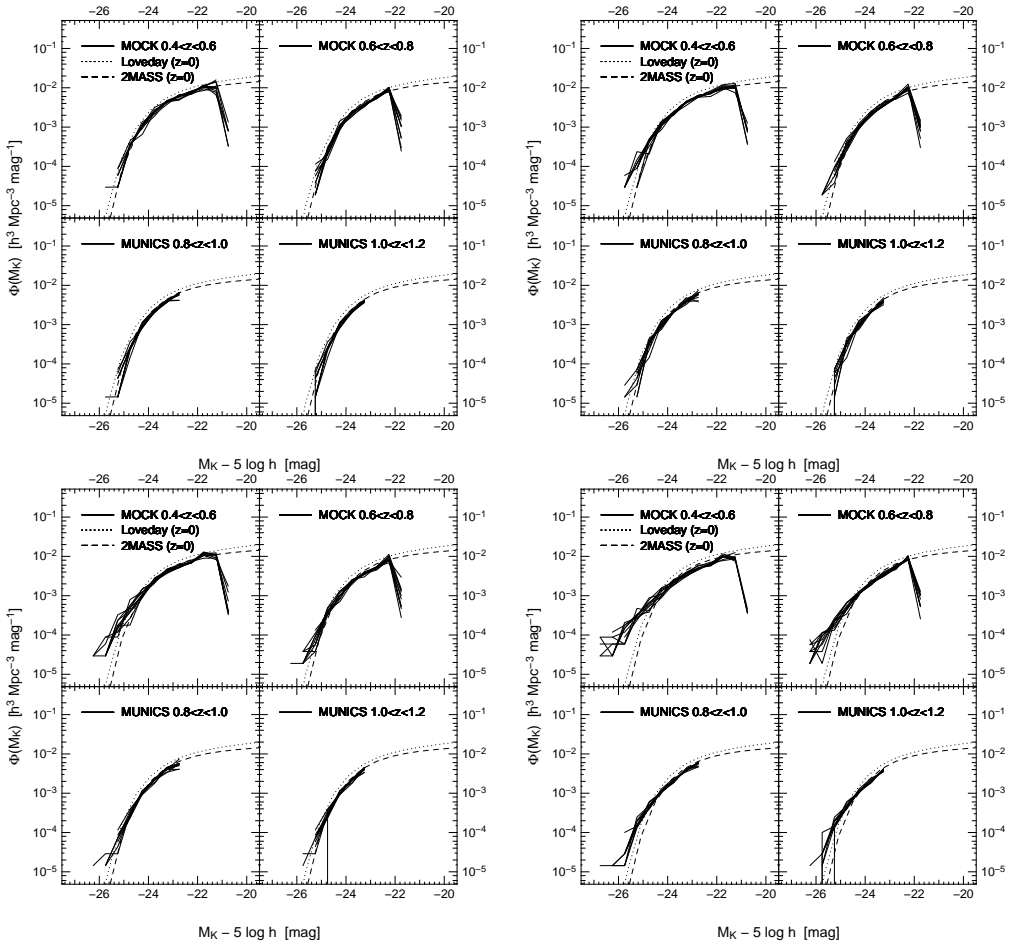


Figure 5.8: Monte-Carlo realisations of the luminosity function to test the susceptibility to errors in the redshift determination due to photometric redshifts. The LFs were simulated with redshift errors Δz drawn from a Gaussian of width 0.02 (upper left), 0.075 (upper right), 0.1 (lower left), and 0.2 (lower right). In each panel, the LF is shown in four redshift bins, $0.4 < z < 0.6$, $0.6 < z < 0.8$, $0.8 < z < 1.0$, and $1.0 < z < 1.2$ (see text). Each simulation was repeated 10 times, with each run containing the same total number of galaxies as the real MUNICS sample. The form of the simulated LF is that of the local Kochanek *K*-band LF. The redshift distribution (the normalisation) follows the redshift distribution of the real MUNICS sample.

- Using subsets of the final template library, we estimated the errors in the luminosity and mass functions introduced by a finite (and incomplete) set of templates. These errors were included in our error budget in the analysis of the mass function.
- Monte-Carlo simulations were performed to investigate the influence of photometric redshift errors on the luminosity function and the galaxy number densities.

To test the robustness of the LF estimate under the conditions imposed by the use of photometric redshifts instead of spectroscopic distances, Monte-Carlo simulations were performed. We generated mock MUNICS-like catalogues following some assumed LF and compared the output of the LF estimation as described above with the input LF.

The redshift distribution of the objects was assumed to follow the distribution obtained from the analytic fit (Eq. 5.5) to the distribution of the photometric redshifts. This fixes the normalisation of the simulated LF, so we are left with its form as the only free parameter.

The underlying assumption is that a rms redshift error of the order of ~ 0.1 does not significantly change the form of the distribution, except for smoothing it with a kernel of that width. Note that from comparison with spectroscopically determined redshifts we found the mean error of the photometric redshift estimate to be Gaussian and unbiased (Fig. 5.3). So we assume that the redshift distribution as we measure it resembles the true one close enough.

The form of the simulated LFs was chosen to match the local Schechter form with $M^* = -23.39$, $\alpha = -1.09$ as determined in the *K*-band by Kochanek et al. (2001).

The extrapolation of the rest-frame *K*-band magnitude was done using a the mean *k*-correction of the models used for determining photometric redshifts.

To investigate the influence the errors in the photometric redshifts have on recovering the form of the LF, we have simulated four data sets with errors Δz drawn from a Gaussian of width 0.02, 0.075 (the value found from the comparison with spectroscopic redshifts in Fig. 5.3), 0.1, and 0.2. The simulations were repeated 10 times, each run containing the same total number of objects (5132) as the total MUNICS data set. The LF was extracted in four redshift bins, $0.4 < z < 0.6$, $0.6 < z < 0.8$, $0.8 < z < 1.0$, and $1.0 < z < 1.2$. The results are shown in Fig. 5.8.

The overall impression from Fig. 5.8 is that the form is well reproduced, and that, as expected, the influence of the redshift uncertainty is larger at small redshifts where the relative error in the distance is largest. The form of the LF only becomes significantly biased when the redshift errors exceed $\Delta z \gtrsim 0.1$. For the value $\Delta z = 0.075$, the form is slightly affected only in the lowest redshift bin, $0.4 < z < 0.6$, producing too many high luminosity objects and too few sub- L^* galaxies.

From the last said we conclude that the shape of the luminosity function is not significantly biased as long as the photometric redshifts scatter symmetrically around the true redshifts (see also Subbarao et al., 1996) and their errors are (significantly) smaller than the bin size in z over which the luminosity function is averaged.

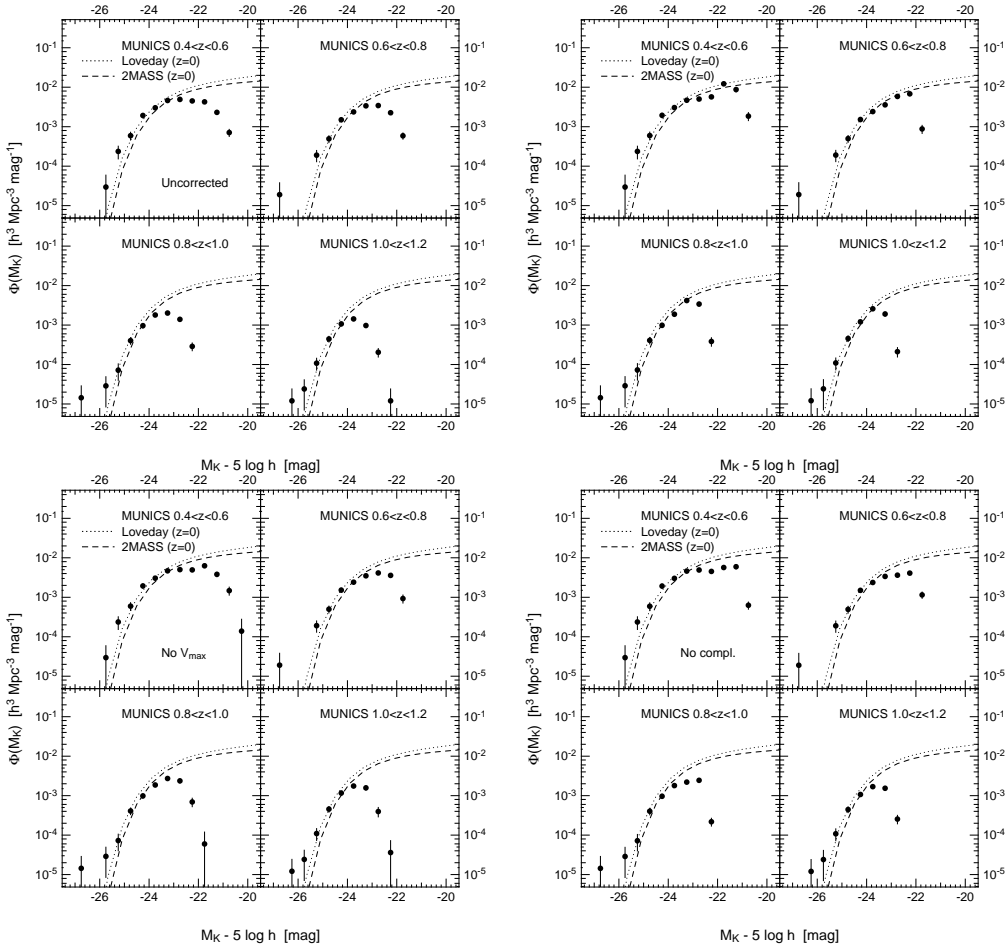


Figure 5.9: Comparison of the uncorrected and the fully corrected luminosity function. The upper left panel shows the completely uncorrected luminosity function (no V_{\max} no detection incompleteness correction, simple N/V estimator), the upper right panel shows the fully corrected LF. The lower left panel shows the LF with only detection probability correction (N/V estimator) and the lower right panel shows the LF computed with the V_{\max} estimator and no correction for the detection incompleteness. The dotted and dashed lines denote the local K -band LF published by Loveday (2000) and Kochanek et al. (2001), respectively.

5.6 Results

In this section we present the results on the evolution of the rest-frame K -band luminosity function to $z \leq 1.2$.

5.6.1 Influence of the completeness corrections

The corrections for incompleteness involve the volume correction, $1/V_{\max}$, and the correction for the detection incompleteness at fainter magnitudes, $1/P(m_{K,i})$.

Fig. 5.9 compares the raw data (the LF computed via the trivial N/V_{bin} estimator) to the fully corrected data. Also shown is a comparison to the LF calculated using only the detection incompleteness term and to the LF calculated using only the V_{\max} term.

Clearly both corrections do not play any role at magnitudes brighter than $M_K^* \approx -23.5$. At fainter magnitudes both corrections contribute significantly. The V_{\max} term becomes dominant at the faintest levels (as we exclude objects with $P(m_{K,i}) < 0.75$).

In the lowest redshift bin the V_{\max} term becomes unstable resulting in wiggles in the LF's faint end. This is understandable in terms of objects, mostly dwarfish irregular galaxies which are only detected at smaller redshifts, having true redshifts lower than the bin's lower bound, that are scattered upwards in z by the photometric redshift estimate and make it into that bin. As those galaxies are close to the detection limit, the V_{\max} test predicts them to be detectable only in a very small volume of the bin and therefore the V_{\max} correction becomes large (factors of 3 and above), producing the observed behaviour. We conclude that our data do not allow us to place constraints on the faint end slope of the LF, even in our lowest redshift bin.

5.6.2 The final rest-frame K -band luminosity function

In Fig. 5.10 we plot the final rest-frame K -band luminosity function as derived from the present MUNICS dataset, employing spectroscopically calibrated photometric redshifts. For comparison we also show the local $z = 0$ K -band LF by Loveday (2000) and Kochanek et al. (2001).

The figure shows the corrected and the raw data. In the corrected data we have marked those data points we believe to be unreliable given the above discussion of the various effects introduced by the correction process by open symbols.

Taken at face value, it is apparent that the total rest-frame K -band LF does not evolve much out to $z = 1.2$. In each of our four redshift bins, the LF is consistent with no evolution with respect to the local one. This is in agreement with the finding of Cowie et al. (1996) from a much smaller spectroscopic sample, where the authors found that the K -band LF in the redshift bin $0.6 < z < 1$ was consistent with the one at $0 < z < 0.2$.

This is further demonstrated by the total K -band luminosity density shown in Fig. 5.11. Also here there is no clear sign of evolution with redshift within our sample.

Note that to compute the previous quantity, we have to assume something about the luminosity in objects at the faint end of the luminosity function which are beyond our magnitude limits. Since we have no handle on the slope of the faint end from our

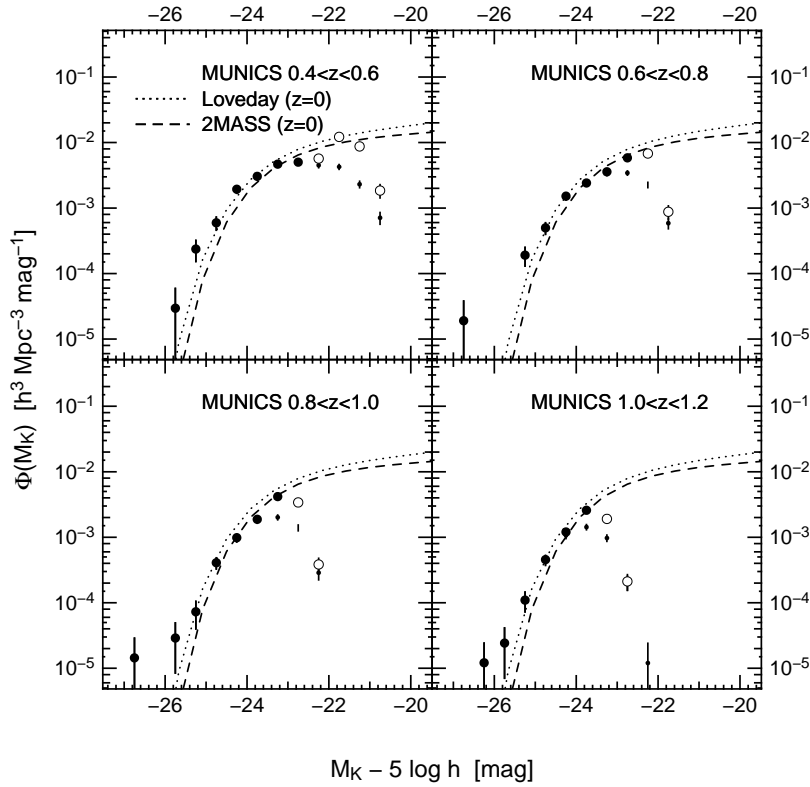


Figure 5.10: The final rest-frame K -band luminosity function from the MUNICS sample in four redshift bins, $0.4 < z < 0.6$, $0.6 < z < 0.8$, $0.8 < z < 1.0$, and $1.0 < z < 1.2$. The small filled symbols denote the uncorrected data, the large filled symbols show the final corrected data. The open symbols denote those ranges where we think that the correction is unreliable (see text). Error bars are Poisson errors on the number of objects in each bin. The dotted and dashed lines denote the local K -band LF published by Loveday (2000) and Kochanek et al. (2001), respectively.

data, assuming that the local slope of $\alpha = -1.09$ holds, we have computed the fraction of the total luminosity lost due to incompleteness:

$$C_{\Phi} = \frac{\int_{-\infty}^{M_{\text{lim}}} \Phi(M) dM}{\int_{-\infty}^{+\infty} \Phi(M) dM}. \quad (5.8)$$

This fraction was found to be always smaller than a factor of 2.

Our result is in marked contrast to the results obtained for the B -band LF in the same redshift range from the CFRS and CNOC surveys (Lilly et al., 1995b; Lin et al., 1999) which consistently find an increase in the B -band luminosity density driven mainly by late spectral types.

At least some of this increase is due to the “faint blue galaxies” population at (observer’s frame) $B \gtrsim 22$ mag which first appeared in faint blue number counts (see review by Ellis, 1997). For example, Cowie et al. (1996) found that at $B \approx 24$, the population of galaxies is a mixture of normal galaxies at modest redshifts and a popu-

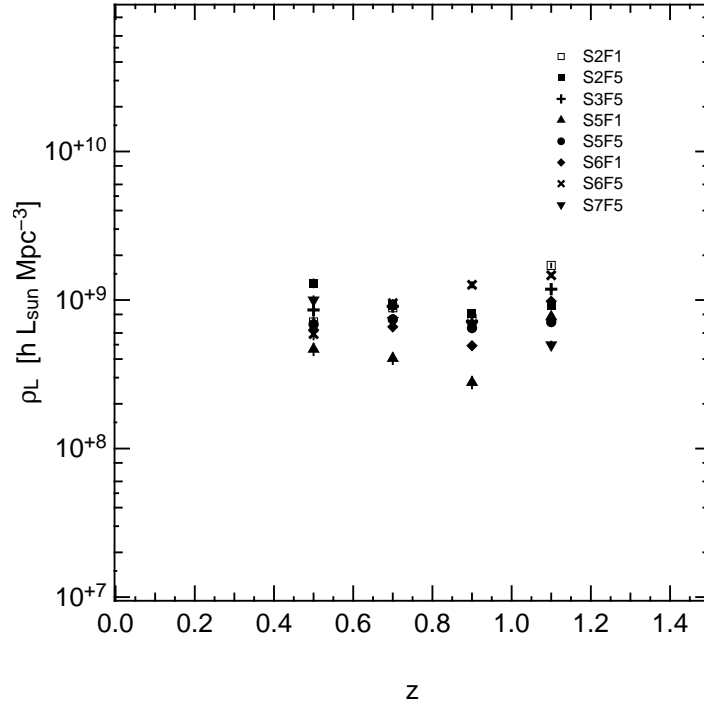


Figure 5.11: The rest-frame *K*-band luminosity density at $0.4 < z < 1.2$. Different symbols denote the different survey patches (Mosaic Fields). Redshift bins as for the luminosity function.

lation of galaxies with a wide range of masses undergoing rapid star formation which are spread out in redshift from $z = 0.2$ to at least $z = 1.7$.

The remaining part of the increase in blue luminosity is due to luminosity evolution of normal field spirals and early-type systems.

On the other hand, luminosity evolution is inevitable if the *K*-band light traces the underlying old stellar population of galaxies, since these stars inevitably become younger with look-back time.

For the *K* band, pure luminosity evolution predicts brightening by ~ 0.5 mag as the mass-to-light ratio evolves from the local value to ~ 0.65 at redshift ~ 1 (see the following chapter on the mass function).

Therefore, our conclusion must be that either number density evolution takes place, counterbalancing the luminosity evolution, or evolution in the stellar mass of individual objects on average drives the total *K*-band luminosity down to counterbalance the luminosity evolution. Even if the faint end of the LF changes significantly and thereby rendering the result on the total luminosity density invalid, the stated conclusion holds for $L \gtrsim L^*$ objects from the constancy of the luminosity function alone.

5.6.3 The rest-frame *K*-band luminosity function by spectral type

From spectroscopic follow-up observations of the Hawaii Deep Fields (Cowie et al., 1994), Cowie et al. (1996) constructed a nearly complete sample down to $K = 20$, $I =$

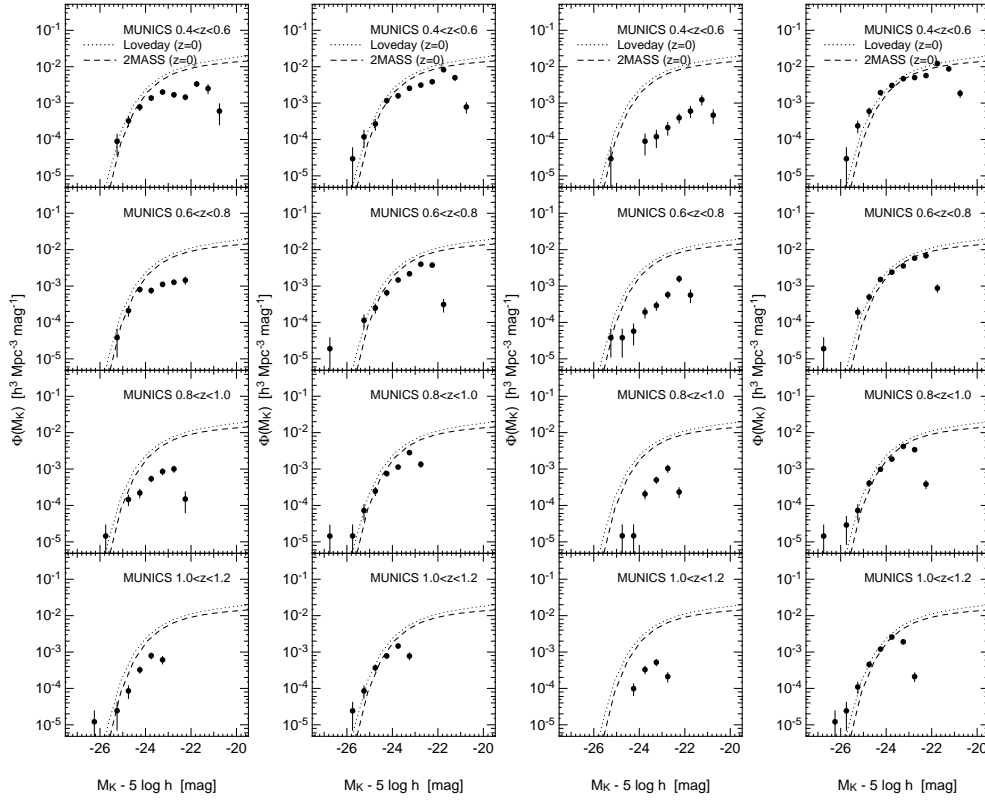


Figure 5.12: Comparison of the rest frame K -band luminosity function divided by spectral type (see text). The panels from left to right show the luminosity function for early, intermediate, late, and all types, respectively. Redshift increases from top to bottom. The dotted and dashed lines denote the local K -band LF published by Loveday (2000) and Kochanek et al. (2001), respectively and are shown for comparison in all panels.

22, and $B = 24.5$ mag containing 392 galaxies in total. Measures of the star formation rate ([OII] equivalent widths or rest-frame UV-IR colour information) in conjunction with rest-frame K -band luminosity were used to argue that the maximum rest-frame K luminosity of galaxies undergoing strong star-formation has been declining steadily with decreasing redshift from a value near L^* at $z \gtrsim 1$. In other words, more massive galaxies experience strong star formation at earlier cosmic time.

Verifying this most interesting result has been difficult so far due to the lack of suitable K -selected samples. The MUNICS sample lacks the appropriate measure of star-formation rate due to the incompleteness of the spectroscopic programme to date and due to the absence of rest-frame UV imaging, but we might try to use the colour information to divide the sample into rough spectral types and see if there is a correlation between colour and rest-frame K -luminosity.

Using interpolated rest-frame $B-V$ colours, we divided the sample into early-type objects ($B-V > 0.75$; E,S0), intermediate-type objects ($0.6 < B-V < 0.75$; Sa to Sb), and late-type objects ($B-V < 0.6$; later than Sbc). The Hubble classification according

to $B-V$ colour is following [Roberts & Haynes \(1994\)](#). This classification is, of course, only indicative. We have convinced ourselves that the results presented below are not sensitive on the exact choice of colour subdivisions.

The LF of these subdivisions are shown in [Fig. 5.12](#). The bright end is populated by early and intermediate-type objects at all redshifts. At luminosities around L^* the LF is dominated by intermediate type objects, as it is also true locally. Both early and intermediate-type objects do not show clear signs of evolution with redshifts in our sample. At the bright end, there might be a decrease in numbers in the early-type population, but as those objects are dominated by de Vaucouleurs profiles, this might well be due the bias against these profiles in the detection probability, as pointed out in [Sect. 4.5.4](#).

The late-types, though, show a trend with redshift, in the sense that there are more *K*-band bright objects of blue colour at high redshift compared to the lowest redshift bin. One gains the impression that the LF of these late types steepens with redshift, such that blue objects of higher *K*-band luminosity appear at higher redshifts, but this trend is indicative at most, as the LF of the late-type objects is noisy, due to their relative paucity in the *K*-selected sample.

If this trend is real, it implies that the stellar mass of galaxies correlates with their formation epoch such that galaxies of higher mass formed the bulk of their stars at earlier cosmic times. This is most interesting since it places a constraint on galaxy formation models, which rather predict later assembly of massive galaxies. Newer models seem to be able to reproduce this observed trend, as the oldest stars are found in the deepest potential wells in the current generation of models ([White 2001](#), priv. comm.)

Clearly, a large *K*-selected spectroscopic sample is needed to assess this matter quantitatively, providing both a measure for the stellar mass and a measurement of the star-formation rate and dust extinction.

Chapter 6

The mass function of field galaxies

In the following chapter we discuss the integrated mass function of field galaxies and its evolution over the redshift range $0.4 < z < 1.2$. We use two approaches to model the mass-to-light ratio of galaxies, presented in Sect. 6.2 and Sect. 6.3 and compare the results obtained in Sect. 6.4.

6.1 Introduction

The traditional observables used to characterise galaxies are unsuitable for studying the assembly history of galaxies, one of the most fundamental predictions of CDM models, since these observables may be transient. The best observable for this aim is, in principle, total mass, which is on the other hand very hard to measure. It has been argued that the best available surrogate accessible to direct observation is the near-IR K -band luminosity of a galaxy which reflects the mass of the underlying stellar population and is least sensitive to bursts of star formation and dust extinction (Rix & Rieke, 1993; Kauffmann & Charlot, 1998; Brinchmann & Ellis, 2000). The main uncertainty involved in the conversion of K -band light to mass is due to the age of the population, amounting to only a factor of two in mass uncertainty for populations older than ~ 3 Gyr.

Here we use the K -band selected field galaxy sample of MUNICS to study the number density evolution of massive galaxies. Data discussed here refer to ~ 5000 galaxies for which high quality VRIJK imaging covering 0.27 square degrees is available. The distances of the galaxies are derived from spectroscopically calibrated photometric redshifts. The sample is identical to the one used to construct the luminosity function in Chapter 5.

We derive stellar masses by converting rest-frame K -band luminosities to mass using two different approaches to model the mass-to-light ratios of the galaxies. We discuss the resulting integrated stellar mass functions at different mass limits and their evolution with redshift.

Again, we assume $\Omega_M = 0.3$, $\Omega_\Lambda = 0.7$ throughout this chapter. We write Hubble's Constant as $H_0 = 100 h \text{ km s}^{-1} \text{ Mpc}^{-1}$, using $h = 0.65$ unless the quantities in question can be written in a form explicitly depending on h .

6.2 The maximum PLE model

The integrated stellar mass function $n(\mathcal{M} > \mathcal{M}_{\text{lim}})$, the comoving number density of objects having stellar mass exceeding \mathcal{M}_{lim} , is computed using the V_{max} formalism and a per-object detection incompleteness correction in analogy to the calculation of the luminosity function in Sect. 5.5.

To compute the stellar mass of a galaxy, we first use an approach which maximises the stellar mass for any K -band luminosity at any redshift.

Noting that \mathcal{M}/L_K is a monotonically rising function of age for Simple Stellar Populations (SSPs), we find that the likely upper limit for \mathcal{M}/L_K is the mass-to-light ratio of a SSP which is as old as the universe at the galaxy's redshift. This is the most extreme case of passive luminosity evolution (PLE) one can adopt. It corresponds to a situation where all massive galaxies would be of either elliptical, S0, or Sa type.

We take the mass-to-light ratios from the SSP models published by Maraston (1998), using a Salpeter IMF. Similar dependencies on age are obtained from the models of Worthey (1994) and Bruzual & Charlot (1993) although the absolute values of \mathcal{M}/L_K vary somewhat, partly due to differences in the models themselves but mostly due to the way stellar remnants are treated by the different authors.

The \mathcal{M}/L_K which we obtain with our cosmological parameters at $z \sim 0.5$ are approximately consistent with \mathcal{M}/L_K of local galaxies (Bell & de Jong, 2001).

The mass of each object in solar units is consequently given by

$$\mathcal{M} = \left(\frac{\mathcal{M}}{L_K} \right) 10^{-0.4(M_K - M_{\odot,K})}, \quad (6.1)$$

using $M_{\odot,K} = 3.33$.

The number density in each redshift bin, $n(\mathcal{M} > \mathcal{M}_{\text{lim}}, z)$, is finally computed by summing over all galaxies in the bin whose stellar mass is exceeding \mathcal{M}_{lim} ,

$$n(\mathcal{M} > \mathcal{M}_{\text{lim}}, z) = \sum_i \frac{1}{V_{\text{max}}^i} \frac{1}{P(m_{K,i})} \quad (6.2)$$

The resulting integrated mass functions for $\mathcal{M}_{\text{lim}} = 2 \times 10^{10} h^{-2} \mathcal{M}_{\odot}$, $\mathcal{M}_{\text{lim}} = 5 \times 10^{10} h^{-2} \mathcal{M}_{\odot}$, and $\mathcal{M}_{\text{lim}} = 1 \times 10^{11} h^{-2} \mathcal{M}_{\odot}$ are shown in Fig. 6.1 along with the integrated luminosity functions for comparison.

The mean values of \mathcal{M}/L_K in the maximum PLE model in the four redshift bins are 0.99, 0.83, 0.73, and 0.65, as computed from the look-back time in our cosmology. With these mean values the mass limits correspond to absolute K -band magnitudes of -22.43 , -22.63 , -22.77 , and -22.90 , respectively, for $\mathcal{M}_{\text{lim}} = 2 \times 10^{10} h^{-2} \mathcal{M}_{\odot}$. For $\mathcal{M}_{\text{lim}} = 5 \times 10^{10} h^{-2} \mathcal{M}_{\odot}$ the numbers are -23.42 , -23.62 , -23.76 , and -23.89 . Finally, for $\mathcal{M}_{\text{lim}} = 1 \times 10^{11} h^{-2} \mathcal{M}_{\odot}$ we have -24.18 , -24.38 , -24.51 , and -24.64 (magnitudes with respect to $h = 1$).

Fig. 6.1 compares the evolution of the integrated luminosity to the integrated mass. It is evident that the number density of *luminous* K -band selected galaxies does not evolve significantly (given our uncertainties) to $z = 1.2$. However, because of the inevitable evolution of the mass-to-light ratio with z , the number density of

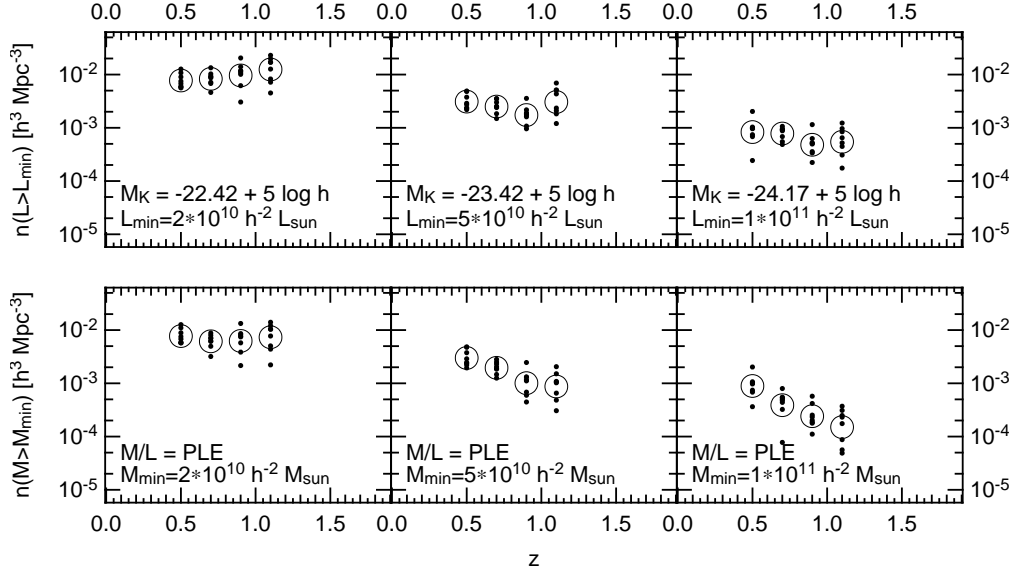


Figure 6.1: Comoving number density of objects having rest-frame K -band luminosities exceeding $-22.42 + 5 \log h$ ($2 \times 10^{10} h^{-2} L_{\odot}$), $-23.42 + 5 \log h$ ($2 \times 10^{10} h^{-2} L_{\odot}$), and $-24.17 + 5 \log h$ ($2 \times 10^{10} h^{-2} L_{\odot}$) (upper panels) and comoving number density of objects having stellar masses exceeding $\mathcal{M}_{\text{lim}} = 2 \times 10^{10} h^{-2} \mathcal{M}_{\odot}$, $\mathcal{M}_{\text{lim}} = 5 \times 10^{10} h^{-2} \mathcal{M}_{\odot}$, and $\mathcal{M}_{\text{lim}} = 1 \times 10^{11} h^{-2} \mathcal{M}_{\odot}$ (integrated stellar mass functions; lower panels). Mass to light ratios are assigned to maximise the stellar mass at a given luminosity (see text), and thus are likely upper limits. The solid points denote the values measured separately in each survey field, the open circles denote the mean values over the whole survey area. The size of the open circles is chosen to represent our estimate of the total uncertainty in the mean values.

massive systems does change. Transforming luminosities into masses with our maximum PLE scheme yields a roughly constant number density for our lowest mass limit, $2 \times 10^{10} h^{-2} \mathcal{M}_{\odot}$, and a decrease of the number density with redshift by a factor of ~ 3 for a mass limit of $5 \times 10^{10} h^{-2} \mathcal{M}_{\odot}$, and by a factor ~ 6 for objects more massive than $1 \times 10^{11} h^{-2} \mathcal{M}_{\odot}$. As the true \mathcal{M}/L_K at high redshift will most likely be lower than in our maximum PLE model, the true number densities are likely to decrease more rapidly with redshift.

The steepening of the curves with increasing limiting mass in the maximum PLE curves (despite them all having the same mass-to-light ratios at any given redshift) is due to the invariance of the LF with redshift and its steepness at the bright end. At increasing limiting mass, one is moving down the steepening bright end of the LF, so that the same change in the mass-to-light ratio yields a higher change in the number density.

To investigate the effect the uncertainties in the photometric redshifts have on the values of the integrated mass function, we have performed Monte-Carlo simulations as described in Sect. 5.5.2. The errors of the mean values of the integrated mass function (size of open symbols in Fig. 6.1) are derived by repeating the mass function analysis

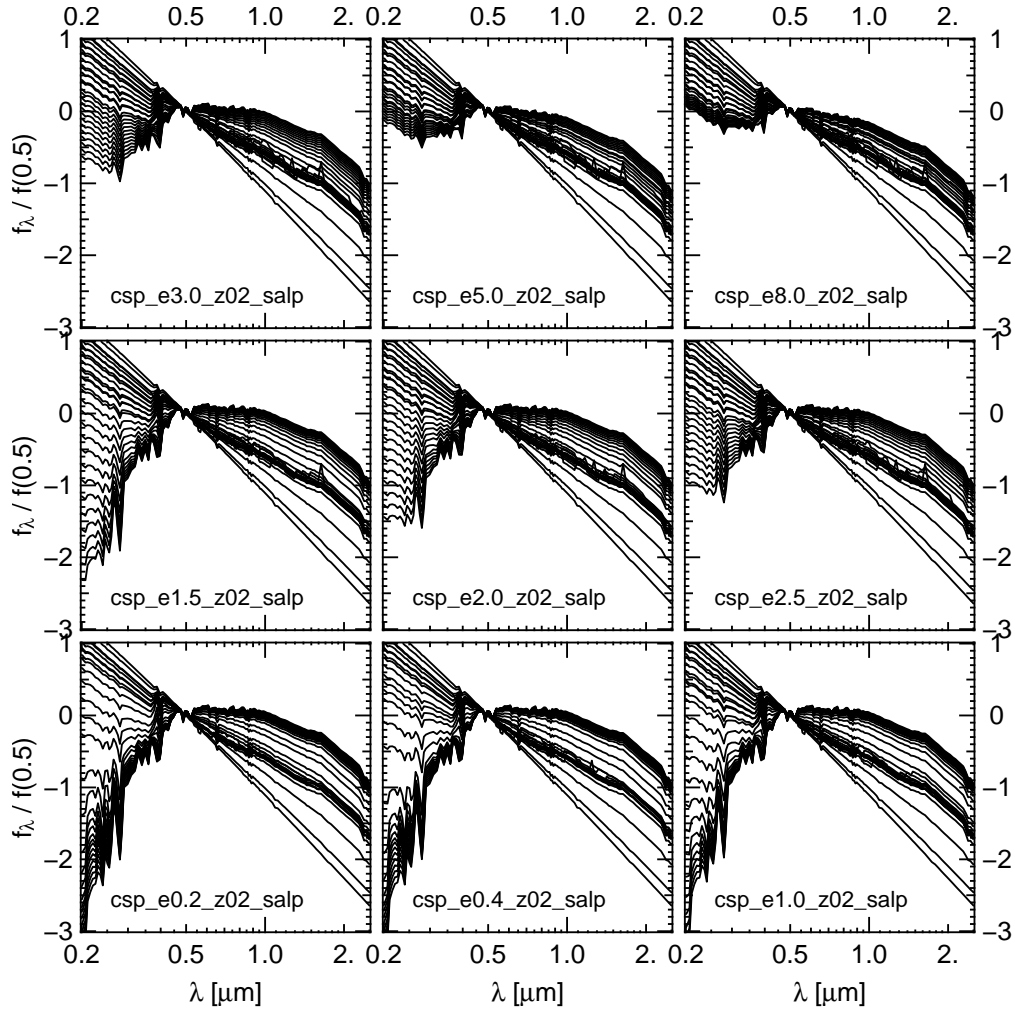


Figure 6.2: Grid of CSP models with exponentially declining star formation rates, τ , ranging from 0.2 Gyr (bottom left) to 8 Gyr (top right). Each panel shows the spectra of one model extracted at 28 ages, t , between 0.04 Gyr and 15 Gyr. The flux is normalised at 5000\AA .

using subsamples of the template SED library, as deficiencies in the templates are the main source of concern for the accuracy of the redshifts during the photometric redshift determination.

6.3 The fitted mass-to-light-ratio model

To obtain a more realistic estimate of \mathcal{M}/L_K , we used our VRIJK color information and the photometric redshift to fit the age and SFR of each galaxy using a grid of composite stellar populations (CSP) with 9 exponential star formation timescales, τ , ranging from 0.2 to 8 Gyr with spectra extracted for 28 ages, t , between 0.04 Gyr and 15 Gyr for each τ . The input SSPs for constructing the composite stellar populations

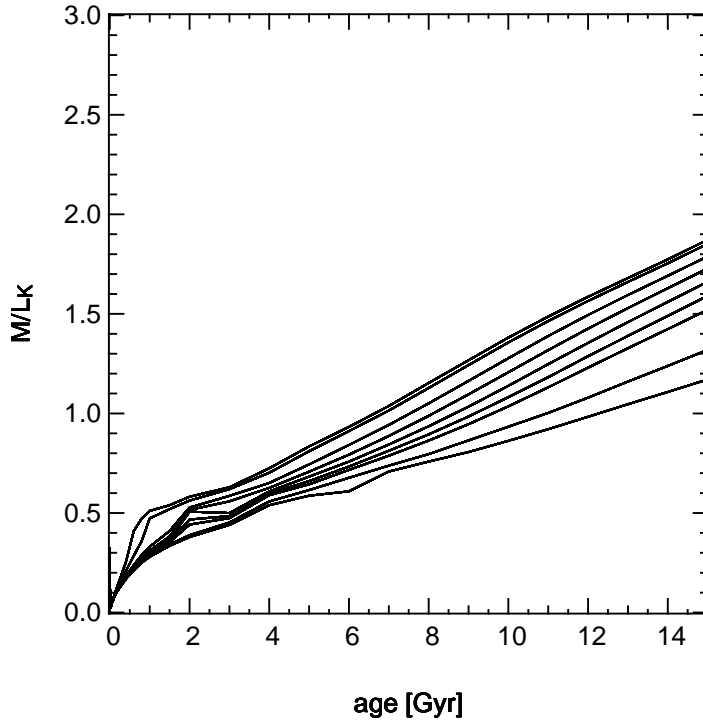


Figure 6.3: Evolution of the K -band mass-to-light ratio, \mathcal{M}/L_K , with age for different star formation histories (see text). The models are exponential declines in the SFR and span the range $0.2\text{Gyr} \leq \tau \leq 8\text{Gyr}$

models are taken from [Maraston \(2002\)](#), again using Salpeter IMF. The model grid is shown in [Fig. 6.2](#)

[Fig. 6.3](#) shows the evolution of the K -band mass-to-light ratios as a function of age for each value of τ in the grid. Except for the two largest values of τ , the slope at ages $t \gtrsim 2\text{Gyr}$ is remarkably independent of the actual star formation timescale. Moreover, the slope of the time evolution of \mathcal{M}/L_K is the same even for the shortest value of τ , 0.2 Gyr, which essentially represents an SSP. Let aside normalisation effects, we therefore may expect a similar result for the mass function as obtained with the PLE model.

To assign each object a pair of values (τ, t) , a likelihood analogous to [Eq. 5.3](#) is computed at each grid point (τ, t) , after accounting for the bandwidth shift due to the redshift of the object. We restricted the model grid for each object such that a model cannot be chosen if it represents an object older than the universe at the particular redshift.

The average K -band mass-to-light ratio of the galaxy population determined by applying this fitting procedure is shown in [Fig. 6.4](#). The figure also shows the PLE mass-to-light ratio as a function of z . Apart from the different normalisation, the evolution with redshift is very similar, a consequence of the insensitivity of \mathcal{M}/L_K on the star formation history.

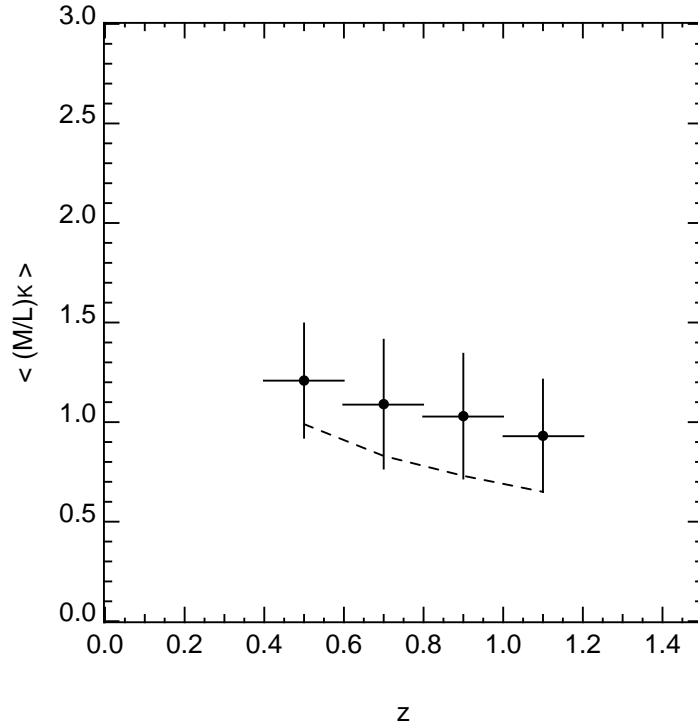


Figure 6.4: The average K -band mass-to-light ratio, \mathcal{M}/L_K , of the MUNICS sample as a function of redshift as determined from fitting composite stellar population models to the V, R, I, J, K colour data base. Vertical errorbars denote the width of the \mathcal{M}/L_K distribution in each redshift bin. The dashed line denotes the mass-to-light ratio of the maximum PLE model (see text).

Finally, Fig.6.5 shows the integrated mass function for the same mass limits as those applied above, using the individually fitted \mathcal{M}/L_K values.

6.4 Discussion

The most striking feature of Fig. 6.5 is the similarity of the maximum PLE and the CSP-fitted curves. Note that there is a difference in the normalisation of the two, and due to the logarithmic scaling of the figure, the slope appears to be different in the plot.

If star formation played an important role at $z \sim 1$, the presence of young populations would have pushed \mathcal{M}/L_K down, and therefore the CSP-fitted curves would be expected to be steeper than the maximum PLE curve, which assumes no star formation happens at all after $z = \infty$.

Nevertheless, the number density of massive systems seems to decline, with this decline being stronger for more massive systems, and therefore one is inclined to think that merging does play an important role. Indeed, Le Fèvre et al. (2000b) derive a number of 0.6 to 1.8 major mergers per L^* galaxy since $z \sim 1$ from HST-based pair counts of galaxies with known redshifts selected from the CFRS. We observe a decline

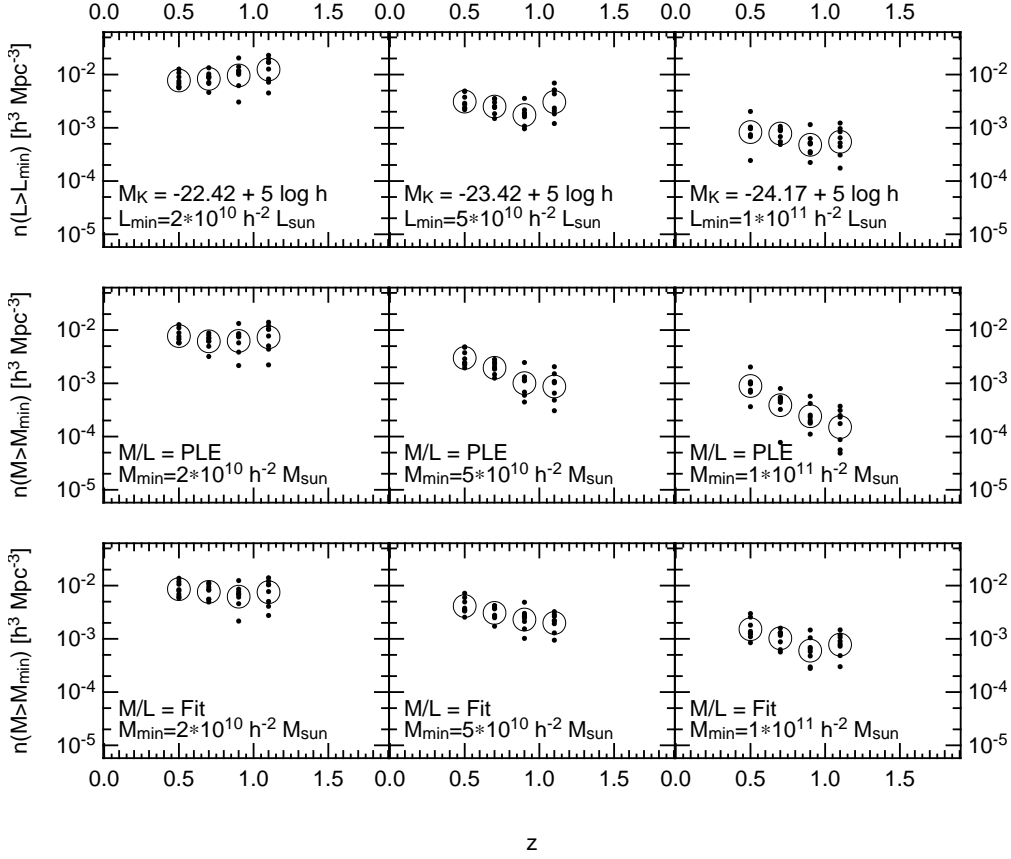


Figure 6.5: Upper and middle panels as in Fig. 6.1. The lower panel shows the integrated mass function for the same mass limits, this time individually determining \mathcal{M}/L_K for each object by fitting against a grid of CSP models (see text). The solid points denote the values measured separately in each survey field, the open circles denote the mean values over the whole survey area. The size of the open circles is chosen to represent our estimate of the total uncertainty in the mean values.

in the number density by a factor of $\gtrsim 2$ for somewhat more massive systems, and almost no significant density evolution at L^* .

Therefore, we are inclined to think that if merging is the dominant factor in increasing the mass of these K -selected massive galaxies, most of the merging has to be dissipationless, involving rather low star formation activity.

The main uncertainty in these conclusions is still the field to field variation, in spite of the relatively large area surveyed, followed by the choice of SED templates used in the photometric redshift code (see above). The size of the open symbols in Fig. 6.1 represents our estimate of the total uncertainty of the mean values. If we assume a Gould IMF (Gould et al., 1998) instead of a Salpeter IMF, the evolving \mathcal{M}/L_K curve becomes lower in its normalization as the mass-to-light ratio becomes smaller due to the reduced number of low-mass stars. The slope does not change significantly.

The observed density evolution as a function of mass is qualitatively consistent

with the expectation from hierarchical galaxy formation models. Most rapid evolution is predicted for the number density of the most massive galaxies while the number density of L^* -galaxies should evolve much less. E.g. Baugh et al. (1998) predict that the number density of galaxies of a stellar mass of $10^{10}h^{-1}M_{\odot}$ decreases by a factor of ~ 3.1 over redshift range $0.4 < z < 1.2$ (for the cosmological parameters as used here). Though this agreement is encouraging, both more elaborated models and improved sets of data are required. The latter can be obtained by larger and deeper samples, and more realistic estimates of \mathcal{M}/L_K based on spectroscopic observations of the galaxies.

Bibliography

- Aragòn-Salamanca, A., Baugh, C. M., & Kauffmann, G. 1998, MNRAS, 297, 427 [19](#)
- Arnouts, S., D'Odorico, S., Cristiani, S., Zaggia, S., Fontana, A., & Giallongo, E. 1999, A&A, 341, 641 [71](#)
- Bahcall, N. A., & Fan, X. 1998, ApJ, 504, 1 [18](#)
- Bahcall, N. A., Fan, X., & Cen, R. 1997, ApJ, 485, L53 [18](#)
- Baugh, C. M., Cole, S., & Frenk, C. S. 1996, MNRAS, 283, 1361 [19](#), [81](#)
- Baugh, C. M., Cole, S., Frenk, C. S., & Lacey, C. G. 1998, ApJ, 498, 504 [100](#)
- Baum, W. A. 1962, in IAU Symp. 15: Problems of Extra-Galactic Research, Vol. 15, 390 [15](#)
- Bazell, D., & Peng, Y. 1998, ApJS, 116, 47 [39](#)
- Beard, S. M., MacGillivray, H. T., & Thanisch, P. F. 1990, MNRAS, 247, 311 [33](#)
- Bell, E. F., & de Jong, R. S. 2001, ApJ, 550, 212 [94](#)
- Bender, R., et al. 2001, in ESO/ECF/STScI Workshop on Deep Fields, ed. S. Cristiani (Berlin: Springer), 327 [75](#)
- Bender, R., Burstein, D., & Faber, S. M. 1992, ApJ, 399, 462 [4](#)
- Bender, R., Ziegler, B., & Bruzual, G. 1996, ApJ, 463, L51 [4](#), [81](#)
- Benítez, N. 2000, ApJ, 536, 571 [16](#), [75](#)
- Bernardi, M., Renzini, A., da Costa, L. N., Wegner, G., Alonso, M. V., Pellegrini, P. S., Rité, C., & Willmer, C. N. A. 1998, ApJ, 508, L143 [81](#)
- Bertin, E. 1994, Ap&SS, 217, 49 [39](#)
- Bertin, E., & Arnouts, S. 1996, A&AS, 117, 393 [33](#), [35](#), [39](#)
- Bertin, E., & Dennefeld, M. 1997, A&A, 317, 43 [71](#)
- Bizenberger, P., McCaughrean, M. J., Birk, C., Thompson, D., & Storz, C. 1998, Proceedings of SPIE, 3354, 825 [25](#)

- Brinchmann, J., et al. 1998, ApJ, 499, 112 7
- Brinchmann, J., & Ellis, R. S. 2000, ApJ, 536, L77 vii, 16, 19, 93
- Broadhurst, T. J., Ellis, R. S., & Shanks, T. 1988, MNRAS, 235, 827 vii, 15
- Bromley, B. C., Press, W. H., Lin, H., & Kirshner, R. P. 1998, ApJ, 505, 25 73
- Bruzual, G. A., & Charlot, S. 1993, ApJ, 405, 538 20, 94
- Burkey, J. M., Keel, W. C., Windhorst, R. A., & Franklin, B. E. 1994, ApJ, 429, L13 9
- Burstein, D., Bender, R., Faber, S., & Nolthenius, R. 1997, AJ, 114, 1365 50, 51
- Carlberg, R. G., Cowie, L. L., Songaila, A., & Hu, E. M. 1997, ApJ, 484, 538 8
- Carlberg, R. G., Pritchett, C. J., & Infante, L. 1994, ApJ, 435, 540 9
- Carlberg, R. G., Yee, H. K. C., Morris, S. L., Lin, H., Hall, P. B., Patton, D., Sawicki, M., & Shepherd, C. W. 2000, ApJ, 542, 57 9
- Casali, M. M., & Hawarden, T. 1992, JCMT UKIRT Newsletter, 4, 33 25
- Casertano, S., et al. 2000, AJ, 120, 2747 1
- Casertano, S., Ratnatunga, K. U., Griffiths, R. E., Im, M., Neuschaefer, L. W., Ostrander, E. J., & Windhorst, R. A. 1995, ApJ, 453, 599 71
- Chapman, S. C., McCarthy, P. J., & Persson, S. E. 2000, AJ, 120, 1612 2
- Charlot, S., Ferrari, F., Mathews, G. J., & Silk, J. 1993, ApJ, 419, L57 4
- Christian, C. A., Adams, M., Barnes, J. V., Butcher, H., Hayes, D. S., Mould, J. R., & Siegel, M. 1985, PASP, 97, 363 30
- Cimatti, A., et al. 1999, A&A, 352, L45 3, 19
- Cimatti, A., Villani, D., Pozzetti, L., & di Serego Alighieri, S. 2000, MNRAS, 318, 453 2
- Cole, S., Lacey, C. G., Baugh, C. M., & Frenk, C. S. 2000, MNRAS, 319, 168 11, 12, 19, 81
- Colless, M., Ellis, R. S., Taylor, K., & Hook, R. N. 1990, MNRAS, 244, 408 vii, 15
- Couch, W. J., Jurcevic, J. S., & Boyle, B. J. 1993, MNRAS, 260, 241 71
- Couch, W. J., & Newell, E. B. 1984, ApJS, 56, 143 71
- Cowie, L. L., Gardner, J. P., Hu, E. M., Songaila, A., Hodapp, K.-W., & Wainscoat, R. J. 1994, ApJ, 434, 114 vii, 15, 16, 17, 71, 90

- Cowie, L. L., Songaila, A., & Barger, A. J. 1999, *AJ*, 118, 603 6
- Cowie, L. L., Songaila, A., Hu, E. M., & Cohen, J. G. 1996, *AJ*, 112, 839 8, 82, 88, 89, 90
- Daddi, E., Cimatti, A., Pozzetti, L., Hoekstra, H., Röttgering, H. J. A., Renzini, A., Zamorani, G., & Mannucci, F. 2000, *A&A*, 361, 535 3
- Daddi, E., Cimatti, A., & Renzini, A. 2000, *A&A*, 362, L45 2
- Dalcanton, J. J. 1998, *ApJ*, 495, 251 50
- de Propriis, R., Stanford, S. A., Eisenhardt, P. R., Dickinson, M., & Elston, R. 1999, *AJ*, 118, 719 3, 18
- de Vaucouleurs, G. 1948, *Annales d'Astrophysique*, 11, 247 51
- Disney, M., & Phillipps, S. 1983, *MNRAS*, 205, 1253 56, 57
- Djorgovski, S., & Davis, M. 1987, *ApJ*, 313, 59 4
- Djorgovski, S., et al. 1995, *ApJ*, 438, 1 17, 71
- Driver, S. P., Phillipps, S., Davies, J. I., Morgan, I., & Disney, M. J. 1994, *MNRAS*, 266, 155 71
- Driver, S. P., Windhorst, R. A., & Griffiths, R. E. 1995, *ApJ*, 453, 48 7
- Eke, V. R., Cole, S., & Frenk, C. S. 1996, *MNRAS*, 282, 263 18
- Eke, V. R., Cole, S., Frenk, C. S., & Patrick Henry, J. 1998, *MNRAS*, 298, 1145 18
- Ellis, R. S. 1997, *ARA&A*, 35, 389 7, 89
- Ellis, R. S., Colless, M., Broadhurst, T., Heyl, J., & Glazebrook, K. 1996, *MNRAS*, 280, 235 2
- Elston, R., Rieke, G. H., & Rieke, M. J. 1988, *ApJ*, 331, L77 19
- Ferguson, H. C., Dickinson, M., & Williams, R. 2000, *ARA&A*, 38, 667 1, 7
- Fernández-Soto, A., Lanzetta, K. M., & Yahil, A. 1999, *ApJ*, 513, 34 16
- Feulner, G. 2000, Diploma thesis, Ludwig-Maximilians-Universität, München 30, 69
- Feulner, G. 2002, Ph.D. thesis, Ludwig-Maximilians-Universität, München 31
- Flores, H., et al. 1999, *ApJ*, 517, 148 6
- Folkes, S., et al. 1999, *MNRAS*, 308, 459 73
- Fontana, A., Menci, N., D'Odorico, S., Giallongo, E., Poli, F., Cristiani, S., Moorwood, A., & Saracco, P. 1999, *MNRAS*, 310, L27 82

- Freeman, K. C. 1970, *ApJ*, 160, 811 50
- Gardner, J. P., Cowie, L. L., & Wainscoat, R. J. 1993, *ApJ*, 415, L9 16, 69
- Gardner, J. P., Sharples, R. M., Carrasco, B. E., & Frenk, C. S. 1996, *MNRAS*, 282, L1 71
- Gardner, J. P., Sharples, R. M., Frenk, C. S., & Carrasco, B. E. 1997, *ApJ*, 480, L99 17
- Gavazzi, G., Franzetti, P., Scodreggio, M., Boselli, A., & Pierini, D. 2000, *A&A*, 361, 863 52, 53
- Giavalisco, M., Livio, M., Bohlin, R. C., Macchetto, F. D., & Stecher, T. P. 1996, *AJ*, 112, 369 10
- Giavalisco, M., Steidel, C. C., Adelberger, K. L., Dickinson, M. E., Pettini, M., & Kellogg, M. 1998, *ApJ*, 503, 543 10
- Glazebrook, K., Ellis, R., Santiago, B., & Griffiths, R. 1995, *MNRAS*, 275, L19 7
- Glazebrook, K., Peacock, J. A., Collins, C. A., & Miller, L. 1994, *MNRAS*, 266, 65 vii, 15, 17, 71
- Gössl, C. A., Riffeser, A., & Fliri, J. 2000, *A&A*, in preparation 29
- Gould, A., Flynn, C., & Bahcall, J. N. 1998, *ApJ*, 503, 798 99
- Griffiths, R. E., et al. 1994, *ApJ*, 437, 67 3
- Groth, E. J., A., K. J., R., L., J., O. R., R., B., & J., R. 1994, *BAAS*, 26, 1403 3
- Gunn, J. E., & Stryker, L. L. 1983, *ApJS*, 52, 121 23
- Haarsma, D. B., Partridge, R. B., Windhorst, R. A., & Richards, E. A. 2000, *ApJ*, 544, 641 6
- Hall, P., & Mackay, C. D. 1984, *MNRAS*, 210, 979 71
- Hammer, F., et al. 1997, *ApJ*, 481, 49 6
- Harris, W. E. 1990, *PASP*, 102, 949 35
- Heyl, J., Colless, M., Ellis, R. S., & Broadhurst, T. 1997, *MNRAS*, 285, 613 2, 73
- Hogg, D. W. 2001, *ApJ*, submitted 6
- Hogg, D. W., Cohen, J. G., Blandford, R., & Pahre, M. A. 1998, *ApJ*, 504, 622 6
- Hogg, D. W., Pahre, M. A., McCarthy, J. K., Cohen, J. G., Blandford, R., Smail, I., & Soifer, B. T. 1997, *MNRAS*, 288, 404 71
- Hu, E. M., & Ridgway, S. E. 1994, *AJ*, 107, 1303 2, 19

- Huang, J., Cowie, L. L., & Luppino, G. A. 1998, *ApJ*, 496, 31–71
- Hughes, D. H., et al. 1998, *Nature*, 394, 241–6
- Hunt, L. K., Mannucci, F., Testi, L., Migliorini, S., Stanga, R. M., Baffa, C., Lisi, F., & Vanzì, L. 1998, *AJ*, 115, 2594–25
- Im, M., Griffiths, R. E., Ratnatunga, K. U., & Sarajedini, V. L. 1996, *ApJ*, 461, L79–3
- Infante, L., Pritchett, C., & Quintana, H. 1986, *AJ*, 91, 217–71
- Irwin, M. J. 1985, *MNRAS*, 214, 575–35
- Jarvis, J. F., & Tyson, J. A. 1981, *AJ*, 86, 476–33, 35
- Jones, L. R., Fong, R., Shanks, T., Ellis, R. S., & Peterson, B. A. 1991, *MNRAS*, 249, 481–71
- Kauffmann, G., & Charlot, S. 1998, *MNRAS*, 297, L23–vii, 16, 17, 19, 81, 82, 83, 93
- Kauffmann, G., Charlot, S., & White, S. D. M. 1996, *MNRAS*, 283, L117–2
- Kauffmann, G., White, S. D. M., & Guiderdoni, B. 1993, *MNRAS*, 264, 201–11, 81
- Kelson, D. D., Illingworth, G. D., Franx, M., & van Dokkum, P. G. 2001, *ApJ*, 552, L17–4
- Kelson, D. D., Illingworth, G. D., van Dokkum, P. G., & Franx, M. 2000, *ApJ*, 531, 184–4
- Kelson, D. D., van Dokkum, P. G., Franx, M., Illingworth, G. D., & Fabricant, D. 1997, *ApJ*, 478, L13–4
- Kochanek, C. S., et al. 2001, *ApJ*, submitted–73, 86, 87, 88, 89, 91
- Koo, D. C. 1985, *AJ*, 90, 418–16
- Koo, D. C. 1986, *ApJ*, 311, 651–71
- Kormendy, J. 1985, *ApJ*, 295, 73–51
- Kron, R. G. 1980, *ApJS*, 43, 305–33, 35, 39
- Landolt, A. U. 1992, *AJ*, 104, 340–30
- Le Fèvre, O., et al. 2000a, *MNRAS*, 311, 565–9
- Le Fèvre, O., et al. 2000b, *MNRAS*, 311, 565–98
- Le Fèvre, O., Hudon, D., Lilly, S. J., Crampton, D., Hammer, F., & Tresse, L. 1996, *ApJ*, 461, 534–8
- Lilly, S., et al. 1998, *ApJ*, 500, 75–7

- Lilly, S. J., Cowie, L. L., & Gardner, J. P. 1991, *ApJ*, 369, 79 [vii](#), [15](#), [71](#)
- Lilly, S. J., Le Fèvre, O., Crampton, D., Hammer, F., & Tresse, L. 1995a, *ApJ*, 455, 50 [vii](#), [2](#), [15](#)
- Lilly, S. J., Le Fèvre, O., Hammer, F., & Crampton, D. 1996, *ApJ*, 460, L1 [6](#)
- Lilly, S. J., Tresse, L., Hammer, F., Crampton, D., & Le Fèvre, O. 1995b, *ApJ*, 455, 108 [2](#), [20](#), [73](#), [89](#)
- Lin, H., Yee, H. K. C., Carlberg, R. G., & Ellingson, E. 1997, *ApJ*, 475, 494 [73](#)
- Lin, H., Yee, H. K. C., Carlberg, R. G., Morris, S. L., Sawicki, M., Patton, D. R., Wirth, G., & Shepherd, C. W. 1999, *ApJ*, 518, 533 [2](#), [9](#), [73](#), [89](#)
- Liu, C. T., Green, R. F., Hall, P. B., & Osmer, P. S. 1998, *AJ*, 116, 1082 [73](#)
- Liu, M. C., Dey, A., Graham, J. R., Bundy, K. A., Steidel, C. C., Adelberger, K., & Dickinson, M. E. 2000, *AJ*, 119, 2556 [2](#)
- Loveday, J. 2000, *MNRAS*, 312, 557 [52](#), [87](#), [88](#), [89](#), [91](#)
- Lowenthal, J. D., et al. 1997, *ApJ*, 481, 673 [10](#)
- Madau, P., Ferguson, H. C., Dickinson, M. E., Giavalisco, M., Steidel, C. C., & Fruchter, A. 1996, *MNRAS*, 283, 1388 [6](#)
- Madau, P., Pozzetti, L., & Dickinson, M. 1998, *ApJ*, 498, 106 [7](#)
- Maddox, S. J., Efsthathiou, G., Sutherland, W. J., & Loveday, J. 1990, *MNRAS*, 243, 692 [33](#), [39](#)
- Maraston, C. 1998, *MNRAS*, 300, 872 [20](#), [75](#), [94](#)
- Maraston, C. 2002, *MNRAS*, submitted [97](#)
- Martini, P. 2001, *AJ*, 121, 2301 [2](#)
- Marzke, R. O., Huchra, J. P., & Geller, M. J. 1994, *ApJ*, 428, 43 [73](#)
- McLeod, B. A., Bernstein, G. M., Rieke, M. J., Tollestrup, E. V., & Fazio, G. G. 1995, *ApJS*, 96, 117 [17](#)
- Menanteau, F., Ellis, R. S., Abraham, R. G., Barger, A. J., & Cowie, L. L. 1999, *MNRAS*, 309, 208 [3](#)
- Metcalfé, N., Fong, R., & Shanks, T. 1995, *MNRAS*, 274, 769 [71](#)
- Metcalfé, N., Shanks, T., Campos, A., Fong, R., & Gardner, J. P. 1996, *Nature*, 383, 236 [71](#)
- Metcalfé, N., Shanks, T., Campos, A., McCracken, H. J., & Fong, R. 2000, *MNRAS*, in press [71](#)

- Metcalf, N., Shanks, T., Fong, R., & Jones, L. R. 1991, MNRAS, 249, 498 71
- Metcalf, N., Shanks, T., Fong, R., & Roche, N. 1995, MNRAS, 273, 257 71
- Mobasher, B., Cram, L., Georgakakis, A., & Hopkins, A. 1999, MNRAS, 308, 45 6
- Mobasher, B., Sharples, R. M., & Ellis, R. S. 1993, MNRAS, 263, 560 17
- Moffat, A. F. J. 1969, A&A, 3, 455 51
- Monet, D., et al. 1996, "USNO-SA1.0" (U.S. Naval Observatory, Washington DC, 1996.) 30
- Moorwood, A. F. M., van der Werf, P. P., Cuby, J. G., & Oliva, E. 2000, A&A, 362, 9 6
- Moriondo, G., Cimatti, A., & Daddi, E. 2000, A&A, 364, 26 3
- Neuschaefer, L., Ratnatunga, K. U., Griffiths, R. E., & Valdes, F. 1995, PASP, 107, 590 35
- Odehahn, S. C., Stockwell, E. B., Pennington, R. L., Humphreys, R. M., & Zumach, W. A. 1992, AJ, 103, 318 39
- Pahre, M. A., Djorgovski, S. G., & de Carvalho, R. R. 1995, ApJ, 453, L17 51
- Papovich, C., Dickinson, M., & Ferguson, H. C. 2001, ApJ, in press 10
- Patton, D. R., Carlberg, R. G., Marzke, R. O., Pritchett, C. J., da Costa, L. N., & Pellegrini, P. S. 2000, ApJ, 536, 153 9
- Patton, D. R., Carlberg, R. G., Marzke, R. O., Pritchett, C. J., da Costa, L. N., & Pellegrini, P. S. 2001, ApJ, in press 9
- Patton, D. R., Pritchett, C. J., Yee, H. K. C., Ellingson, E., & Carlberg, R. G. 1997, ApJ, 475, 29 9
- Pearce, F. R., Jenkins, A., Frenk, C. S., White, S. D. M., Thomas, P. A., Couchman, H. M. P., Peacock, J. A., & Efstathiou, G. 2001, MNRAS, 326, 649 11
- Pettini, M., Kellogg, M., Steidel, C. C., Dickinson, M., Adelberger, K. L., & Giavalisco, M. 1998, ApJ, 508, 539 6
- Pettini, M., Shapley, A. E., Steidel, C. C., Cuby, J., Dickinson, M., Moorwood, A. F. M., Adelberger, K. L., & Giavalisco, M. 2001, ApJ, 554, 981 10
- Phillipps, S., Davies, J. I., & Disney, M. J. 1990, MNRAS, 242, 235 56
- Picard, A. 1991, AJ, 102, 445 71
- Ratcliffe, A., Shanks, T., Parker, Q. A., & Fong, R. 1998, MNRAS, 293, 197 73
- Rieke, G. H., Loken, K., Rieke, M. J., & Tamblyn, P. 1993, ApJ, 412, 99 4

- Rix, H., & Rieke, M. J. 1993, *ApJ*, 418, 123 [vii](#), [16](#), [93](#)
- Roberts, M. S., & Haynes, M. P. 1994, *ARA&A*, 32, 115 [92](#)
- Rowan-Robinson, M., et al. 1997, *MNRAS*, 289, 490 [6](#)
- Saha, P. 1995, *AJ*, 110, 916 [35](#), [45](#)
- Sandage, A., Binggeli, B., & Tammann, G. A. 1985, *AJ*, 90, 1759 [20](#)
- Saracco, P., D'Odorico, S., Moorwood, A., Buzzoni, A., Cuby, J. ., & Lidman, C. 1999, *A&A*, 349, 751 [71](#)
- Saracco, P., Iovino, A., Garilli, B., Maccagni, D., & Chincarini, G. 1997, *AJ*, 114, 887 [17](#)
- Schade, D., et al. 1999, *ApJ*, 525, 31 [3](#), [81](#)
- Schlegel, D. J., Finkbeiner, D. P., & Davis, M. 1998, *ApJ*, 500, 525 [49](#)
- Schmidt, M. 1968, *ApJ*, 151, 393 [83](#)
- Sebok, W. L. 1979, *AJ*, 84, 1526 [38](#)
- Shapley, A. E., Steidel, C. C., Adelberger, K. L., Dickinson, M., Giavalisco, M., & Pettini, M. 2001, *ApJ*, 562, 95 [73](#)
- Simard, L., & Pritchett, C. J. 1998, *ApJ*, 505, 96 [5](#)
- Smail, I., Hogg, D. W., Yan, L., & Cohen, J. G. 1995, *ApJ*, 449, L105 [71](#)
- Smail, I., Ivison, R. J., Kneib, J.-P., Cowie, L. L., Blain, A. W., Barger, A. J., Owen, F. N., & Morrison, G. 1999, *MNRAS*, 308, 1061 [19](#)
- Small, T. A., Ma, C., Sargent, W. L. W., & Hamilton, D. 1999, *ApJ*, 524, 31 [9](#)
- Snigula, J. 2000, Diploma thesis, Ludwig-Maximilians-Universität, München [50](#), [74](#)
- Songaila, A., Cowie, L. L., Hu, E. M., & Gardner, J. P. 1994, *ApJS*, 94, 461 [82](#)
- Stanford, S. A., Eisenhardt, P. R., & Dickinson, M. 1998, *ApJ*, 492, 461 [3](#), [18](#)
- Stanford, S. A., Eisenhardt, P. R. M., & Dickinson, M. 1995, *ApJ*, 450, 512 [18](#)
- Stanford, S. A., Elston, R., Eisenhardt, P. R., Spinrad, H., Stern, D., & Dey, A. 1997, *AJ*, 114, 2232 [3](#), [18](#)
- Steidel, C. C., Giavalisco, M., Pettini, M., Dickinson, M., & Adelberger, K. L. 1996, *ApJ*, 462, L17 [10](#)
- Steidel, C. C., & Hamilton, D. 1992, *AJ*, 104, 941 [10](#)
- Steidel, C. C., & Hamilton, D. 1993, *AJ*, 105, 2017 [10](#), [71](#)

- Steidel, C. C., Pettini, M., & Hamilton, D. 1995, *AJ*, 110, 2519 10
- Stevenson, P. R. F., Shanks, T., & Fong, R. 1986, in *Spectral Evolution of Galaxies*, 439 71
- Strecker, D. W., Erickson, E. F., & Witteborn, F. C. 1979, *ApJS*, 41, 501 23
- Subbarao, M. U., Connolly, A. J., Szalay, A. S., & Koo, D. C. 1996, *AJ*, 112, 929 86
- Sullivan, M., Treyer, M. A., Ellis, R. S., Bridges, T. J., Milliard, B., & Donas, J. . 2000, *MNRAS*, 312, 442 7
- Takeuchi, T. T., Yoshikawa, K., & Ishii, T. T. 2000, *ApJS*, 129, 1 84
- Teplitz, H. I., et al. 2000, *ApJ*, 542, 18 6
- Teplitz, H. I., McLean, I. S., & Malkan, M. A. 1999, *ApJ*, 520, 469 71
- Thomas, D. 2001, Ph.D. thesis, Ludwig-Maximilians-Universität, München 81
- Thompson, D., et al. 1999, *ApJ*, 523, 100 2, 19
- Totani, T., & Yoshii, Y. 1998, *ApJ*, 501, L177 2
- Totani, T., & Yoshii, Y. 2000, *ApJ*, 540, 81 2
- Treu, T., & Stiavelli, M. 1999, *ApJ*, 524, L27 3
- Treu, T., Stiavelli, M., Bertin, G., Casertano, S., & Møller, P. 2001, *MNRAS*, 326, 237 5
- Treyer, M. A., Ellis, R. S., Milliard, B., Donas, J., & Bridges, T. J. 1998, *MNRAS*, 300, 303 7
- Tyson, J. A. 1988, *AJ*, 96, 1 71
- Valdes, F. 1982, *Proceedings of SPIE*, 331, 465 38, 39
- van den Bergh, S., Cohen, J. G., Hogg, D. W., & Blandford, R. 2000, *AJ*, 120, 2190 8
- van Dokkum, P. G., & Franx, M. 1996, *MNRAS*, 281, 985 4
- van Dokkum, P. G., & Franx, M. 2001, *ApJ*, 553, 90 4
- van Dokkum, P. G., Franx, M., Kelson, D. D., & Illingworth, G. D. 1998, *ApJ*, 504, L17 4
- van Dokkum, P. G., Stanford, S. A., Holden, B. P., Eisenhardt, P. R., Dickinson, M., & Elston, R. 2001, *ApJ*, 552, L101 3
- Veron-Cetty, M.-P., & Veron, P. 1996, "A Catalogue of quasars and active nuclei" (ESO Scientific Report, Garching: European Southern Observatory (ESO), 7th ed.) 21, 27

- Vogt, N. P., Forbes, D. A., Phillips, A. C., Gronwall, C., Faber, S. M., Illingworth, G. D., & Koo, D. C. 1996, *ApJ*, 465, L15 5
- Vogt, N. P., et al. 1997, *ApJ*, 479, L121 5
- Wainscoat, R. J., & Cowie, L. L. 1992, *AJ*, 103, 332 25
- Williams, R. E., et al. 2000, *AJ*, 120, 2735 1, 15
- Williams, R. E., et al. 1996, *AJ*, 112, 1335 1, 15, 17, 71
- Worthey, G. 1994, *ApJS*, 95, 107 94
- Yan, L., McCarthy, P. J., Weymann, R. J., Malkan, M. A., Teplitz, H. I., Storrie-Lombardi, L. J., Smith, M., & Dressler, A. 2000, *AJ*, 120, 575 2
- Yee, H. K. C. 1991, *PASP*, 103, 396 33, 35
- Yee, H. K. C., & Ellingson, E. 1995, *ApJ*, 445, 37 9
- Yee, H. K. C., Ellingson, E., & Carlberg, R. G. 1996, *ApJS*, 102, 269 2
- Yee, H. K. C., & Green, R. F. 1987, *ApJ*, 319, 28 71
- Yoshii, Y. 1993, *ApJ*, 403, 552 50
- Zepf, S. E., & Koo, D. C. 1989, *ApJ*, 337, 34 9
- Ziegler, B. L., & Bender, R. 1997, *MNRAS*, 291, 527 4
- Ziegler, B. L., Saglia, R. P., Bender, R., Belloni, P., Greggio, L., & Seitz, S. 1999, *A&A*, 346, 13 4

Appendix A

Photometric calibration using the stellar sequence

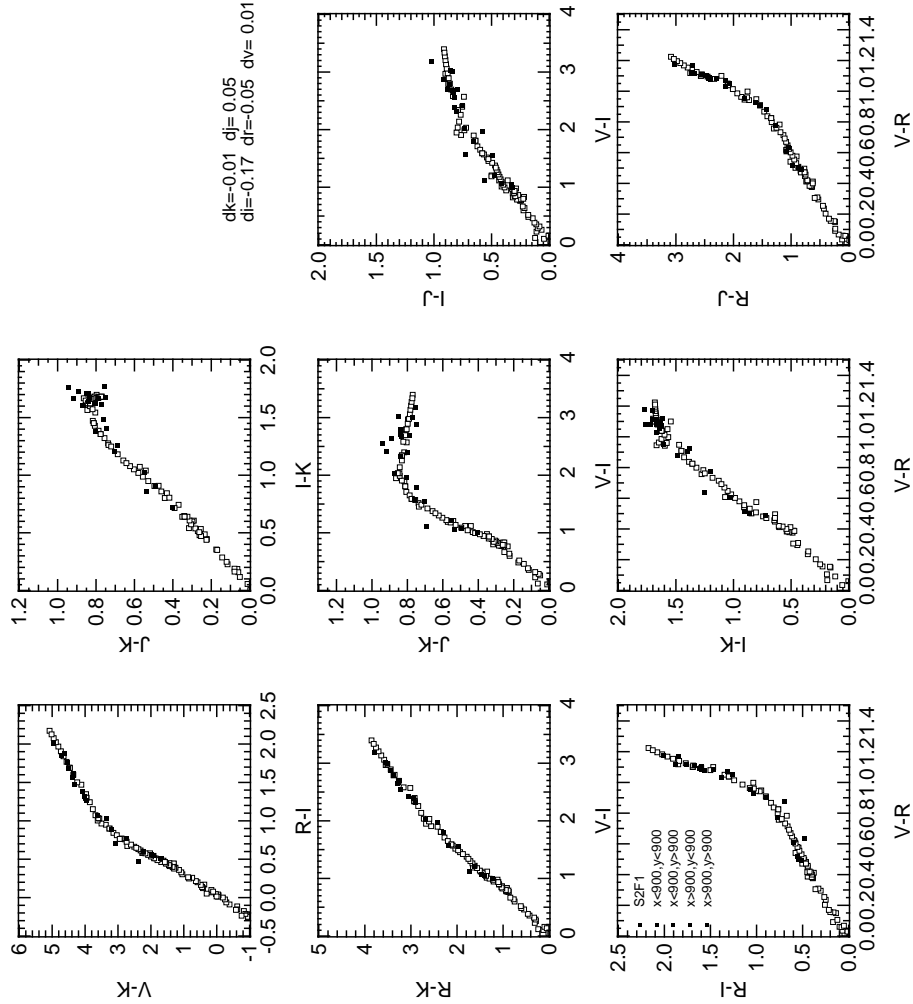


Figure A.1: Photometric calibration using artificial stellar photometry in S2F1. The K -band magnitude is calibrated on 2MASS, all other colors are calibrated to fit the artificial stellar photometry (BPGS-Library) using the offsets given in the plot. See Sect. 2.2.4

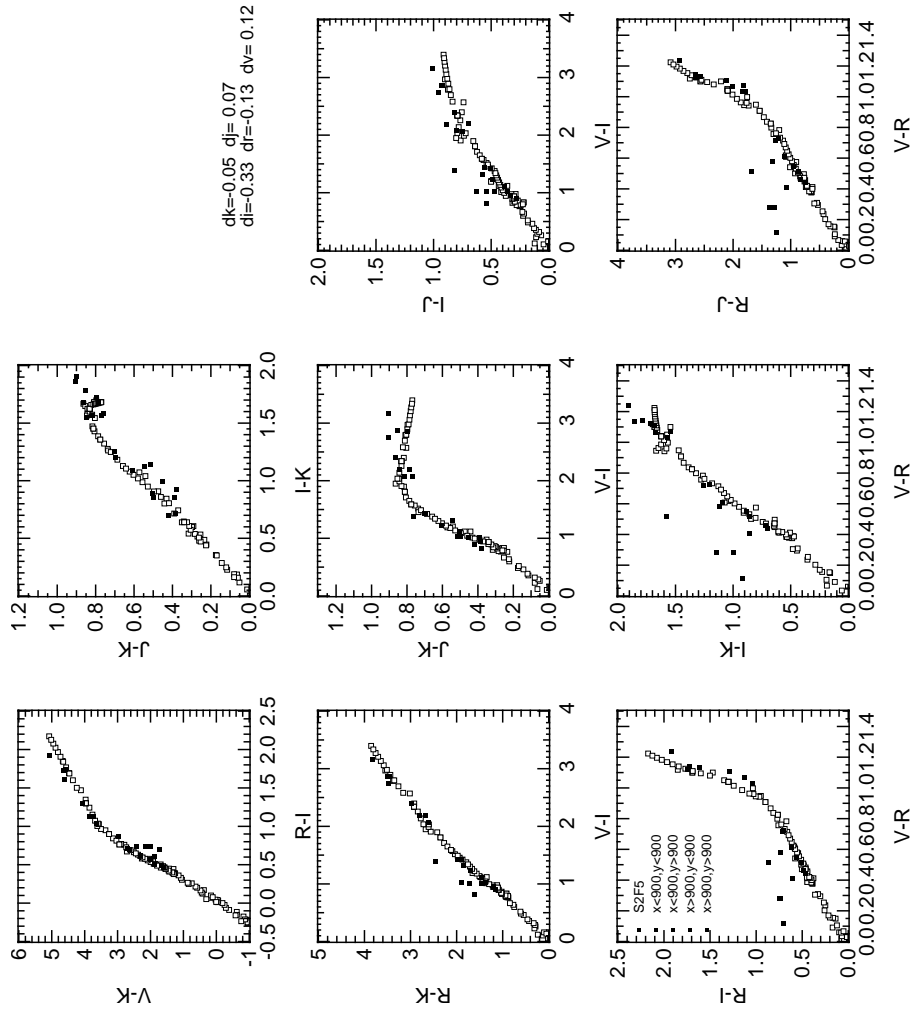


Figure A.2: Photometric calibration using artificial stellar photometry in S2F5. The K -band magnitude is calibrated on 2MASS, all other colors are calibrated to fit the artificial stellar photometry (BPGS-Library) using the offsets given in the plot. See Sect. 2.2.4

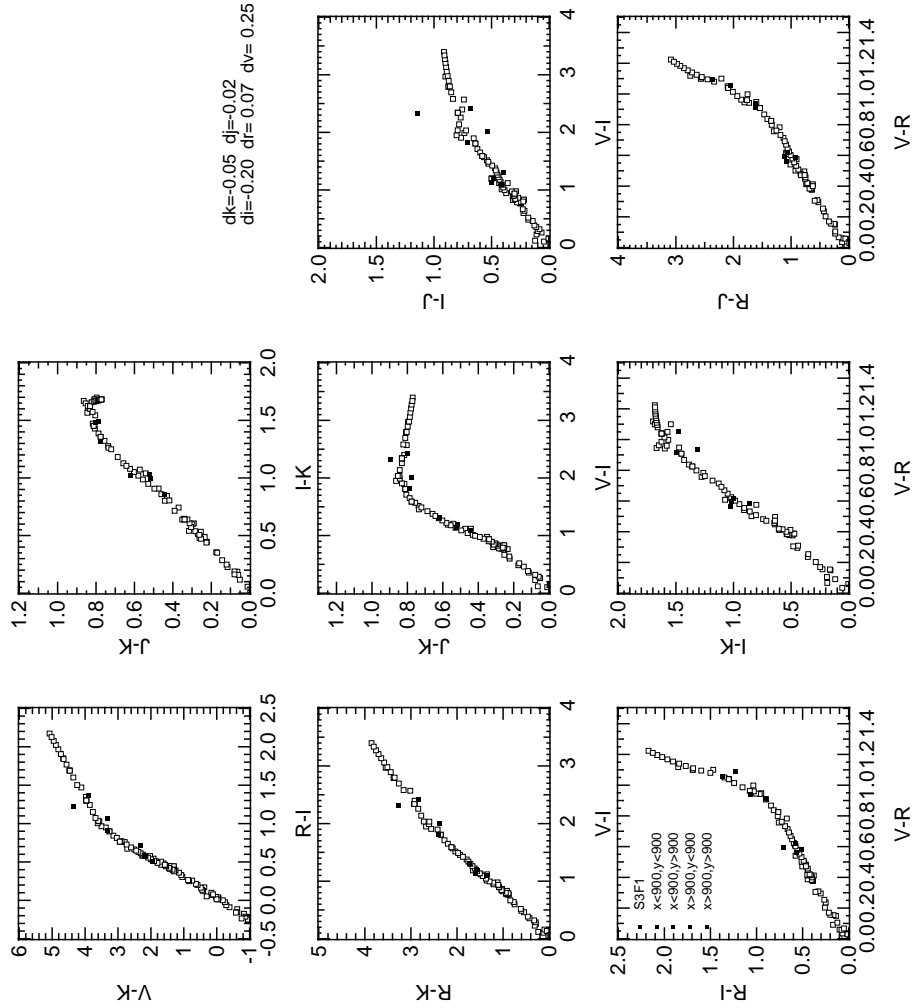


Figure A.3: Photometric calibration using artificial stellar photometry in S3F1. The K -band magnitude is calibrated on 2MASS, all other colors are calibrated to fit the artificial stellar photometry (BPGS-Library) using the offsets given in the plot. See Sect. 2.2.4

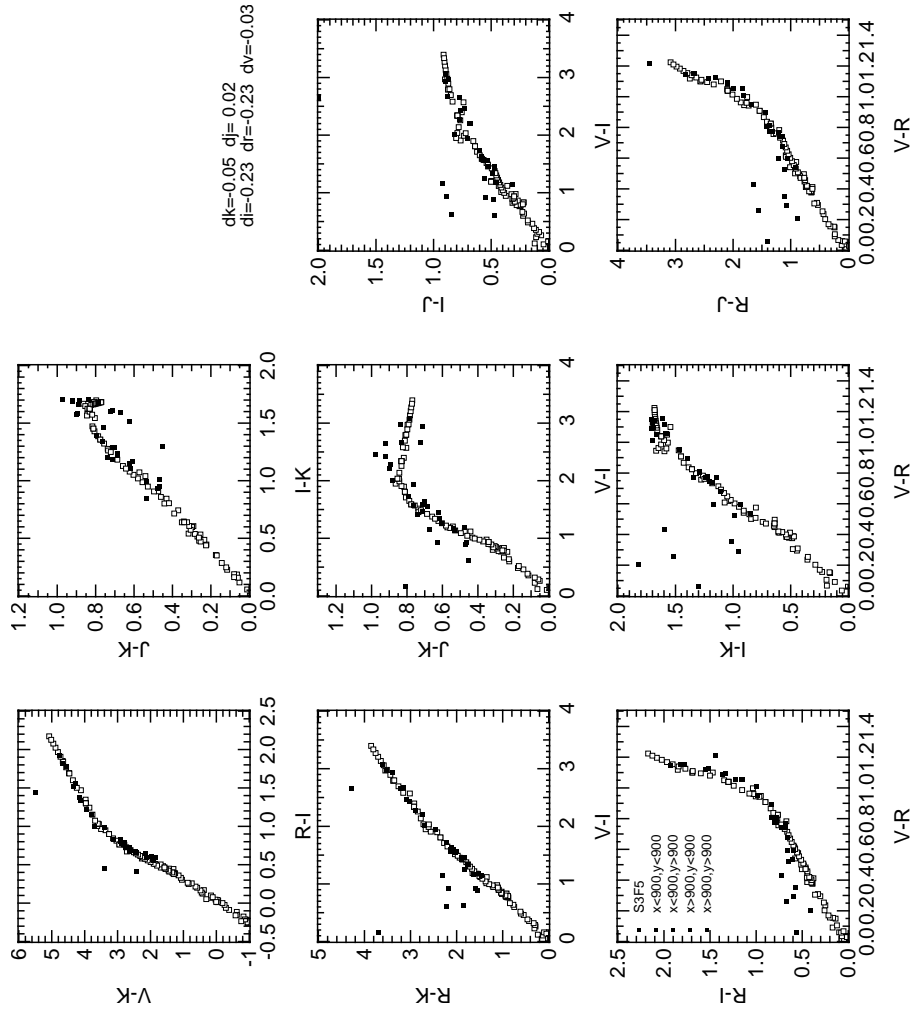


Figure A.4: Photometric calibration using artificial stellar photometry in S3F5. The K -band magnitude is calibrated on 2MASS, all other colors are calibrated to fit the artificial stellar photometry (BPGS-Library) using the offsets given in the plot. See Sect. 2.2.4

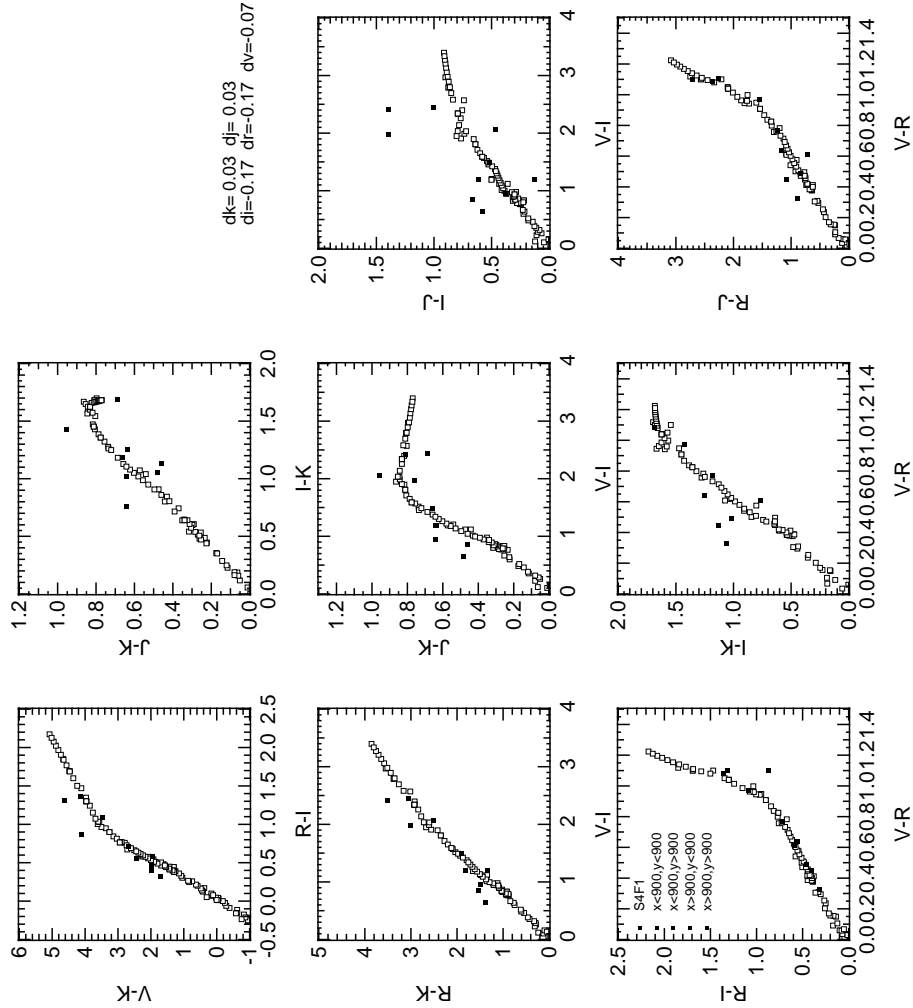


Figure A.5: Photometric calibration using artificial stellar photometry in S4F1. The K -band magnitude is calibrated on 2MASS, all other colors are calibrated to fit the artificial stellar photometry (BPGS-Library) using the offsets given in the plot. See Sect. 2.2.4

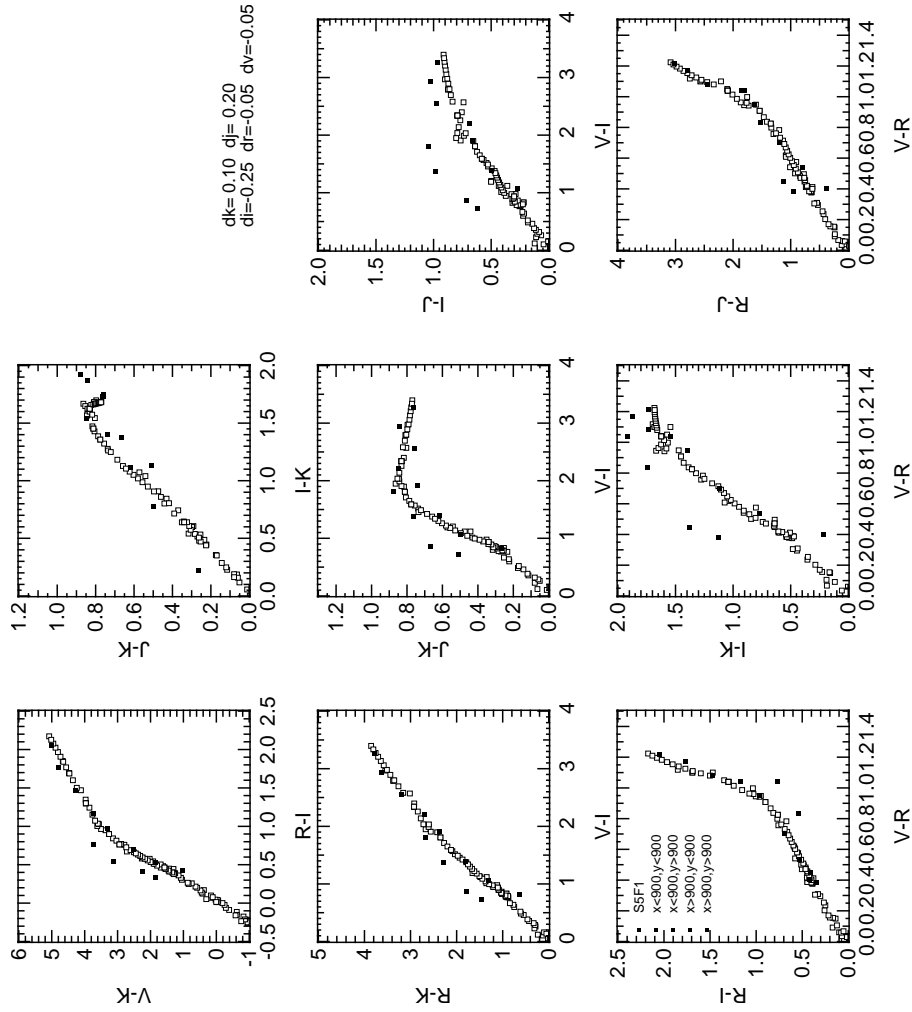


Figure A.6: Photometric calibration using artificial stellar photometry in S5F1. The K -band magnitude is calibrated on 2MASS, all other colors are calibrated to fit the artificial stellar photometry (BPGS-Library) using the offsets given in the plot. See Sect. 2.2.4

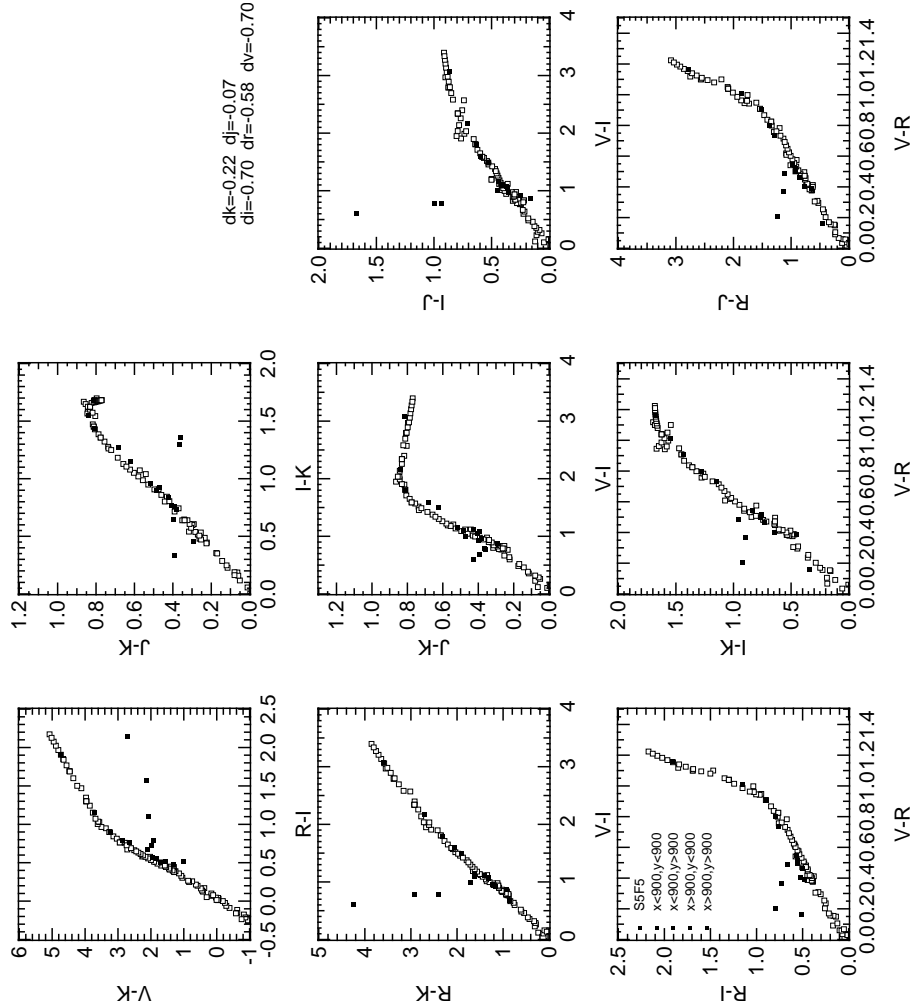


Figure A.7: Photometric calibration using artificial stellar photometry in S5F5. The K -band magnitude is calibrated on 2MASS, all other colors are calibrated to fit the artificial stellar photometry (BPGS-Library) using the offsets given in the plot. See Sect. 2.2.4

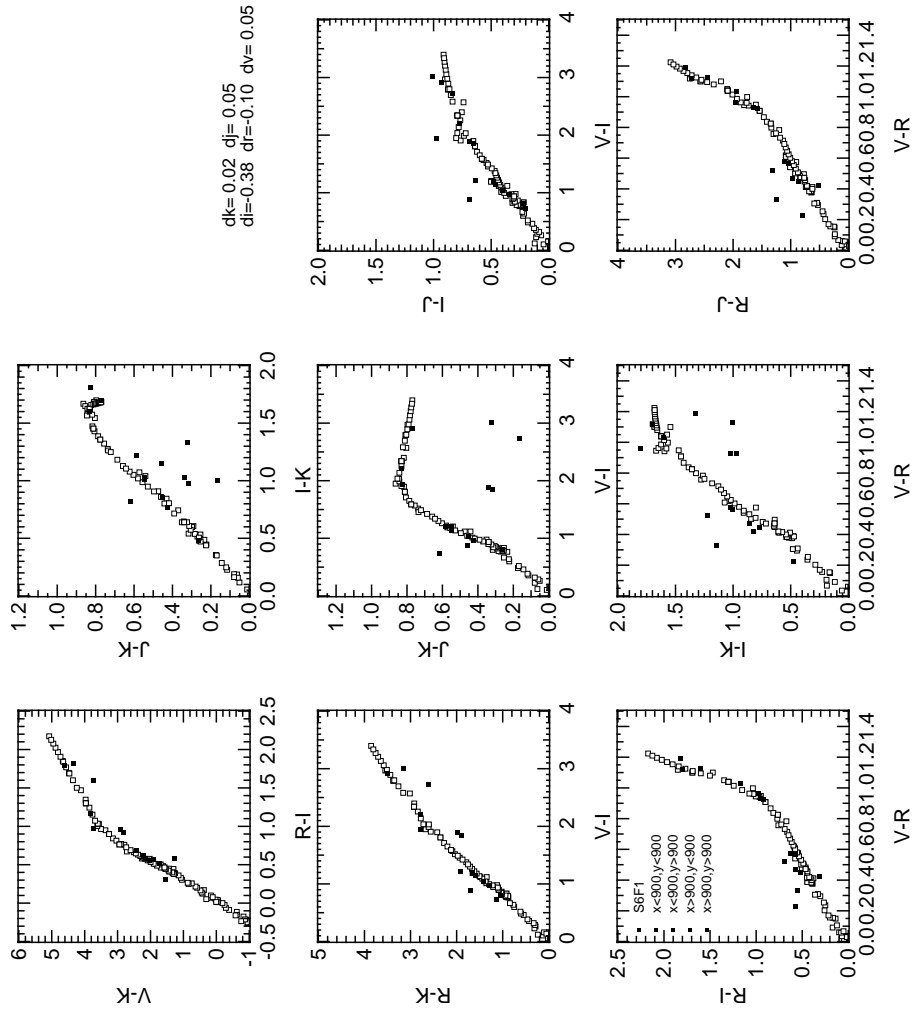


Figure A.8: Photometric calibration using artificial stellar photometry in S6F1. The K -band magnitude is calibrated on 2MASS, all other colors are calibrated to fit the artificial stellar photometry (BPGS-Library) using the offsets given in the plot. See Sect. 2.2.4

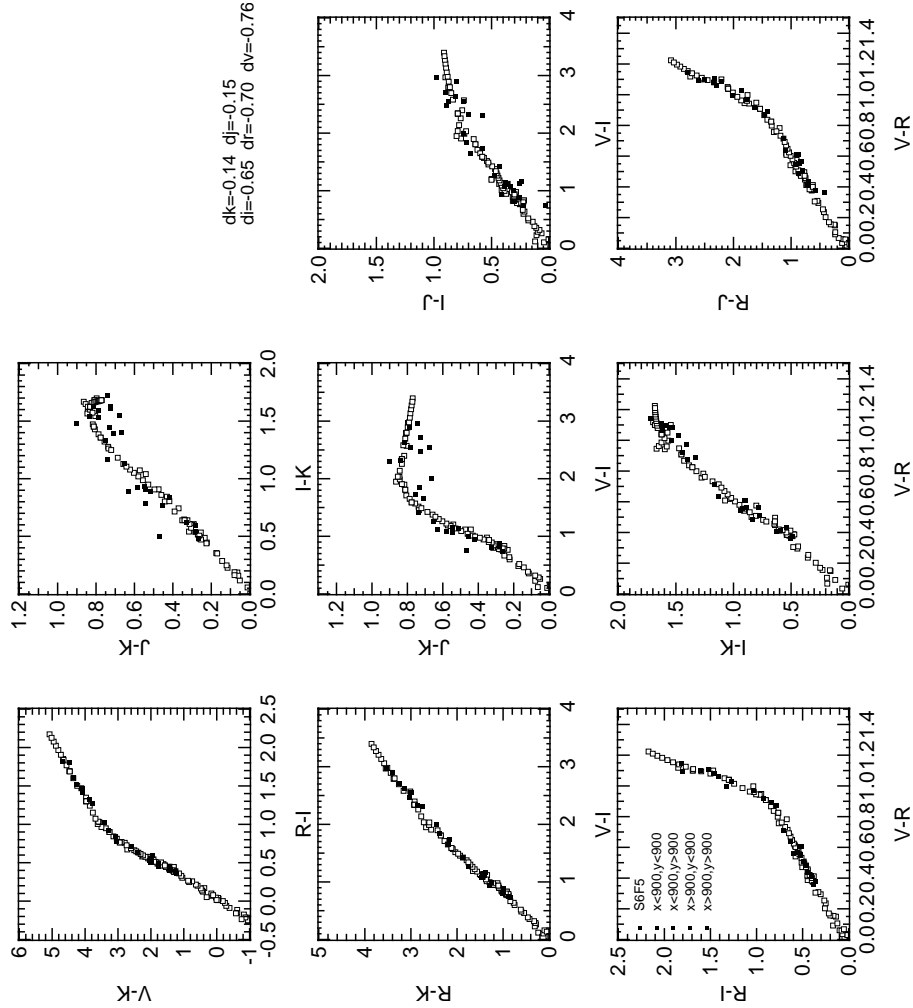


Figure A.9: Photometric calibration using artificial stellar photometry in S6F5. The K -band magnitude is calibrated on 2MASS, all other colors are calibrated to fit the artificial stellar photometry (BPGS-Library) using the offsets given in the plot. See Sect. 2.2.4

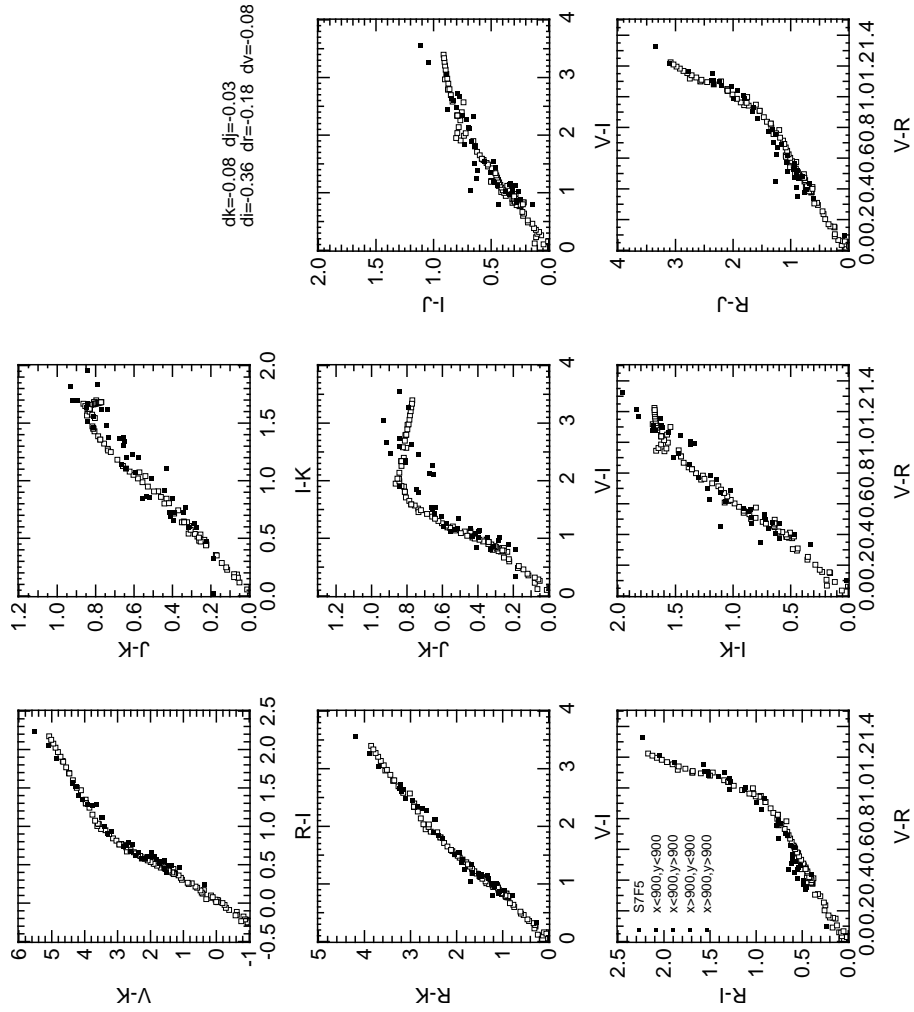


Figure A.10: Photometric calibration using artificial stellar photometry in S7F5. The K -band magnitude is calibrated on 2MASS, all other colors are calibrated to fit the artificial stellar photometry (BPGS-Library) using the offsets given in the plot. See Sect. 2.2.4

Appendix B

Detection probabilities for pointlike and extended sources

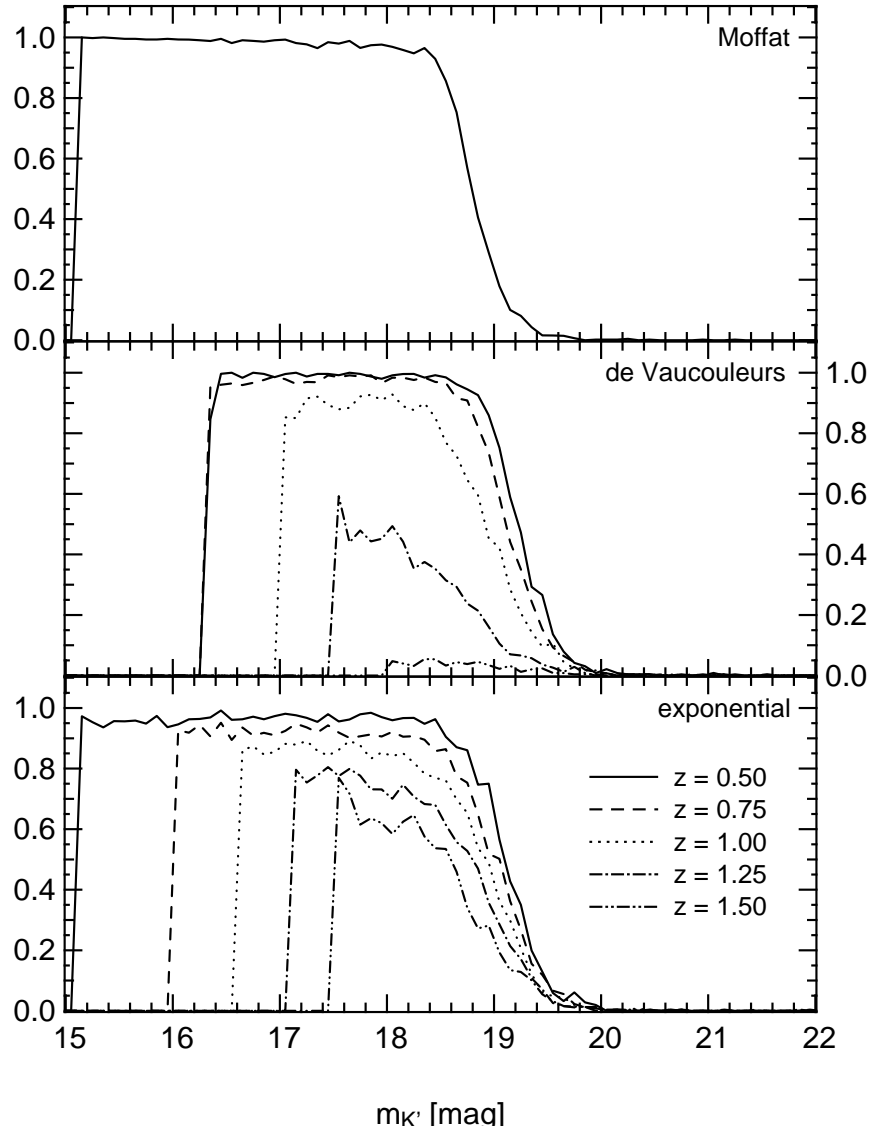


Figure B.1: Detection probabilities for point-like sources, de Vaucouleurs profiles, and exponential profiles as a function of magnitude in S2F1. See Sect. 4.5

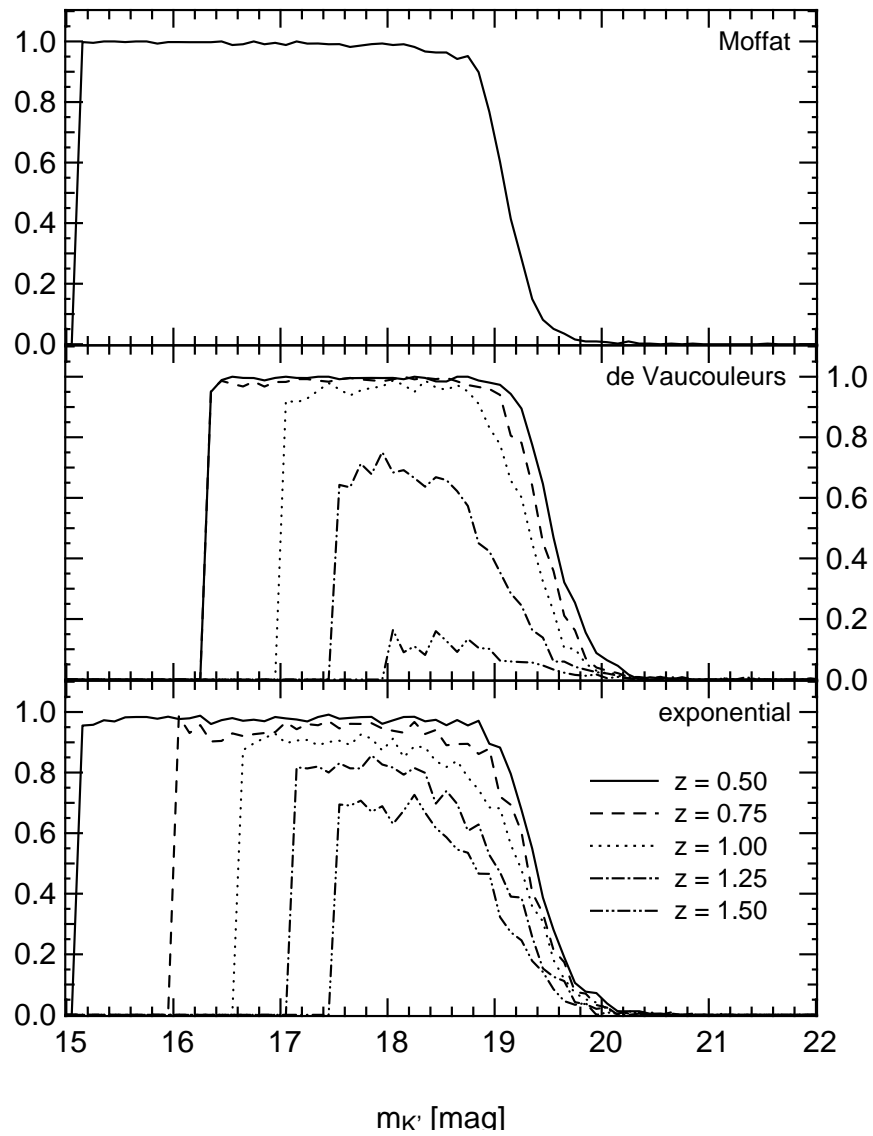


Figure B.2: Detection probabilities for point-like sources, de Vaucouleurs profiles, and exponential profiles as a function of magnitude in S2F5. See Sect. 4.5

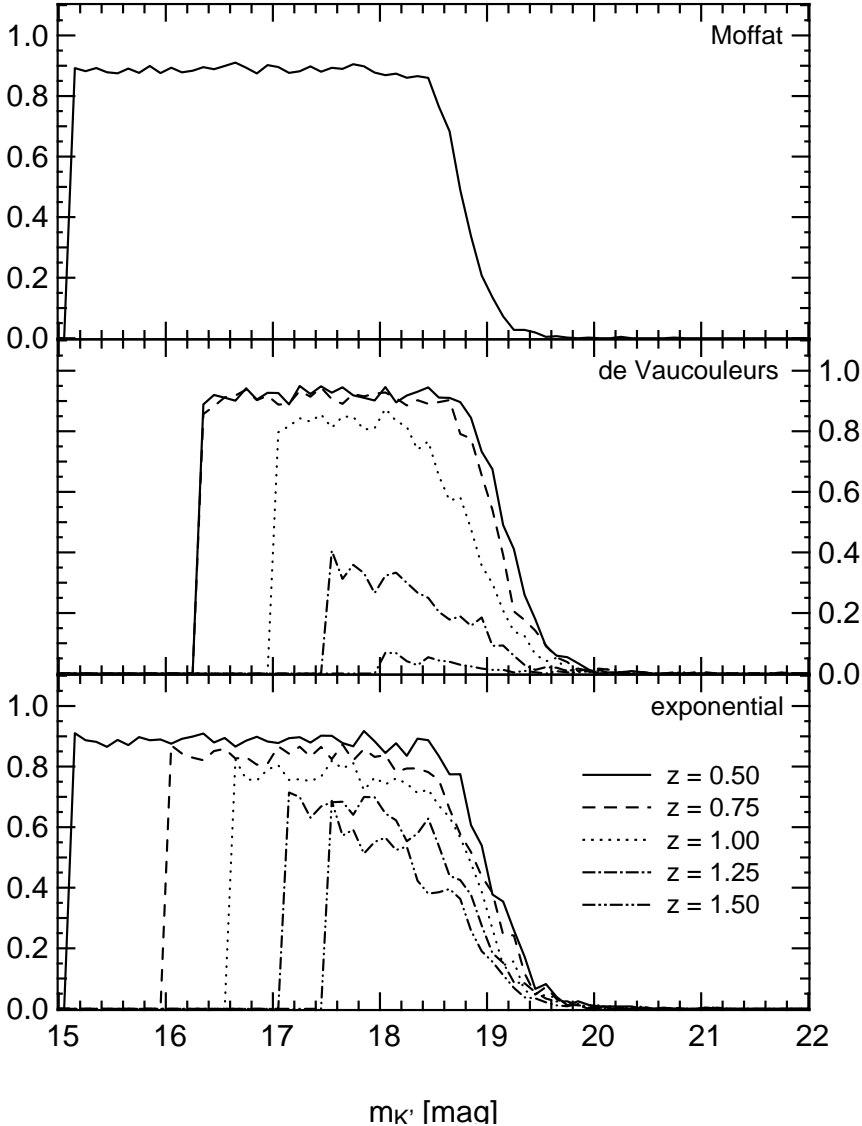


Figure B.3: Detection probabilities for point-like sources, de Vaucouleurs profiles, and exponential profiles as a function of magnitude in S3F1. See Sect. 4.5

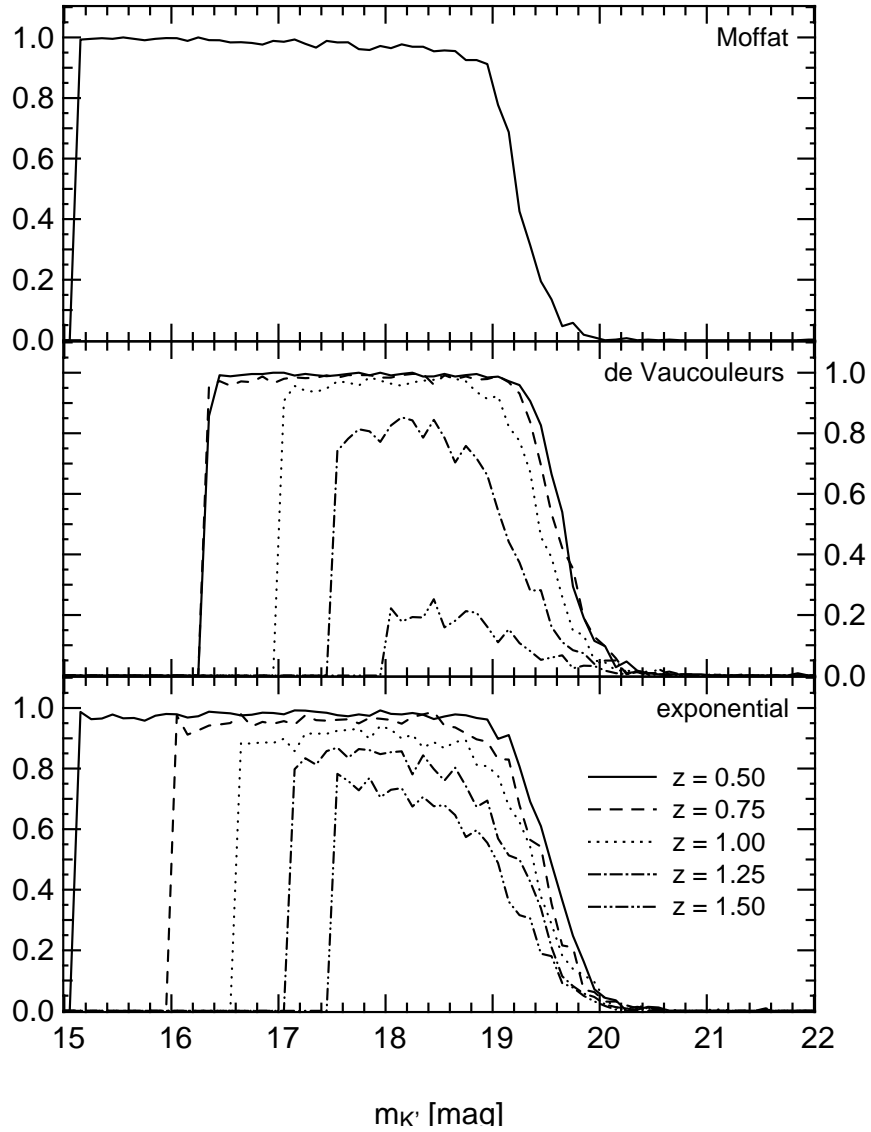


Figure B.4: Detection probabilities for point-like sources, de Vaucouleurs profiles, and exponential profiles as a function of magnitude in S3F5. See Sect. 4.5

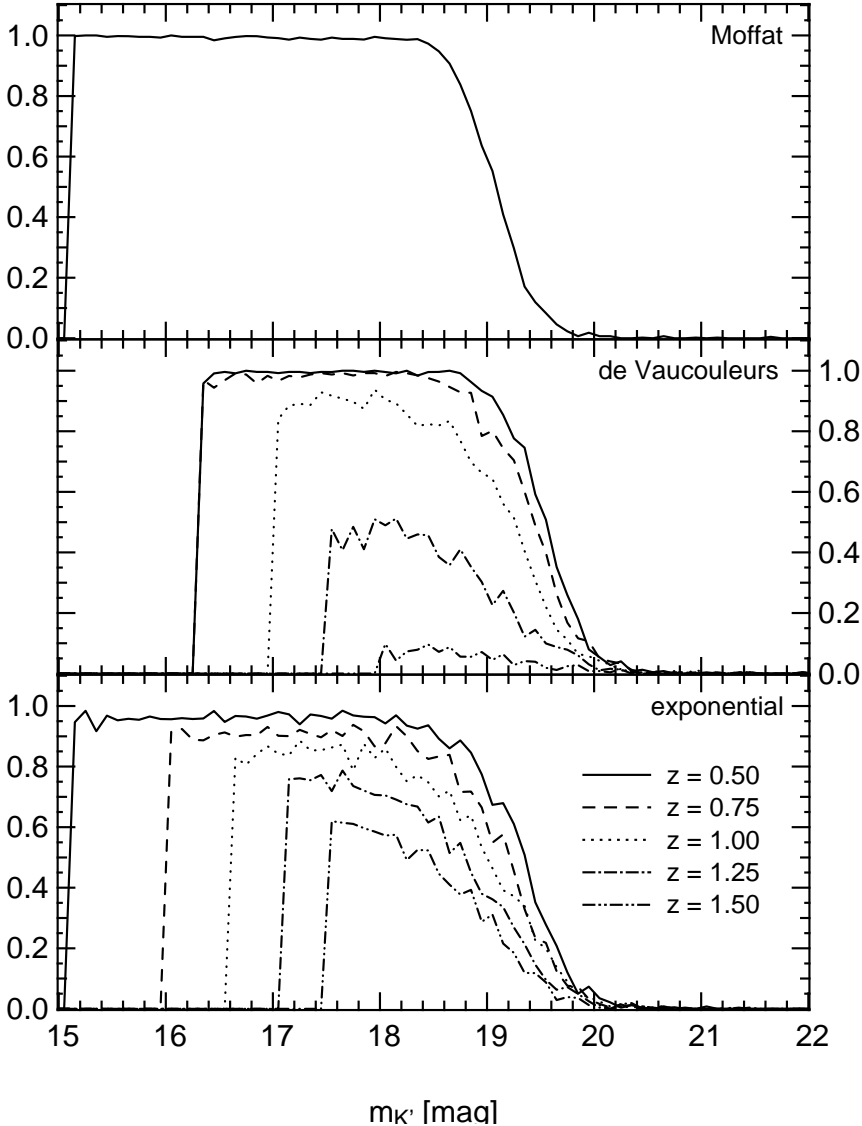


Figure B.5: Detection probabilities for point-like sources, de Vaucouleurs profiles, and exponential profiles as a function of magnitude in S4F1. See Sect. 4.5

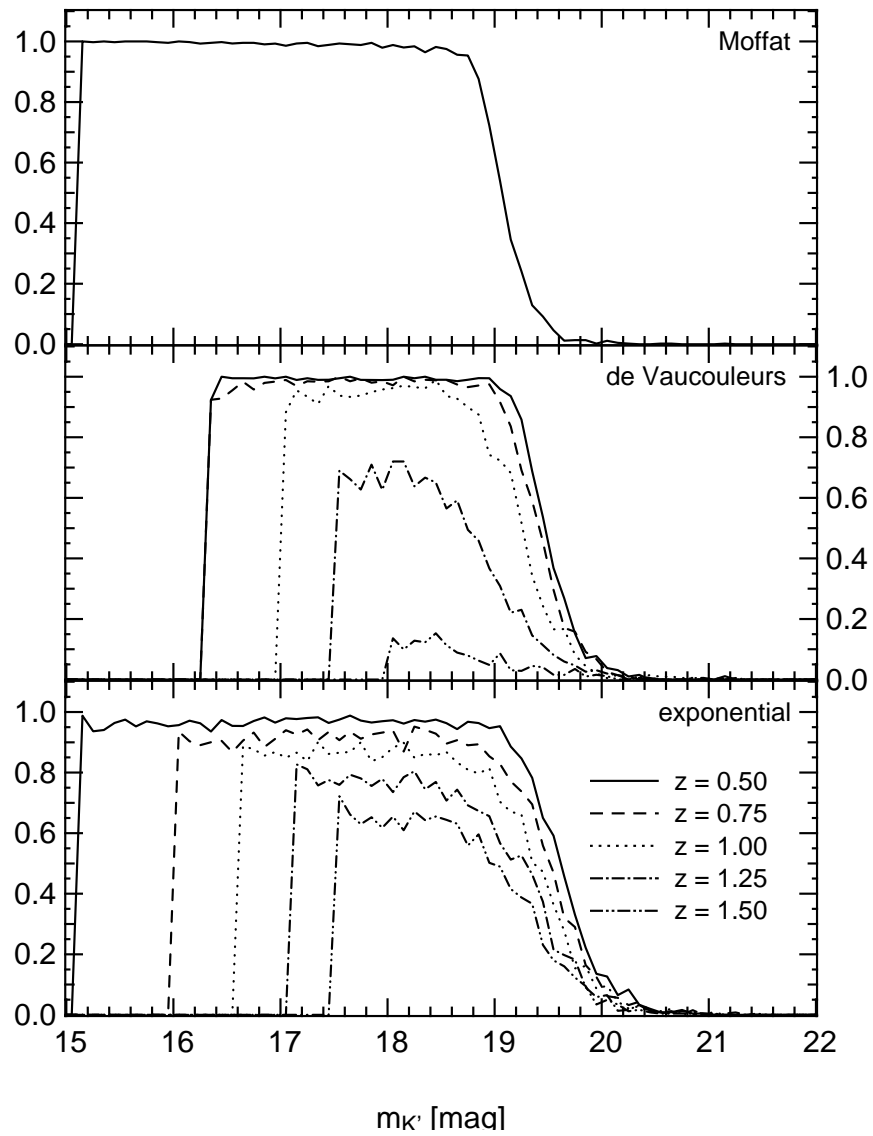


Figure B.6: Detection probabilities for point-like sources, de Vaucouleurs profiles, and exponential profiles as a function of magnitude in S5F1. See Sect. 4.5

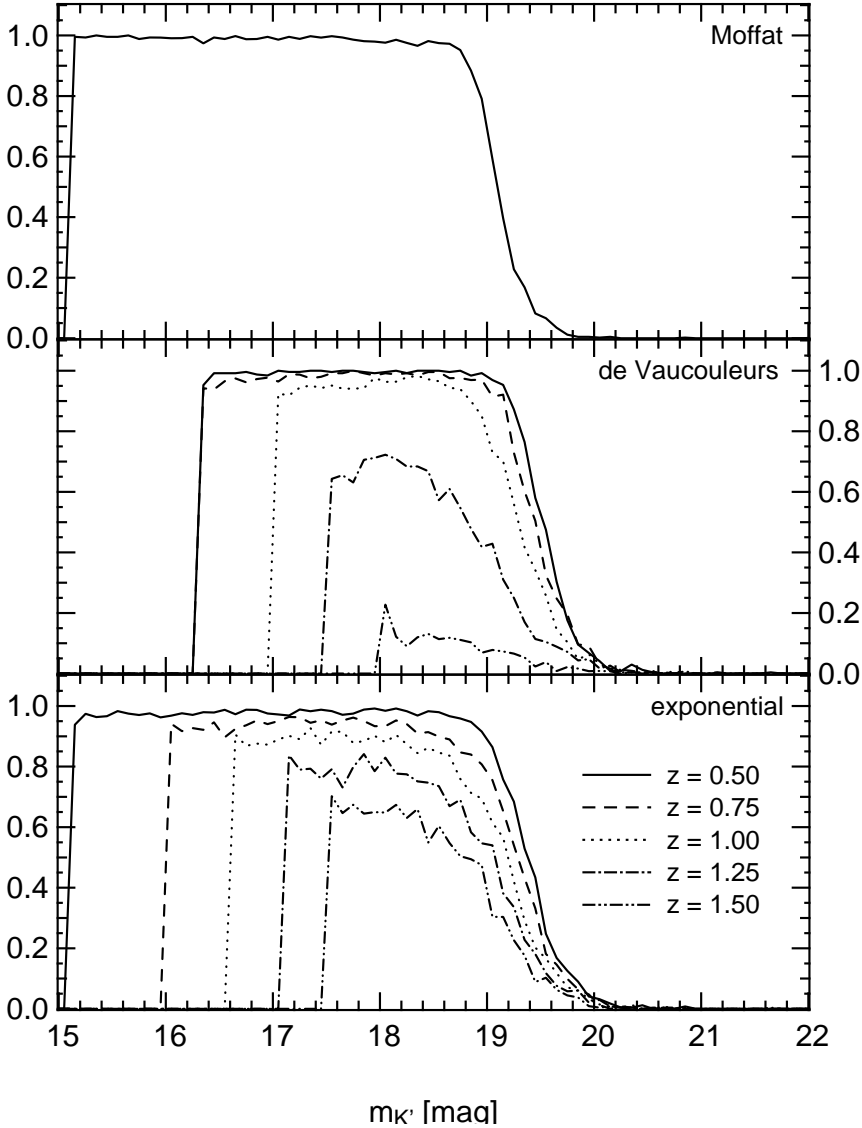


Figure B.7: Detection probabilities for point-like sources, de Vaucouleurs profiles, and exponential profiles as a function of magnitude in S5F5. See Sect. 4.5

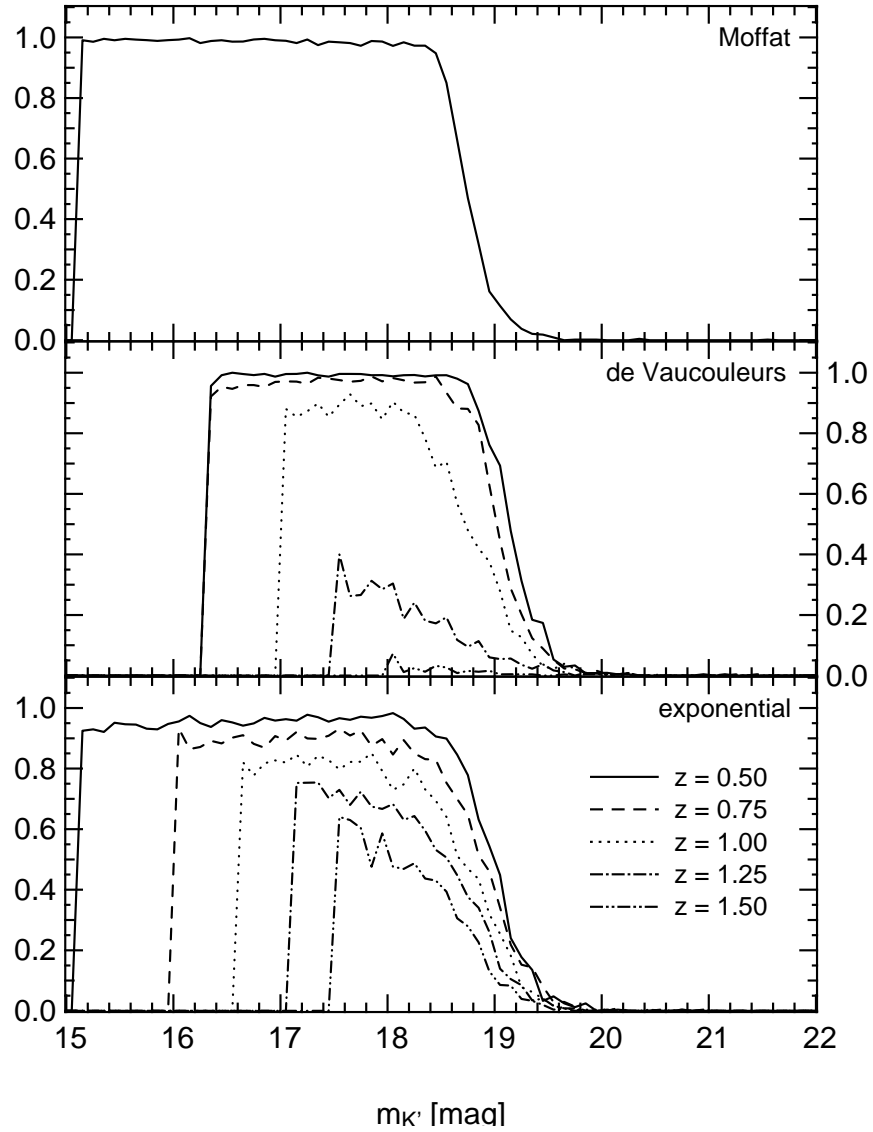


Figure B.8: Detection probabilities for point-like sources, de Vaucouleurs profiles, and exponential profiles as a function of magnitude in S6F1. See Sect. 4.5

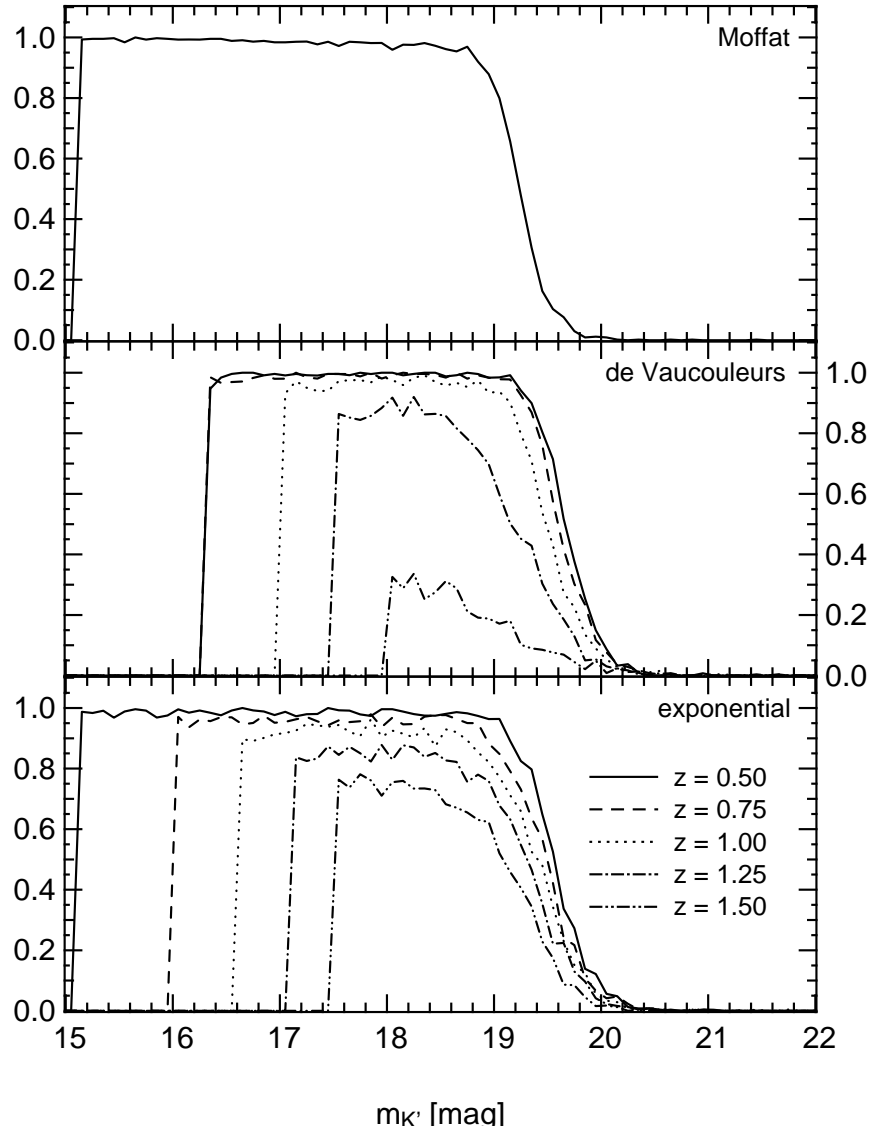


Figure B.9: Detection probabilities for point-like sources, de Vaucouleurs profiles, and exponential profiles as a function of magnitude in S6F5. See Sect. 4.5

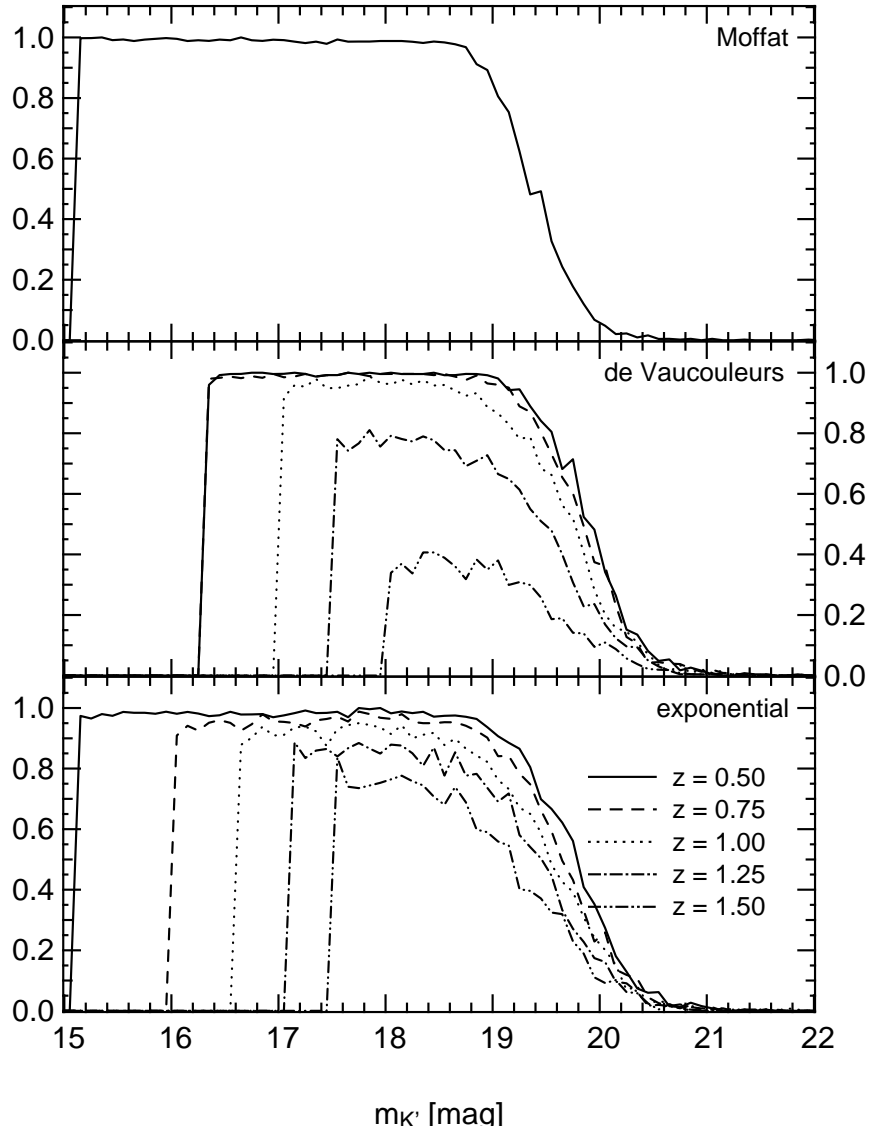


Figure B.10: Detection probabilities for point-like sources, de Vaucouleurs profiles, and exponential profiles as a function of magnitude in S7F5. See Sect. 4.5

Acknowledgments

Ralf Bender, my thesis advisor, deserves my deeply felt gratitude for his never-ending patience, his support, and for his confidence in me, for giving me the freedom to find my way. His office door is always open, and never has he rejected me, never discouraged me to ask a question, never stopped me articulating a concern or express an idea, no matter how busy he was. Who does not wish such a teacher.

I owe no less gratitude to Ulrich Hopp, my co-advisor, for his endless endurance, for his efforts in supporting me and the MUNICS project, for being there whenever I needed assistance, for his honesty, and for always asking the right questions.

The “other” members of the MUNICS team and Ph.D.-student-colleagues Chris Botzler, Georg Feulner, and Jan Snigula deserve my honestly felt gratitude and appreciation. Their work within our project has been most valuable. Working together has been a pleasure. I couldn’t have done without them.

This is also true for Claudia Mendes de Oliveira, who got me started working on MUNICS, taught me infrared data reduction and has spent so many hours encouraging me to keep going during her much anticipated visits to Munich later on.

Our other remote project member, Gary J. Hill, who brought me to McDonald Observatory and helped me get started there and has since then contributed to the project also deserves my gratitude.

I am grateful to my roommates Daniel Thomas and Claudia Maraston for many inspiring discussions, for their lively criticism, and for many lovely evenings we spent together at various occasions. Oh, and for the Italian I’ve learnt during the last four years.

The members of the extragalactic group here at the Sternwarte, Roberto Saglia, Laura Greggio, Stella Seitz, Mark Neeser, and Don Hamilton have taught me a lot. Their friendliness and their patience, but also their criticism, their skepticism, and all the obnoxious questions asked during many seminars have made work at the institute both fruitful and a pleasure.

I owe thanks to Michael Mathias, Dörte Mehlert, Jan Beuing, and Bodo Ziegler, with whom I had the pleasure to share the office, too, in the course of my thesis.

I am grateful to Claus Gössl and Arno Riffeser for many hours of discussing, cod-

ing, testing, and debugging we've spent together. Exchanging ideas on data reduction and on YODA with them was a pleasure. And thanks for getting and installing the coffee machine.

I am grateful to the rest of the extragalactic gang, my dear student colleagues Jürgen Fliri, Armin Gabasch, Thomas Puzia, and Jens Thomas for many discussions, ideas, lunch breaks, coffee breaks, and for the excellent atmosphere here at the institute.

I would like to explicitly thank the staff at Calar Alto Observatory for their long-standing support during the last five years, both for supporting us during many observing runs and for carrying out observations in service mode.

Last but not least, my friends and family. Without their love, support, and encouragement, this work would not have been possible.

Lebenslauf

Persönliche Daten

Name:	Niv Oliver Michael Tomer Drory
Geburtsdatum:	10. Januar 1972
Geburtsort:	Haifa, Israel

Ausbildung:

1978–1984	Besuch der 1. bis 6. Klasse der Reali-Grundschule in Haifa, Israel.
1984–1991	Besuch der 7. bis 13. Klasse des Luitpold-Gymnasiums, München
1991	Abitur
1991–1997	Studium der Physik an der Ludwig-Maximilians-Universität, München
1996–1997	Diplomarbeit an der Universitätssternwarte, München
1997	Diplom in Physik
1998–2002	Dissertation an der Universitäts-Sternwarte München